ENHANCEMENT, QUANTITATIVE UNDERSTANDING, AND TUNING OF SPIN DIFFUSION LENGTH IN COPPER

by

Xingyu Shen

A dissertation submitted to the Faculty of the University of Delaware in partial fulfillment of the requirements for the degree of Doctor of Philosophy in Physics

Winter 2024

ENHANCEMENT, QUANTITATIVE UNDERSTANDING, AND TUNING OF SPIN DIFFUSION LENGTH IN COPPER

by

Xingyu Shen

Approved: ____
Edmund R. Nowak, Ph.D.
Chair of the Department of Physics and Astronomy

Approved: ____
Debra Hess Norris
Dean of the College of Arts and Sciences

Approved: ____
Louis F. Rossi, Ph.D.
Vice Provost for Graduate and Professional Education and
Dean of the Graduate College

I certify that I have read this dissertation and that in my opinion it meets the academic and professional standard required by the University as a dissertation for the degree of Doctor of Philosophy.

Signed: ______________________________

Yi Ji, Ph.D.
Professor in charge of dissertation

I certify that I have read this dissertation and that in my opinion it meets the academic and professional standard required by the University as a dissertation for the degree of Doctor of Philosophy.

Signed: ______________________________

Jamie Holder, Ph.D.
Member of dissertation committee

I certify that I have read this dissertation and that in my opinion it meets the academic and professional standard required by the University as a dissertation for the degree of Doctor of Philosophy.

Signed: ______________________________

Benjamin Jungfleisch, Ph.D.
Member of dissertation committee

I certify that I have read this dissertation and that in my opinion it meets the academic and professional standard required by the University as a dissertation for the degree of Doctor of Philosophy.

Signed: ______________________________

Anderson Janotti, Ph.D.
Member of dissertation committee

ACKNOWLEDGMENTS

Scientific explorations, like numerous other pursuits, involve inherent unpredictability and hence risks. Additionally, physics is known for its difficulty and solitude, compounded by the pressure that physicists face from various directions. I express my deepest gratitude to my advisor, Dr. Yi Ji, for never putting pressure on me and for fostering an environment of open-mindedness and freedom throughout this journey. This allowed me the autonomy to work at my own pace and explore individual ideas. Additionally, I appreciate his extensive knowledge in the field of spin transport, but with a down-to-earth attitude.

I extend appreciation to my committee members: Dr. Jamie Holder, Dr. Benjamin Jungfleisch, and Dr. Anderson Janotti. A special acknowledgment goes to Dr. Holder for his meticulous review and detailed suggestions on this thesis.

My gratitude extends to our collaborator, Dr. Yizheng Wu, from Fudan University.

I express thanks to the UNDF staff—Dr. Iulian Codreanu, Dr. Kevin Lister, Paul Horng, and Scott McCracken—without whose support this thesis would have been impossible. Special thanks to Kevin for his guidance on the fundamentals of lithography and wafer handling.

Additionally, I would like to thank my fellow lab mates, including Dr. Yunjiao Cai, Dr. Chuan Qin, Dr. Fatih Kandaz, Dr. Hang Chen, and Dr. Yang Wang, for their invaluable research and psychological support. Special thanks to Yunjiao for serving as a role model.

I extend my thanks to the staff and faculty members in the Department of Physics and Astronomy for their kind assistance. A special note of appreciation goes to our lab manager, Dr. John Shaw, for his relaxed demeanor and for being understanding, flexible, and supportive in my role as a teaching assistant. I also extend thanks to Dr. Edmund Nowak for his generosity in granting us access to his wire bonder.

Last but not least, I convey my deepest thanks to my parents, Jing Kang and Yanlai Shen, for their unconditional love.

TABLE OF CONTENTS

LIST OF TABLES

LIST OF FIGURES

ABSTRACT

Spintronics exploits electron's intrinsic spin degree of freedom along with its fundamental charge for information processing and data storage. Spin current, the flow of electronic spin angular momentum, is integral to the functionalities of spintronics and has been a central subject of fundamental research. When a spin current is injected into a material, it decays exponentially over distance, a phenomenon known as the spin relaxation with the characteristic decay length being the spin diffusion length λ. Therefore, to maintain a robust spin current in spintronic circuity, a long spin diffusion length is highly desirable.

In mesoscopic metallic channels made of Cu, Al, and Ag, λ has been shown to be substantial but is in general limited to 1 μm even at low temperatures. The direction toward further enhancement of λ is unclear. In addition, detailed quantitative understanding of the spin relaxation processes in these metals remains challenging, because phonons, impurities, surfaces, spin-orbital effects, grain boundaries, and Kondo effects all contribute to the spin relaxation and are non-trivial to separate. Furthermore, the electrical tunability of spin relaxation provides an intriguing avenue for achieving electrically tunable spin currents but has remained largely unexplored to date. In this dissertation, progress toward resolving these issues will be presented via three related studies that utilize nonlocal spin valve (NLSV) structures with mesoscopic spin transport channels made of Cu.

In the first study, enhanced spin diffusion lengths up to 5 μm have been demonstrated in mesoscopic Cu channels at low temperatures. With a modest increase

of the cross-sectional area of the Cu channels to 0.5 × 0.5 μm^2, the low temperature electrical conductivity values of channels are dramatically enhanced. Based on 14 structures fabricated in a single batch, we found an average spin diffusion length of λ_{Cu} = 3.2 ± 0.7 μm and an average spin relaxation time of τ_s = 120 ± 50 ps at 30 K. Substantial variations are observed among devices, and the spin diffusion length correlates well with the resistivity. The most conductive Cu channel in the batch yields λ_{Cu} = 5.3 ± 0.8 μm and τ_s = 250 ± 80 ps. These superior values exceed expectations for metals and can be attributed to reduced spin relaxation from grain boundaries and surfaces.

In the second study, we have quantitatively established the relation between the Kondo spin relaxation rate ${\tau_{sK}}^{-1}$ and the Kondo momentum relaxation rate ${\tau_{eK}}^{-1}$ by using Cu channels that contain dilute Fe impurities. A linear relation between ${\tau_{sK}}^{-1}$ and ${\tau_{eK}}^{-1}$ is established under varying temperatures for any given device. Among 20 devices, however, ${\tau_{sK}}^{-1}$ remains nearly constant despite variation of ${\tau_{eK}}^{-1}$ by a factor of 10. This surprising relation can be understood by considering spin relaxation through overlapping Kondo screening clouds and supports the physical existence of the elusive Kondo clouds.

In the third study, we demonstrate the electrical tunability of λ_{cu} by using the ionic gating technique via a Li^+ containing solid polymer electrolyte. At 5 K, λ_{cu} is tuned reversibly between 670 nm and 410 nm and the Cu resistivity ρ_{cu} is tuned by 9% in relatively thin Cu channel with 65 nm thickness. The strength of the Kondo effect due to the Fe impurities is tuned by one order of magnitude. At room temperature, λ_{cu} is tuned between 380 nm and 300 nm and ρ_{cu} is tuned by 7%. A gradual amplification of the tuning ranges by repeated gate cycling is observed and clearly suggests an electrochemical origin. We hypothesize that reversible diffusion of Li along the Cu grain boundaries leads to the tuning effects. Tunable spin relaxation in simple metals enriches functionalities in metal-based spintronics.

Chapter 1

INTRODUCTION

Spintronics emerges as an alternative technology to the traditional charge-based electronics by utilizing electron's spin degree of freedom for novel applications such as logic-in-memory computing [1], spin based current modulator [2], quantum information processing [3], and non-volatile memory [4]. Compared with electronics, spintronic devices have potential advantages including lower power consumption, higher integration density, nonvolatility, and faster processing speed [5].

One of the core topics of spintronics is the spin injection from ferromagnetic (FM) metals into nonmagnetic (NM) materials, which was first demonstrated by Johnson and Silsbee using a FM/NM/FM geometry later known as the nonlocal/lateral spin valve (NLSV), as illustrated in Figure 1.1 [6]. In ferromagnets such as Fe, Co, and Ni, the spin up and spin down sub-bands have different conductivities, therefore the electric current in these materials is spin polarized. When such a current is sent from a FM stripe (spin injector) into a NM channel, a splitting of the Fermi level between the spin up and spin down sub-bands is induced at the FM/NM injection interface as well as within the NM material, which can then be detected as an electric signal by using a second FM stripe as spin detector. The splitting of the Fermi level decreases exponentially over distance due to the spin relaxation processes. The characteristic decay length is known as the spin diffusion length. The longer the spin diffusion length, the farther the spins can travel while maintaining their spin angular momentum. A pure spin current, that is, a flow of spins with zero net charge current, is driven by the gradient of the Fermi level splitting and flows in the NM channel away from the injection point. Such a diffusive spin current has the advantage of reduced heat dissipation compared to the charge current and is critical for spintronic ideas such as spin field effect transistor [2], all-spin logic device [7], and spin accumulation sensor [8].

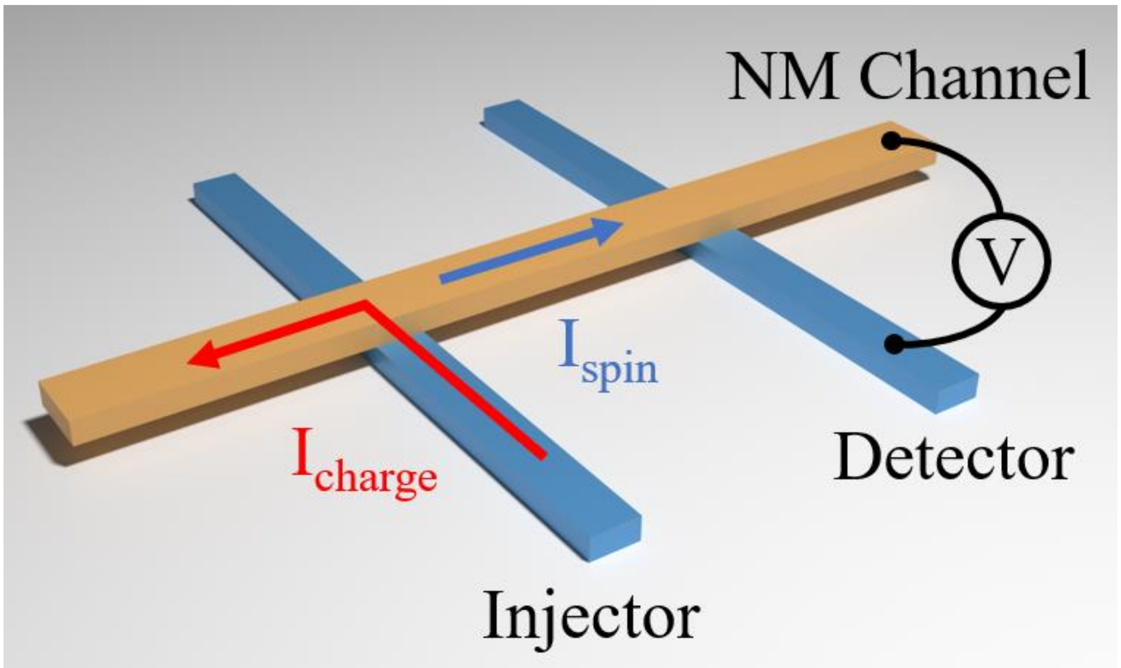

Figure 1.1: Illustration of the nonlocal spin valve geometry.

In light metals including Cu, Ag, and Al, it is widely accepted that spin relaxation is predominately due to spin-flip scatterings. Despite substantial effort to improve our understanding of the fundamental relaxation mechanisms, many questions remain open. Even in the heavily investigated Cu, the contribution and mechanism of each individual scattering source including grain boundaries, surfaces, magnetic impurities, phonons, dislocations, and large spin-orbit coupling impurities are still far from complete understanding.

The background of this thesis is provided in chapter 2, where we give a brief overview of the various magnetoresistance effects including anisotropic, giant, and tunnel magnetoresistances, which have laid the foundation of the information age by facilitating high density data storage. The discoveries of the tunnel and later giant magnetoresistances mark the beginning of spintronics. In the second part of the chapter, we introduce NLSV which plays a central role in this thesis. We explain the spin relaxation process through spin flip scatterings, which is the predominat relaxation mechanism in Cu. Finally, we present the spin dependent electrochemical potentials and the spin signals in NLSVs with transparent and tunnel interfaces by considering the diffusion equation with proper boundary conditions. We leave the discussion of the low resistance oxide interface situation to the following chapter.

In chapter 3, we demonstrate efficient spin transport by exploring Cu channels with cross section of 0.5×0.5 μm^2, which is substantially larger than the typical cross section of $< 0.2 \times 0.2$ μm^2 from previous studies [9-12]. These channels demonstrate significantly improved electrical conductivity, residual resistivity ratio, and spin diffusion length. 14 NLSVs fabricated in a single batch yield an average spin diffusion length of 3.2 μm at 30 K, considerably longer than the previously reported values [9-12]. The greatly improved spin diffusion length can be explained by the suppression of the grain boundary and surface scatterings using the Mayadas–Shatzkes model and the Fuchs–Sondheimer model.

In chapter 4, we explore the Kondo spin relaxation mechanism due to Fe impurities in Cu host. The Kondo effect, first discovered by W. J. de Haas *et al.* in

1934 [13], has attracted attention for decades because of its many-body entanglement origin. In de Haas and his colleagues' original work, a resistivity minimum was observed around 4 K in Au wire. At the time, the decrease of the resistivity of metal upon cooling, which is due to the suppression of lattice vibration, was well documented, however an increase of Au resistivity below 4 K was unexpected. Later experiments confirmed that this abnormality is due to the existence of dilute magnetic impurities in the host metals. A theoretical model successfully explaining the phenomenon was proposed by Jun Kondo in 1964 [14]. From the second Born approximation, a resistivity contribution proportional to $\log\left(\frac{1}{T}\right)$, which gives rise to the upturn as T approaches 0, is obtained from the antiferromagnetic *s*-*d* exchange interaction between the impurity spin and the conduction spins of the host metal. The Kondo resistivity upturn is illustrated in Figure 1.2.

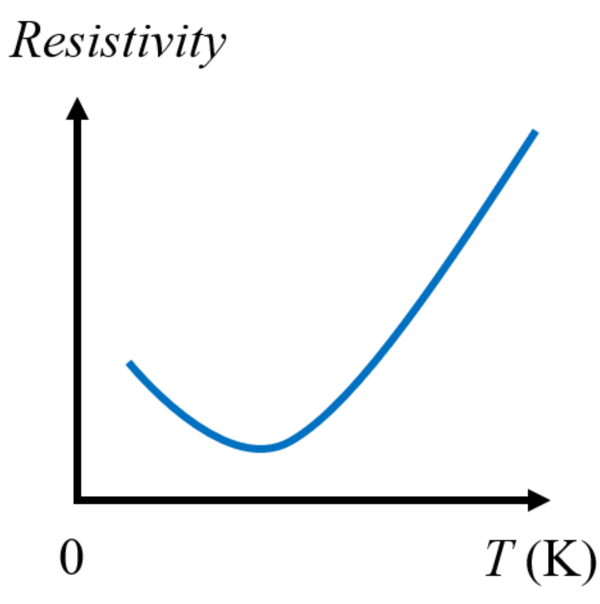

Figure 1.2: Illustration of the Kondo resistivity upturn.

Despite the Kondo effect being relatively well understood and becoming a text-book subject in many-body physics, many questions remain to be answered, specifically the existence of the Kondo screening cloud and the interaction among overlapping clouds are among the critical issues that need to be addressed. Essentially a Kondo screening cloud is an electron cloud that masks the localized impurity spin with opposite overall spin polarization. The Kondo screening cloud is particularly difficult to detect because of its extremely dilute spin density, ~ 1 Bohr magneton per $(100\ \mathrm{nm})^3$ volume for Fe impurities in Cu host. The first experimental observation of the elusive Kondo screening cloud was reported by Borzenets et al. in 2020 by using a quantum-dot system [15]; however, evidence of the clouds in metals is still lacking.

We studied the relation between the Kondo spin relaxation rate ${\tau_{sK}}^{-1}$ and the Kondo momentum relaxation rate ${\tau_{eK}}^{-1}$ using 20 NLSVs with submicron Cu channels that contain dilute Fe impurities. After carrying out the spin and charge transport measurements of each NLSV under various temperatures between 5 to 100 K, we systematically extracted ${\tau_{sK}}^{-1}$ and ${\tau_{eK}}^{-1}$ of each device. For any given NLSV, our data shows a linear relation between the two quantities under varying temperature. However, as the Fe impurity concentration C_{Fe} changes among 20 devices, ${\tau_{sK}}^{-1}$ remains nearly a constant despite ${\tau_{eK}}^{-1}$ varying by a factor of 10. The ratio between ${\tau_{sK}}^{-1}$ and ${\tau_{eK}}^{-1}$ gives the Kondo spin relaxation probability, which has been previously reported to be a constant of 0.34 by Batley et al. [16] and 0.7 by Kim et al. [17] Our data demonstrates that while this probability is a constant under varying temperature for a particular device with a specific C_{Fe}, it varies from 0.045 to 0.44 under varying impurity concentration.

This surprising finding could be understood by considering the overlapping of nearby Kondo clouds. The size of a single cloud, theoretically predicted to be ~ 100 nm in diffusive Cu channels, is significantly larger than the average distance between adjacent Fe impurities, which is estimated to vary between 10 to 20 nm based on the impurity concentration (1-12 ppm) of our Cu channels. Therefore, many Kondo clouds heavily overlap in Cu, thus forming a continuous Kondo medium throughout the channel. Each single cloud acts as a momentum scattering barrier as well as a spin scattering barrier for conduction electrons passing through them. The increase of impurity concentration will enhance the momentum scattering, but not necessarily the spin relaxation because the spin polarizations of the Kondo clouds are randomly oriented, thus the spin density of nearby clouds may cancel out. In fact, our data suggests the spin density of the medium is nearly constant within the 1-12 ppm concentration range. This work could open up new possibilities to study the Kondo screening cloud, including probing its spatial extension in low concentration regime, as well as understanding the coupling between magnetic impurities mediated by the clouds in high concentration regime.

In chapter 5, we demonstrate the tunable spin relaxation in Cu by using the ionic gating technique. A lateral gate is patterned a few micrometers away from the Cu channel of a NLSV. We then apply a Li^+ ion containing solid polymer electrolyte to immerse both the gate and the channel. The Li^+ ion concentration at the surface of the channel can be controlled by the gate voltage: a positive gate induces high Li^+ concentration while a negative gate depletes the Li^+ ion. We observed suppressed spin relaxation under positive gate and enhanced spin relaxation under negative gate. At room temperature, the spin diffusion length and the Cu resistivity can be reversibly tuned by 23% and 7%, respectively, while at 5 K, these tunabilities increase to 43% and 9%. In addition, the strength of the Kondo effect due to the Fe impurities, which sensitively depends on the chemical environment of the impurity, is tuned by one order of magnitude. Finally, we also observed a gradual amplification of the tuning ranges by repeated gate cycling which clearly suggests an electrochemical origin. We hypothesize the reversible diffusion of Li along the Cu grain boundaries to be the origin of the observed tuning effects. In polycrystalline metals, grain boundaries act as potential barriers which can induce momentum scatterings and therefore spin relaxation. Under positive gate, Li diffuse into the grain boundaries, which reduces the potential barrier, hence spin relaxation is suppressed. Under negative gate, the reverse process happens, and the spin relaxation is recovered. The controllable spin relaxation demonstrates the broader potential of metallic spintronics.

REFERENCES

[1] S. Jung *et al.*, Nature **601**, 211 (2022).

[2] S. Datta and B. Das, Applied Physics Letters **56**, 665 (1990).

[3] M. N. Leuenberger and D. Loss, Physica E: Low-dimensional Systems and Nanostructures **10**, 452 (2001).

[4] C. Chappert, A. Fert, and F. N. Van Dau, Nature Materials **6**, 813 (2007).

[5] D. Saha, M. Holub, P. Bhattacharya, and D. Basu, in *Comprehensive Semiconductor Science and Technology*, edited by P. Bhattacharya, R. Fornari, and H. Kamimura (Elsevier, Amsterdam, 2011), pp. 563.

[6] M. Johnson and R. H. Silsbee, Physical Review Letters **55**, 1790 (1985).

[7] B. Behin-Aein, D. Datta, S. Salahuddin, and S. Datta, Nature Nanotechnology **5**, 266 (2010).

[8] M. Yamada, D. Sato, N. Yoshida, M. Sato, K. Meguro, and S. Ogawa, IEEE Transactions on Magnetics **49**, 713 (2013).

[9] F. J. Jedema, A. T. Filip, and B. J. van Wees, Nature **410**, 345 (2001).

[10] T. Kimura, T. Sato, and Y. Otani, Physical Review Letters **100**, 066602 (2008).

[11] H. Zou and Y. Ji, Applied Physics Letters **101**, 082401 (2012).

[12] E. Villamor, M. Isasa, L. E. Hueso, and F. Casanova, Physical Review B **87**, 094417 (2013).

[13] W. J. de Haas, J. de Boer, and G. J. van dën Berg, Physica **1**, 1115 (1934).

[14] J. Kondo, Progress of Theoretical Physics **32**, 37 (1964).

[15] I. V. Borzenets, J. Shim, J. C. H. Chen, A. Ludwig, A. D. Wieck, S. Tarucha, H. S. Sim, and M. Yamamoto, Nature **579**, 210 (2020).

[16] J. T. Batley, M. C. Rosamond, M. Ali, E. H. Linfield, G. Burnell, and B. J. Hickey, Physical Review B **92**, 220420 (2015).

[17] K. W. Kim, L. O'Brien, P. A. Crowell, C. Leighton, and M. D. Stiles, Physical Review B **95**, 104404 (2017).

Chapter 2

MAGNETORESISTANCE EFFECTS AND NONLOCAL SPIN VALVE

The origin of spintronics dates back to the 1970s when the tunnel magnetoresistance effect was first observed by Michel Jullière using magnetic tunnel junctions [1]. Since the 1980s the field has attracted enormous attention following the discovery of the giant magnetoresistance effect [2,3] as well as the demonstration of the spin injection from ferromagnet into nonmagnet using a geometry later known as the nonlocal spin valve [4]. The giant magnetoresistance together with the tunnel magnetoresistance technologies have helped to revolutionize the data storage industry by increasing the areal density of the hard disk drive (HDD) from ~ 100 MB/in^2 in the early 90s [5] to over 1.3 TB/in^2 since 2015. As of today, HDDs are widely used in data centers as the most reliable and cost-effective solution, laying the foundation of the fast-growing digital world. The field of spintronics has been under intensive study ever since as emerging spintronic nanodevices offer novel functionalities [6-8] and hold the potential to achieve efficient computation, data transfer and data storage, and are of particular interest in the field of neuromorphic computing [9]. In this chapter, we will give a brief introduction to the various magnetoresistance effects and the nonlocal spin valve which is an ideal structure to study the pure spin current as well as its induced phenomenon and plays a central role in this thesis.

2.1 Magnetoresistance

The magnetoresistance (MR) effect refers to the alteration in the electrical resistance of a material when subjected to an externally applied magnetic field. Magnetoresistance $\Delta R/R_0$ is defined as:

$$\frac{\Delta R}{R_0} = \frac{R(H) - R_0}{R_0} \tag{2.1}$$

where $R(H)$ is the resistance of the material under magnetic field H, and R_0 is the resistance under zero field. There are a variety of MR effects originating from vastly distinct mechanisms, including ordinary magnetoresistance (OMR), anisotropic magnetoresistance (AMR), Giant magnetoresistance (GMR), tunnel magnetoresistance (TMR), colossal magnetoresistance (CMR), and extraordinary magnetoresistance (EMR). The typical percentage change in resistance varies from a few percent for AMR, to an astonishing 1,000,000% for EMR. In the first half of this chapter, we will provide a brief overview of the AMR, GMR and TMR effects, which serve as the cornerstones of spintronics.

2.1.1 Anisotropic magnetoresistance

Anisotropic magnetoresistance (AMR), discovered by William Thomson in 1856 [10], is a phenomenon observed in ferromagnetic (FM) materials where the electrical resistance depends on the angle between the electric current and the magnetization directions of the material. AMR arises from the spin-orbit interaction, which was first suggested by Smit [11]. Although the magnetic moment arising from the exchange interaction is intrinsically isotropic, the presence of the spin-orbit interaction introduces a second-order correction term in the magnetization, which scales with the square of the spin-orbit interaction [12,13]. The magnitude of the magnetization is closely related to the density of hole states that conduction electrons can scatter into, hence an anisotropic magnetization leads to an anisotropic momentum scattering. Therefore, as the magnetization is rotated relative to the electric current by an external magnetic field, its magnitude, and consequently the scattering rate and resistance will vary [14].

The first hard disk drive using an AMR based reader was produced by IBM (9345 DASD system) in 1990, replacing the standard inductive readers at the time which were having difficulties in keeping pace with the increasing data storage density due to various engineering limitations. Beside the data storage industry, the effect also found its application in many other areas such as magnetometers [15], position sensors [16], accelerometers [17], and even flow meters. Permalloy (Py), a nickel–iron magnetic alloy, is the most common AMR material for these types of sensors because of its relatively large magnetoresistance, low saturation field (~5-10 Oe) required to obtain the effect, and its compatibility with the fabrication processes of the silicon based integrated circuits [18]. For magnetic field measurement, the AMR sensors have shown better sensitivities than the Hall sensors with 10 nT resolution [19].

Consider a polycrystalline magnetic thin stripe made of Py as illustrated in Figure 2.1 (a), the easy axis (EA) is along the long axis of the stripe due to the shape anisotropy. In the absence of external magnetic field, the magnetization of the stripe is along the EA, which is the energetically favorable direction of the spontaneous magnetization. When a magnetic field $\vec{H}$ is applied transverse to the EA, the magnetization $\vec{M}$ starts to tilt. If the current density $\vec{J}$ is along the stripe, the tilted magnetization will result in a decrease of the electrical resistance. The resistance can be described by the following relation:

$$R(\varphi) = R_{\perp} + (R_{\parallel} - R_{\perp})cos^2\varphi \tag{2.2}$$

where φ is the angle between the current and the magnetization directions, $R_{\parallel}$ and $R_{\perp}$ are the resistances when $\varphi = 0$ and $\pi/2$, respectively. When the magnetization of the ferromagnet is fully rotated to be perpendicular to the current direction, the resistance reaches its minimum. A sketch of the angle dependence of the resistance is shown in Figure 2.1 (b). For Py, the magnitude of the MR is on the order of 2% in a field of a few Oe at room temperature [20].

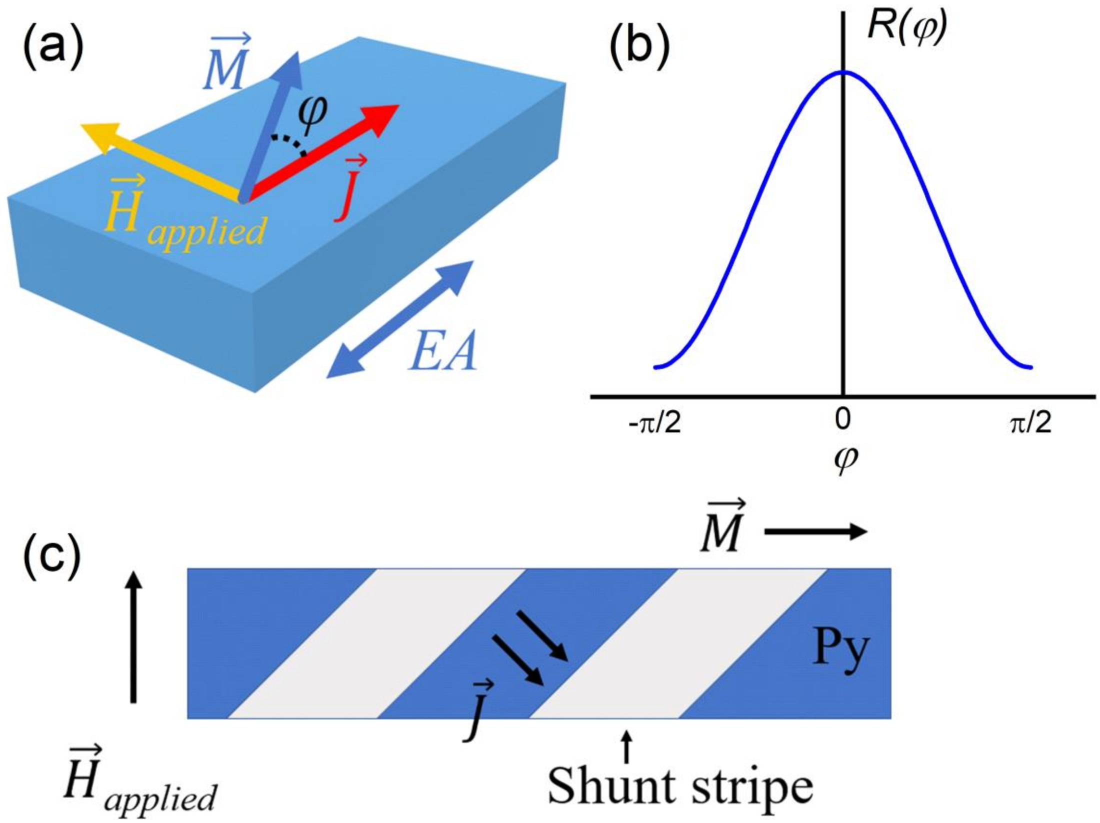

Figure 2.1: (a) Sketch of the ferromagnetic stripe. (b) Resistance of the stripe versus φ, the angle between the current density direction and the magnetization. (c) Barber-pole design with highly conductive diagonal stripes patterned on top of Py bar, forcing the current in the bare Py region to flow diagonally.

Practical magnetic sensor applications such as read heads in HDDs require a unique response under the positive and the negative external fields. In addition to having poor sensitivity, the geometry in Figure 2.1 (a) cannot detect the polarity of the external field because of the symmetrical response of the resistance with respect to $\vec{H}_{applied}$. A linear response with high sensitivity can be achieved if the magnetization under zero external field is at 45° with respect to the current direction, as can be seen from the plot in Figure 2.1 (b). This is commonly achieved by using the Barber-pole biasing design shown in Figure 2.1 (c). Diagonal stripes made of highly conductive metals, such as Cu, Al, Au, are patterned onto a Py bar, which has horizontal magnetization under zero field. When a voltage is applied across the sensor, a single shunt stripe is approximately equipotential and different stripes have different potentials. Thereby, the current flows diagonally in the bare Py region, making an angle of 45° with the magnetization direction, thus a highly sensitive and linear response to the vertically applied external field is realized.

2.1.2 Giant magnetoresistance

The giant magnetoresistance effect (GMR) was found to be much larger than the AMR effect and is therefore, named “giant”. It is a quantum mechanical phenomenon based on multilayers of alternating magnetic and nonmagnetic (NM) thin films. GMR results from the interplay between electron transport and the magnetic ordering of the materials. It was discovered in 1988 independently by the teams led by Albert Fert from the University of Paris-Sud, France, and Peter Grunberg from Forschungszentrum Julich, Germany [2,3]. While both teams’ works were based on Fe/Cr magnetic multilayers, the GMR effect has also been observed in many other magnetic and nonmagnetic multilayers, such as Co/Cu [21], and NiFe/Cu [22]. The discovery of the GMR effect leads to the breakthrough in hard disk drive technology by enabling fast (to the order of 100 ps) detection of minute magnetic bits, which helps to vastly increase the data storage density. In less than 10 years since the discovery of the phenomenon, IBM released the first GMR based heads Deskstar 16GP Titan in 1997. The success of the GMR effect demonstrates how fundamental physics research can lead to technological innovations and commercial products. Both researchers were awarded the Nobel Prize in Physics in 2007 for their pioneering works.

Peter Grunberg's experiment is based on the epitaxially grown monocrystalline Fe-Cr-Fe tri-layer thin film on GaAs substrate. The layers are fabricated as thin stripes, with a 1 nm thick Cr spacer layer separating the two 12 nm thick Fe layers. Due to the shape anisotropy, the easy axes of the 2 Fe layers are in plane and along the long axes of the stripes. The coupling between the two Fe layers is antiferromagnetic when the thickness of Cr is below 3 nm due to the indirect exchange interaction through the Cr layer [2]. Hence the magnetizations of the Fe layers are aligned antiparallel and along the easy axes when no external magnetic field is applied. It was observed that the electrical resistance of the tri-layer is higher under such antiparallel (AP) configuration, and lower when the two Fe layers are aligned parallel (P) by an external magnetic field. The percentage change was measured to be around 1.5% at room temperature, more than one order of magnitude stronger than the AMR effect measured from a single Fe film with thickness identical to that of the tri-layer, which is 0.13% as reported by the researchers [3]. The effect becomes stronger when the number of Fe layer increases, a change of 3% was achieved using structure with 3 Fe layers separated by 2 Cr layers.

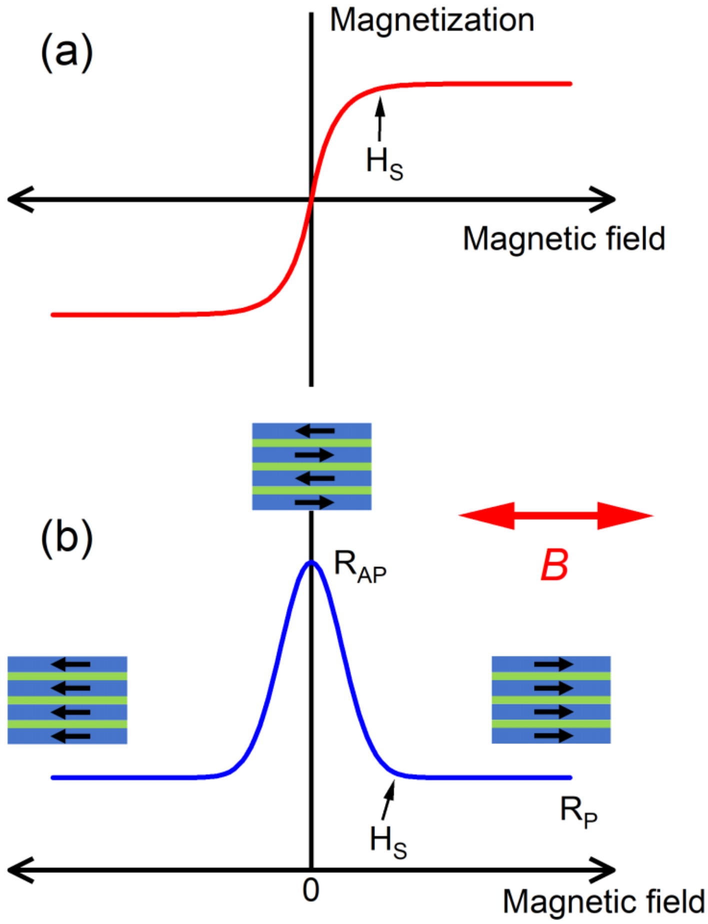

Figure 2.2: Schematic representation of the GMR effect. (a) Magnetization of the superlattice versus the applied field. (b) Resistance of the superlattice versus the applied field. The sketches illustrate the individual magnetization of each Fe layers in the superlattice. H_S is the saturation field.

Albert Fert's experiment, on the other hand, utilizes Fe/Cr superlattice, with up to 60 repetitions of the Fe/Cr bi-layer structure prepared by molecular-beam epitaxy. Samples with different thickness of Cr layer were studied. The largest effect was observed for the thinnest Cr layers with thickness equals to 9 Å. Resistance can be reduced, strikingly, by 50% using a magnetic field at 4.2 K. The effect was named giant magnetoresistance by the researchers because of the large magnetoresistance compared with the typical value of the AMR effect.

Figure 2.2. illustrates the main finding of Fert's experiment. The top and bottom panels show the total magnetization and the total resistance of the superlattice versus the applied magnetic field, respectively. Under zero applied field, the coupling between adjacent Fe layers is antiferromagnetic as illustrated by the alternating arrows in the sketch in Figure 2.2 (b), hence the overall magnetization is zero and the resistance is high. As the magnitude of the applied field increases, the magnetizations of the Fe layers start to be aligned along the field direction and the resistance of the superlattice decreases. The total magnetization approaches a constant and the resistance reaches its minimum above the saturation field H_S.

The GMR effect can be qualitatively explained by Mott's two-current model proposed by N. F. Mott in 1936 [23]. First off, the electric current in typical metals is carried by the spin up and spin down electrons independently, because during a scattering event the probability for the spin of the electron to flip is typically much smaller than the probability for the spin to be conserved. In cobalt, for example, the momentum relaxation time is 3 fs while the spin relaxation time is as long as 400 fs. [14] Therefore, roughly speaking it takes more than 100 momentum scatterings for the spin to flip. In copper more than 1000 momentum scatterings are required for the spin to flip [24]. Hence, in most metals an electron can maintain its spin angular momentum for a long time, so approximately there are two independent spin up and spin down conduction channels in metals, and the total resistance can be treated as two resistive channels connected in parallel as illustrated in Figure 2.3, where $R_\uparrow$ and $R_\downarrow$ represent the resistance of the up and down channels, respectively. This physical picture of two parallel conduction channels has been confirmed experimentally by Fert and Campbell by carefully measuring the resistivity of Ni doped with transition metal impurities at low temperatures [25].

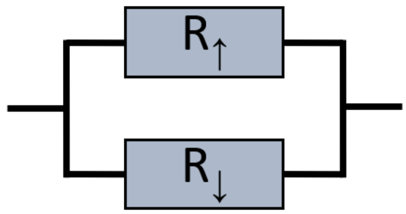

Figure 2.3: Schematic diagram of the Mott model. $R_\uparrow$ and $R_\downarrow$ represent the spin up and spin down channels, respectively.

Secondly, the momentum scattering rate is spin dependent. In ferromagnets including Fe, Co, and Ni, both the 3d and 4s electrons are valence electrons and can conduct electricity. However, the electric current is primarily carried by the s electrons because, compared with them, the d electrons have much larger effective mass when the d band is approximated as free-electron band. Therefore, the d electrons are less mobile, and the conductivities of these transition metals are dominated by the scattering mechanisms of the s electrons. On the other hand, the band structure is exchange-split due to the exchange interaction in these metals. The d band splitting is of the order of 1 eV. The s band splitting is much smaller than the d band and may even has opposite sign. Consequently, the density of states (DOS) of the d electrons (and holes) of the two spin sub-bands are different at the Fermi level. Lastly, according to Fermi's golden rule, the scattering rate is proportional to the DOS at the energy of the final state, therefore the two spin sub-bands of the 4s electrons have

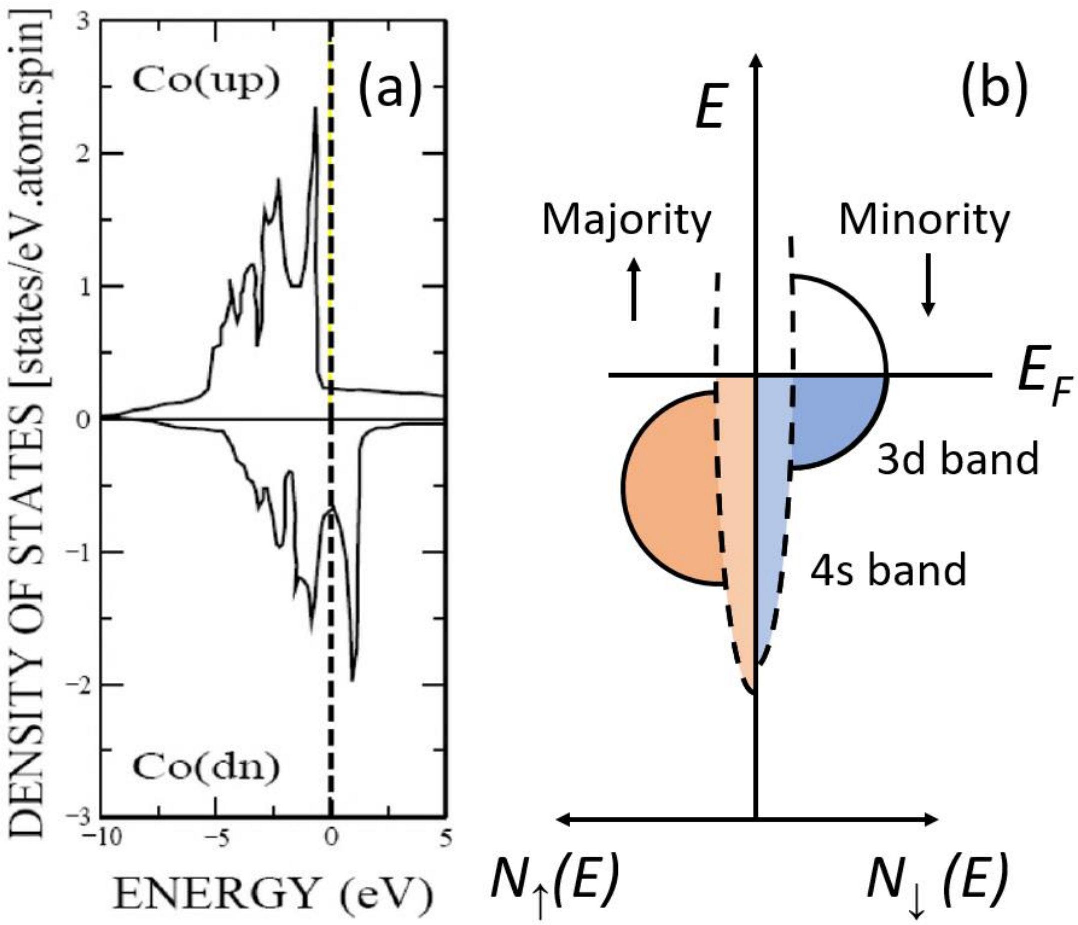

Figure 2.4: (a) Spin dependent DOS of cobalt from ab-initio calculation. The Fermi energy as indicated by the dashed line is taken to be 0. Reprinted with permission from [26]. (b) Sketch illustrating the DOS in Co and Ni. The 4s bands are represented by parabolas and the 3d bands are represented by semicircles.

different scattering rates or, equivalently, the resistances of the two conduction channels differ. Figure 2.4 (a) shows the DOS of cobalt from *ab-initio* calculation [26]. Figure 2.4 (b) gives a qualitative illustration of the DOS of both cobalt and nickel. In this simplified picture, there are no available 3d states for the majority (up) band at the Fermi level, while there are plenty of available states for the minority (down) 4s spins to scatter into, thus the minority spins have a higher s → d transition rate, resulting in a higher resistivity than the majority spins. Please note this physical picture is overly simplified as the hybridization of d states with s-p states is completely ignored. Density functional theory calculation has shown the d states can extend to energies more than 10 eV above the Fermi energy when the hybridization is taken into account [14].

Equipped with the Mott model, we are now ready to understand the GMR effect by considering the spin dependent scatterings in the FM layers. The structure that the GMR effect is based on is known as the spin valve. Figure 2.5. illustrates a simple spin valve where one NM (e.g., Cu) layer is sandwiched by two FM (e.g., Co) layers. The total resistance of the structure, as discussed above, can be described by a spin up channel connected in parallel with a spin down channel, and each spin channel can be considered as two resistances connected in series because the resistance contribution from the NM layer is generally small so can be neglected here. Note we are also ignoring the interface resistances for simplicity. In the subscript of the resistance symbol R in Figure 2.5 (c) and (d), the first arrow represents the spin direction of the conduction channel, and the second represents the direction of the majority spin of the ferromagnet. The positive (up) direction is defined as pointing to the right. From Figure 2.4 (b), we can readily see $R_{\uparrow,\downarrow} = R_{\downarrow,\uparrow} > R_{\uparrow,\uparrow} = R_{\downarrow,\downarrow}$.

When an external magnetic field above the saturation field is applied to the spin valve, the two FM layers will be aligned parallel, as illustrated in Figure 2.5 (a). The spin up electrons can now pass through both layers easily with few momentum

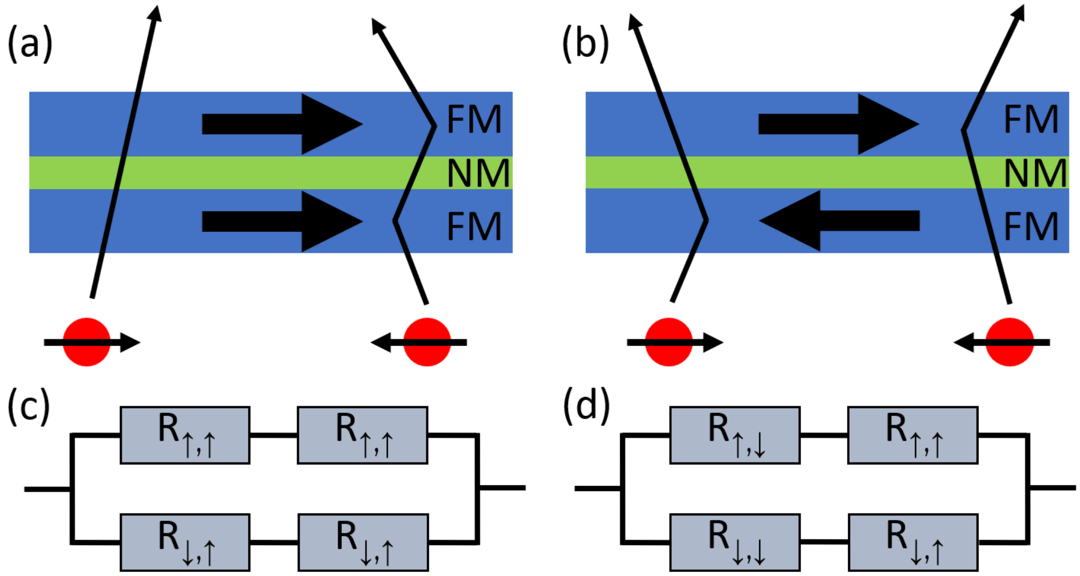

Figure 2.5: Schematic diagram of the spin valve structure where a nonmagnetic layer is sandwiched by two ferromagnetic layers. The two FM layers are aligned parallel in (a), and antiparallel in (b). The arrows in the FM layers represent the direction of the majority spins. (c) and (d) show the resistances of the spin valves as illustrated in (a) and (b), respectively. $R_{\uparrow,\uparrow}$ and $R_{\downarrow,\downarrow}$ represent the resistances of the conduction channels that are parallel to the majority spin of the FM films and have small values due to the lower scattering rates. $R_{\uparrow,\downarrow}$ and $R_{\downarrow,\uparrow}$ represent the resistances of the conduction channels that are antiparallel to the majority spin of the FM films and have large values due to the higher scattering rates.

scattering, therefore, the spin up channel shows small resistance. On the other hand, the spin down electrons experience strong momentum scattering in both layers, thus resulting in a large resistance for the spin down channel. The overall resistance of the spin valve will be small because of the small resistance from the spin up channel, since the two channels are connected in parallel. Quantitively the spin up channel has a resistance of $2R_{\uparrow,\uparrow}$ and the spin down channel has a resistance of $2R_{\downarrow,\uparrow}$. The total resistance can be easily calculated as $2R_{\uparrow,\uparrow}R_{\downarrow,\uparrow}/(R_{\uparrow,\uparrow}+R_{\downarrow,\uparrow})$. When no external magnetic field is applied, the two FM layers will be aligned antiparallel due to the indirect exchange coupling as illustrated in Figure 2.5 (b). In this configuration, both spin up and spin down channels will show large resistances due to the strong momentum scattering in one of the magnetic layers, thus resulting in a large overall resistance for the spin valve. Quantitively the two spin channels have equal resistance of $R_{\uparrow,\uparrow} + R_{\downarrow,\uparrow}$, and the total resistance of the spin valve is $\frac{1}{2}(R_{\uparrow,\uparrow} + R_{\downarrow,\uparrow})$. Following simple algebra, the GMR ratio can be shown as:

$$GMR \coloneqq \frac{\Delta R}{R_P} = \frac{R_{AP} - R_P}{R_P} = \frac{(R_{\uparrow,\uparrow} - R_{\uparrow,\downarrow})^2}{4R_{\uparrow,\uparrow}R_{\uparrow,\downarrow}} \tag{2.3}$$

With the growing demand for HDD with larger capacity and lower cost, the size of the magnetic domains (bits) in the HDD storage media continues to shrink. However smaller domains produce smaller magnetic fields which in turn lead to smaller signal output from the reader. In addition to having low signal to noise ratio for small magnetic domains, it is also challenging to reduce the physical dimensions of the AMR readers. GMR readers on the other hand are remarkably smaller than AMR readers and have been proved to be highly sensitive for weak magnetic fields. The MR ratio of the GMR readers are typically around 8% [27,28] compared with only 2% for AMR readers [20]. In practical applications, the NM spacer layer in the spin valve has to be thick enough to reduce the coupling between the two FM layers so that even a weak field can switch them between parallel and antiparallel alignments. GMR readers replaced AMR readers in the late 90s and helped to boost the data storage density by roughly two orders of magnitude [29].

2.1.3 Tunnel magnetoresistance

The discovery and successful application of the GMR effect lead to an increased interest in a related effect, namely the tunnel magnetoresistance effect. It was first reported by Michel Jullière in 1975 [1]. Despite being discovered earlier than GMR, TMR did not draw much attention initially. The experiment was based on Fe/Ge/Co junctions. Germanium is a good insulator under low temperatures. Similar to the aforementioned spin valve structure where one nonmagnetic metallic layer is sandwiched by two ferromagnetic layers, here we have the so-called magnetic tunnel junction (MTJ) where one insulating layer is sandwiched by two ferromagnetic layers. The TMR effect is named for the quantum mechanical tunneling of the conduction electrons through the insulating layer, which is forbidden in classical physics. The potential barrier is of the order of 100 meV in Jullière's experiment. The insulator has to be thin enough for the tunneling to happen. The barrier thickness usually ranges from a few angstroms to a few nanometers [30-33], and AlO_x and MgO are the most frequently used materials [34]. The normal TMR effect is phenomenologically similar to the GMR effect: the junction shows lower resistance when the two ferromagnets are aligned parallel and higher resistance when the two are aligned antiparallel. In simple applications, the bottom FM layer is often either grown or annealed on top of an antiferromagnetic (AFM) layer so that the exchange bias mechanism can "pin" the magnetization of the FM film. This will greatly enhance the coercive fields ($\gtrsim$ 50 mT) of the pinned layer, thereby the parallel and antiparallel configurations can be conveniently achieved by only switching the magnetization of the top (free) FM layer with small external fields.

While GMR is based on spin dependent scattering as discussed above, TMR is based on spin dependent tunneling. Similar to other MR effects, the TMR ratio is quantitatively defined as:

$$TMR \coloneqq \frac{R_{AP}-R_P}{R_P} = \frac{G_P-G_{AP}}{G_{AP}} \tag{2.3}$$

where R_P (G_P) and R_{AP} (G_{AP}) are the resistances (conductances) of the junction under parallel and antiparallel configurations, respectively. Typically, TMR shows a higher percentage change than GMR. In M. Jullière’s original experiment, a relative change of 14% was observed at 4.2 K. The magnitude of the effect has improved over the years. In 1995, T. Miyazaki et al., found 18% and 30% change under 300 K and 4.2 K, respectively using Fe/Al_2O_3/Fe MTJs [30], while in the same year J. S. Moodera et al., claimed similar fractional change in CoFe/Al_2O_3/Co or NiFe junctions: 1.8%, 20%, and 24% were reported under 295 K, 77 K, and 4.2 K, respectively [31]. The studies of the alumina MTJs have led to steady improvement of the TMR ratio, in 2007 a percentage change of 80% at room temperature was reported by H. X. Wei et al [32]. To achieve an even higher ratio, insulating materials with better quality and ferromagnetic materials with higher spin polarizations are necessary. Theoretical prediction published in 2001 suggested more than 1000% change can be achieved using epitaxial Fe/MgO/Fe(001) junction [35]. In 2008, more than 600% change at room temperature was experimentally demonstrated in annealed MgO tunnel junctions [33].

Similar to the GMR effect, the TMR effect can also be explained by considering the two parallel spin up and spin down conduction channels. With zero bias voltage applied across the insulating layer, electrons tunnel in both directions with equal rates. When a small bias voltage U is applied, a potential difference of eU across the insulator is established. As illustrated in Figure 2.6, electrons preferentially tunnel from F_1 (negative electrode) into F_2 (positive electrode). F_1 and F_2 are assumed to be made of the same material. Under small bias voltage and to the first order approximation, electrons tunnel through the insulating barrier without spin flip.

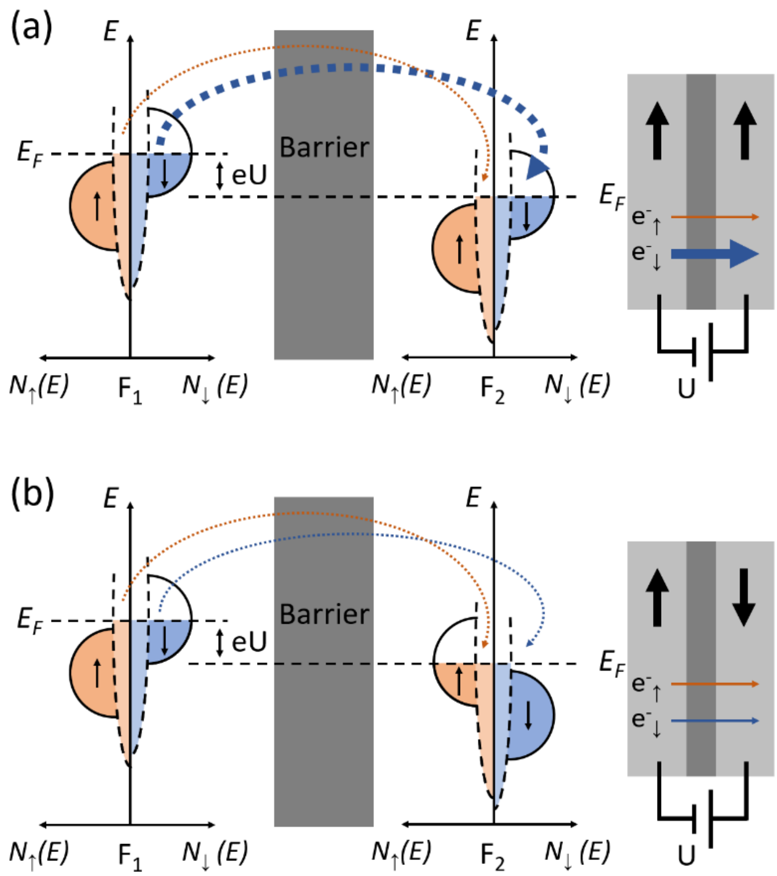

Figure 2.6: Illustration of the electron tunneling in MTJ under (a) parallel configuration and (b) antiparallel configuration. A potential energy difference of eU between F_1 and F_2 is established when a bias voltage U is applied across the insulating layer. E_F is the Fermi energy and $N_\uparrow(E)$ and $N_\downarrow(E)$ represent the DOS of spin up and spin down electrons, respectively.

Therefore, the spin up (down) electrons from F_1 can only tunnel to the spin up (down) sub-band of F_2. To be consistent with our convention in Figure 2.4, here the up and down are defined to be the majority spin and minority spin, respectively. The total current is again split into two conduction channels, just like in the GMR effect. Qualitatively speaking, according to Jullière's model, when the two ferromagnets are aligned parallel, the majority spins from F1 tunnel to the majority sub-band in F2, resulting in a small current; the minority spins from F1 tunnel to the minority sub-band in F2, resulting in a large current. The total current is large, and the MTJ shows a small resistance. On the other hand, when the two ferromagnets are aligned antiparallel, the majority spins from F1 can only tunnel to the minority sub-band of F2, and the minority spins from F1 tunnel to the majority sub-band of F2. Both conduction channels, in this case, have small currents, thus the total current is small and the MTJ shows a large resistance.

Quantitively, Jullière assumed the conductance of each spin channel is proportional to the product of the DOS of the 2 ferromagnets. Following Tedrow and Meservey's analysis [36], the MTJ conductance satisfies the following proportionalities:

$$G_P \propto a_1 a_2 + (1 - a_1)(1 - a_2) \tag{2.4.1}$$

$$G_{AP} \propto a_1(1 - a_2) + a_2(1 - a_1) \tag{2.4.2}$$

where a is the fraction of the majority spin in F_1 or F_2, and is defined as:

$$a \coloneqq \frac{N_{\uparrow}(E_F)}{N_{\uparrow}(E_F) + N_{\downarrow}(E_F)} \tag{2.5}$$

where $N_{\uparrow}(E_F)$ and $N_{\downarrow}(E_F)$ are the DOS for spin up and spin down electrons at the Fermi energy, respectively. Finally, the spin polarization P of a ferromagnet is defined as:

$$P \coloneqq \frac{N_{\uparrow}(E_F) - N_{\downarrow}(E_F)}{N_{\uparrow}(E_F) + N_{\downarrow}(E_F)} \tag{2.6}$$

Combining these equations with Eq. 2.3, the TMR ratio is deduced to be:

$$TMR = \frac{2P_1 P_2}{1 - P_1 P_2} \tag{2.7}$$

where P_1 and P_2 are the spin polarizations of F_1 and F_2, respectively. According to this simple model, as both P_1 and P_2 approach 1, the TMR ratio approaches infinity. As such, the MTJ turns into a switch and can toggle between small and infinite resistances. A ferromagnetic material with polarization equal to unity, or equivalently with all the electrons at the Fermi level aligned in the same direction, is called a half-metal. Some notable examples include magnetite, chromium(IV) oxide, and lanthanum strontium manganite (LSMO). As a comparison, for 3d transition metals including Fe, Co and Ni, the spin polarization is around 40% under cryogenic temperature measured with superconducting point contact [37].

Although Eq. 2.7 is useful for estimating the magnitude of TMR based on spin polarizations of the two ferromagnets, the model is overly simplified. From the assumption that the conductance is proportional to the DOS, one would expect the minority (down) spins of cobalt to have a higher tunneling probability than the majority because the minority d band is partially filled while the majority d band is below E_F. However, experiments have demonstrated that the probability also depends on the properties of the insulating layer. Teresa et al. found that when the barrier is strontium titanate or cerium lanthanite, minority spins indeed tunnel with higher probability, but when the insulating material changes to alumina, the minority spin tunneling probability becomes lower than the majority [38]. The results were attributed to the bonding effect at the cobalt insulator interface. In addition, the 4s and 3d electrons tunnel with different probabilities. According to Hertz et al. s electrons should tunnel more easily than d electrons due to the projection of the wavefunction into the insulating layer [39].

Compared with GMR read head sensors, TMR read head sensors demonstrate higher MR ratios, yielding superior signal to noise ratio (SNR). In addition, TMR sensors generate less heat thanks to MTJ's larger resistance, thereby providing better lifetime performance. In 2005, Seagate introduced the first HDD using TMR based read head with 400 GB capacity. The performance has been further improved by transition from amorphous AlO_x insulator to crystalline MgO insulator lattice matched to the adjacent ferromagnets. Besides magnetic sensors, TMR has also found its application in magnetoresistive random access memory (MRAM) which is essentially a transistor connected with an MTJ. MRAM is a promising alternative to the current dynamic random access memory (DRAM) and has advantages in terms of faster read and write operations, lower heat dissipation, nonvolatility and durability.

2.2 Nonlocal spin valve

The early successful examples of spintronics, GMR and TMR, led to the technological successes of high-density HDD as well as prototypes of MRAMs [6-8]. As the field of spintronics evolved over the last few decades, more concepts, ideas, and phenomena emerged with a broad range of potential applications in information storage and processing. One group of ideas involve the injection, transportation, detection, and utilization of spin current in nonmagnetic channels [40-42]. Such systems often involve several ferromagnetic electrodes that are in contact with a NM chancel and serve as spin injectors or detectors. The lateral layout of these structures resembles a conventional field effect transistor and thus leaves open the possibility of a spintronic field effect transistor [43]. Because of the partial separation of the charge injection current and the spin current, these systems are generally known as the nonlocal/lateral spin valves (NLSV) today. The key challenge of NLSV is that the injected spin current decays exponentially over distance in the NM channel. The characteristic decay length is the spin diffusion length. A long spin diffusion length is desired for spintronic applications.

The electrical spin injection and detection in a NM material was first demonstrated by Mark Johnson and R. H. Silsbee in 1985 by sending a spin polarized current from a thin (65 nm) Py film into an aluminum bar with a large cross section ($50 \times 100\ \mu m^2$) sliced from bulk aluminum [4]. The experiment was carried out under low temperatures up to 55 K and ~ 100 pV signals were detected. The spin diffusion lengths of 2 samples at 4.3 K were extracted to be 170 and 450 μm. In the early 2000s, Jedema et al. applied the ideas to micro-fabricated Py/Cu/Py lateral structures. Rather than sliced from the bulk, the Cu wire was first defined by electron-beam lithography and then deposited by electron-beam evaporation and had much smaller physical dimensions (cross section ~ 50×100 nm^2). Room temperature electrical spin injection was realized and yielded greatly enhanced signals (~ 100 nV) [44]. The spin diffusion length was extracted to be 350 nm at room temperature and 1 μm at 4.2 K. The field has been under intensive study ever since to understand the fundamentals of spin transport and relaxation mechanisms and to foster spintronics innovations [40].

A scanning electron microscopy (SEM) image of a typical NLSV is shown in Figure 2.7 (a). The essential structure of a NLSV consists of two ferromagnetic stripes and a nonmagnetic channel bridging the two. The FM stripes are usually made of Fe, Co, Ni or their alloys, while the NM channel material can vary from metals (Cu, Al, Ag, Au) [44,45] to semiconductors [46] to 2D materials [47]. The 2 FM stripes, if made of the same material, often have slightly different width or thickness to facilitate magnetization switching under different applied fields. Figure 2.7 (b) illustrates the cross section of the device. A thin (usually < 5 nm) insulator (oxide) layer is inserted in between the FM and NM to enhance the spin accumulation in the NM channel [48,49]. Such an interface (FM/I/NM), if engineered properly with uniform thickness, may ideally behave as a tunnel barrier. However, even a non-uniform low-resistance oxide layer (far from an ideal tunnel barrier) can enhance the spin accumulation quite effectively as compared to a direct contact interface FM/NM (ohmic or transparent interface). This point will be elaborated in Chapter 3.

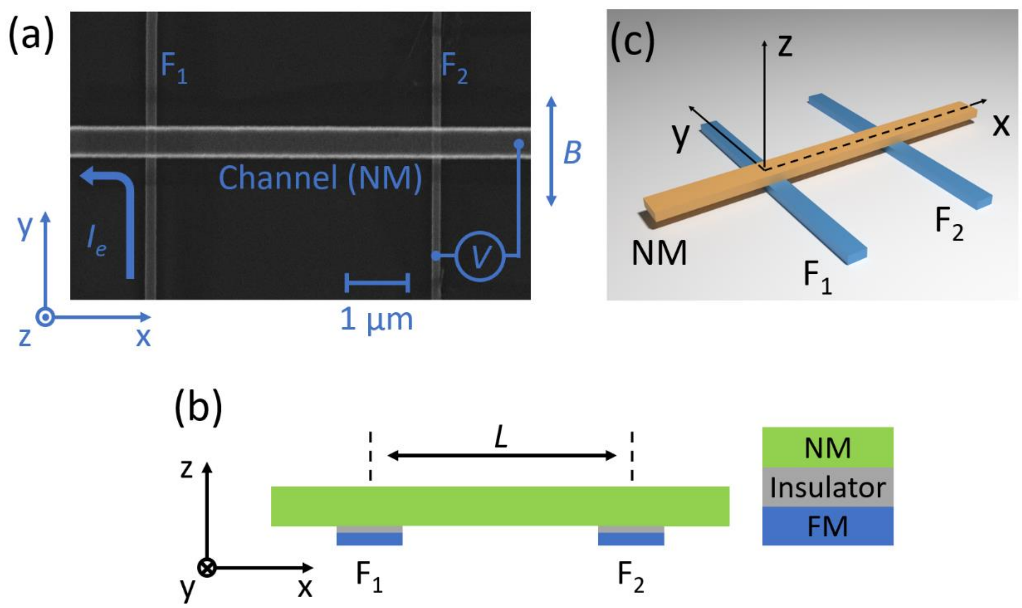

Figure 2.7: (a) SEM image of a NLSV with the spin signal measurement configuration illustrated. (b) Sketch of the cross section of the device. The length of the NM channel L is defined as the center-to-center separation of the FM stripes. (c) Illustration of the coordinate system. The origin is defined at the center of the F_1/I/NM interface. z = 0 is in the NM and adjacent to the insulating layer.

A typical measurement configuration is illustrated in Figure 2.7 (a). Electrons are injected from F_1 (spin injector) into the NM channel and extracted at the left end of the channel. The voltage drop across F_2 (spin detector) and the other end of the channel is measured. In most experiments, the easy axes of the FM stripes are along the y direction due to the shape anisotropy. An external magnetic field *B* along the stripes is used to control the magnetizations of F_1 and F_2, which can be aligned in either parallel or antiparallel configurations thanks to the slightly different coercivities of the two.

The coordinate system is shown in Figure 2.7 (c). The x and y axes are along the NM channel and the FM stripes, respectively, while the z axis is perpendicular to the plane. The origin is defined at the center of the F_1/I/NM interface. z=0 is in the NM and adjacent to the oxide layer. For simplicity, we assume the oxide has negligible thickness. These definitions will become relevant when we present a quantitative description of the spin accumulation and the spin signal in section 2.2.3.

Here we briefly explain the working principle of the NLSV using a simplified picture where both F_1 and F_2 are made of half-metals as shown in Figure 2.8 (a). In the half-metallic spin injector, only the down spins can conduct electricity and are therefore injected into the channel, which, in steady state, induces a spin accumulation at the interface (x = 0), i.e., a surplus of down spins and a deficiency of up spins. Consequently, the chemical potential of down spins increases, and that of up spins decreases at the interface. This splitting of the chemical potentials in the channel decays starting from x=0 along both +x and -x directions due to the spin relaxation processes. The spin current is proportional to the gradient of the chemical potential difference. Therefore, to the right-hand side of F_1 only spin current flows in the channel with zero charge current, making the NLSV an ideal structure to study pure spin current and its induced phenomenon such as spin transfer torque and inverse spin hall effect [41,42].

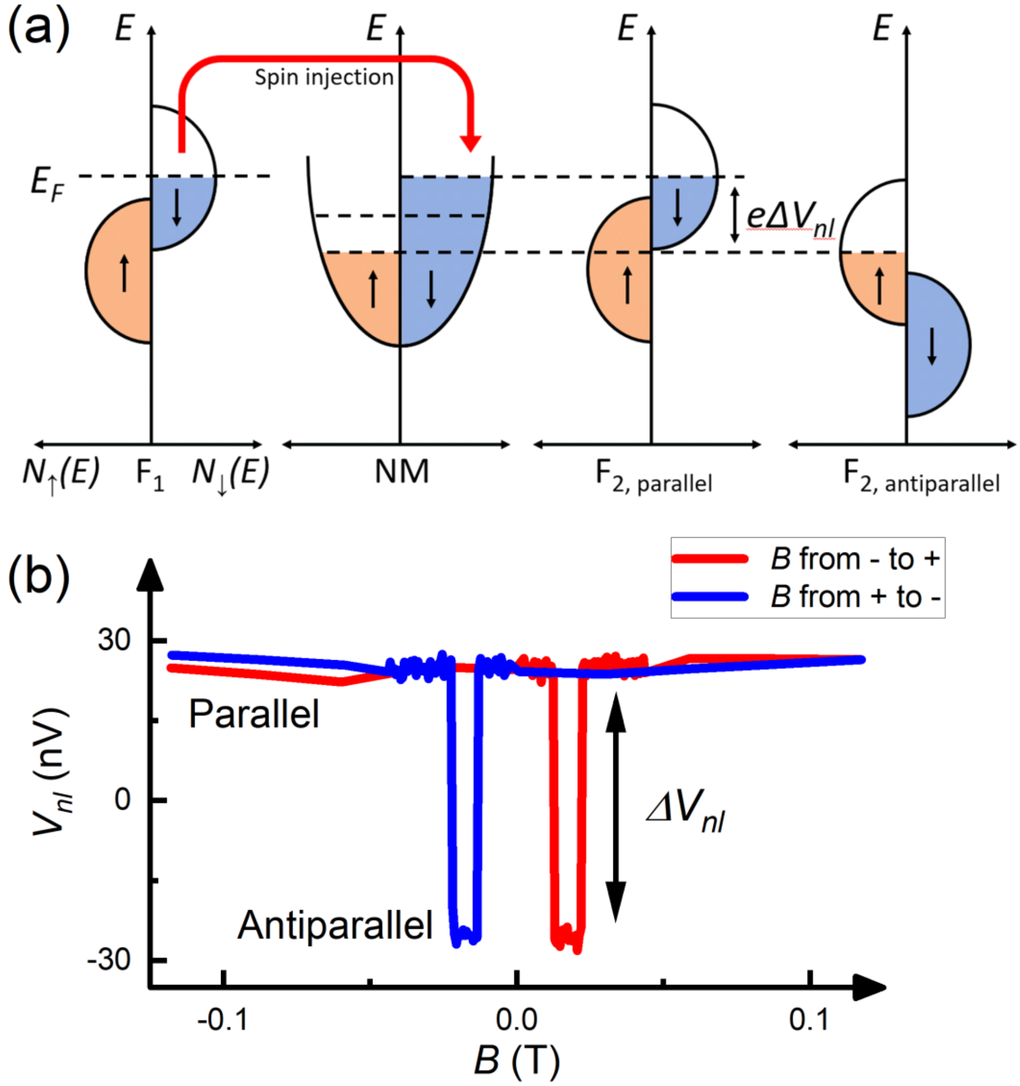

Figure 2.8: (a) Illustration of the spin injection and detection in a NLSV with half-metallic spin injector and detector. (b) The nonlocal voltage V_{nl} as a function of the applied field B. The red curve is for scanning the B field from negative to positive and the blue curve is for the reverse scan.

The spin detector is used to probe the split chemical potentials in the channel. When F_2 is parallel to F_1, as all the charge carriers are down spins in F_2, its Fermi level must be aligned to the chemical potential of down spins in the channel. Therefore, the voltmeter measuring the voltage drop across F2 (the down spin chemical potential) and the far right end of the channel (the equilibrium chemical potential) yields a positive reading. Similarly, when F2 is antiparallel to F1, its Fermi level is aligned to the up spin chemical potential and a negative voltage is measured. The difference between the two readings (ΔV_{nl}) is proportional to the splitting of the chemical potentials ($e \cdot \Delta V_{nl}$) at the detection point in the channel. A nonzero ΔV_{nl} provides evidence of the unequal up and down chemical potentials.

Figure 2.8 (b) shows a typical NLSV measurement where the nonlocal voltage (V_{nl}) is measured as a function of the applied field *B*. Initially F_1 and F_2 are aligned parallel by a large negative field (~ -0.1 T) and the nonlocal voltage shows a positive value. As the magnetic field is scanned from negative to positive (red curve), the FM stripe with smaller coercivity flips its magnetization first leading to the antiparallel configuration of F_1 and F_2, and a sharp drop of V_{nl} is observed. Further increasing the magnetic field flips the second FM stripe and the positive V_{nl} is recovered under the parallel configuration. The blue curve shows the reverse process when the *B* field is scanned from positive back to negative.

The spin signal is defined as $\Delta R_s = \Delta V_{nl}/I$, where I is the injection current. From the one dimensional diffusion equation, the spin signal of a NLSV with low resistance oxide barriers is derived as [50]:

$$\Delta R_s = \frac{P_1 P_2 \rho_N \lambda_N}{A_N} e^{-L/\lambda_N} \tag{2.8}$$

where P_1 and P_2 are the effective spin polarizations of F_1 and F_2, respectively. ρ_N, A_N, and λ_N are the electrical resistivity, cross-sectional area, and spin diffusion length of the NM channel. L is the length of the channel and is defined as the center-to-center separation of F_1 and F_2. By adjusting the position of F_2, the exponential dependence of the spin signal on L can be observed.

At room temperature, ΔV_{nl} in a NLSV with typical physical dimensions is to the order of 0.1 μV. Assuming the channel length is twice the spin diffusion length, the largest chemical potential difference in the channel, which occurs at the injection point, is to the order of 1 μeV, which is only a small fraction of the room temperature thermal energy $k_B T_{room} = 26$ meV. Note this is a very rough estimation as the spin detector is usually made of ferromagnetic materials which are less efficient than half-metals at measuring the chemical potential difference, plus the spin detector often absorbs the spin accumulation in the channel. Both factors make the 1 μeV an underestimate of the actual chemical potential difference at the injection point. Nevertheless, suffice it to say that the spin accumulation from electrical spin injection in metals is only a small perturbation to the chemical potentials of the spin sub-bands, and has negligible impact on the DOS at the spin dependent Fermi levels, nor does it affect the transport properties such as conductivity and momentum relaxation time.

2.2.1 Spin relaxation through spin-flip scattering

Various mechanisms can lead to spin relaxation including spin dephasing, spin selective absorption, and spin-flip scattering. In light metals including Cu, Ag and Al, it is widely accepted that spin-flip scattering is predominately responsible for the spin relaxation, which is dominated by the Elliott-Fafet (EY) spin relaxation mechanism [51,52]. The EY mechanism applies to metals as well as semiconductors with inversion symmetry, weak spin-orbit coupling and low quasi-particle scattering rate. In these light metals, itinerant electrons scatter off sources such as impurities, dislocations, phonons, grain boundaries, and surfaces, which is known as the momentum scattering event. During such an event, a spin polarized electron has a small probability (usually $<10^{-3}$ for most scattering sources [24]) to flip its spin. The collective spin flips of all the conduction electrons, including both up to down and down to up transitions, result in the reduction of the spin accumulation over time, because overall more electrons transition from the surplus spin state into the deficient spin state.

Consider a piece of metal with nonzero spin accumulation at time $t = 0$ as illustrated in Figure 2.9 (a). We define $\tau_{\uparrow\downarrow}$ to be the average time for an up spin to transition into down spin, and $\tau_{\downarrow\uparrow}$ to be the average time of the reverse process. From the continuity equation and assuming no electrons enter or leave the region of interest, the deviations of electron densities (electrons per space volume) from equilibrium $\delta n_\uparrow$ and $\delta n_\downarrow$ satisfy the following coupled differential equations:

$$\frac{d\delta n_\uparrow}{dt} = -\frac{\delta n_\uparrow}{\tau_{\uparrow\downarrow}} + \frac{\delta n_\downarrow}{\tau_{\downarrow\uparrow}} \tag{2.9.1}$$

$$\frac{d\delta n_\downarrow}{dt} = \frac{\delta n_\uparrow}{\tau_{\uparrow\downarrow}} - \frac{\delta n_\downarrow}{\tau_{\downarrow\uparrow}} \tag{2.9.2}$$

Solving Eq. 2.9, we find the spin accumulation decays exponentially over time:

$$\delta n_\uparrow(t) = \frac{\tau_{\uparrow\downarrow}}{\tau_{\uparrow\downarrow}+\tau_{\downarrow\uparrow}}\left(\delta n_\uparrow^0 - \frac{\tau_{\downarrow\uparrow}}{\tau_{\uparrow\downarrow}}\delta n_\downarrow^0\right)e^{-t/\tau_s} \tag{2.10.1}$$

$$\delta n_\downarrow(t) = -\frac{\tau_{\uparrow\downarrow}}{\tau_{\uparrow\downarrow}+\tau_{\downarrow\uparrow}}\left(\delta n_\uparrow^0 - \frac{\tau_{\downarrow\uparrow}}{\tau_{\uparrow\downarrow}}\delta n_\downarrow^0\right)e^{-t/\tau_s} \tag{2.10.2}$$

where $\delta n_\uparrow^0$ and $\delta n_\downarrow^0$ are the electron density deviations at time $t = 0$. We assume the metal is charge neutral, so $\delta n_\uparrow^0 + \delta n_\downarrow^0 = 0$. τ_s is the spin relaxation time, and is defined as:

$$\tau_s{}^{-1} = \tau_{\uparrow\downarrow}{}^{-1} + \tau_{\downarrow\uparrow}{}^{-1} \tag{2.11}$$

For nonmagnetic metals, $\tau_{\uparrow\downarrow} = \tau_{\downarrow\uparrow}$ and Eq. 2.10 reduce to:

$$\delta n_\uparrow(t) = \delta n_\uparrow^0 e^{-t/\tau_s} \tag{2.12.1}$$

$$\delta n_\downarrow(t) = \delta n_\downarrow^0 e^{-t/\tau_s} \tag{2.12.2}$$

The spin relaxation in metals happens on the time scale of sub-nanosecond. For Cu at cryogenic temperatures, as illustrated in chapter 4, the optimal τ_s is on the order of 100 ps [24]. The exponential decay of $\delta n_\uparrow$ and $\delta n_\downarrow$ in NM metals is illustrated in Figure 2.9 (b).

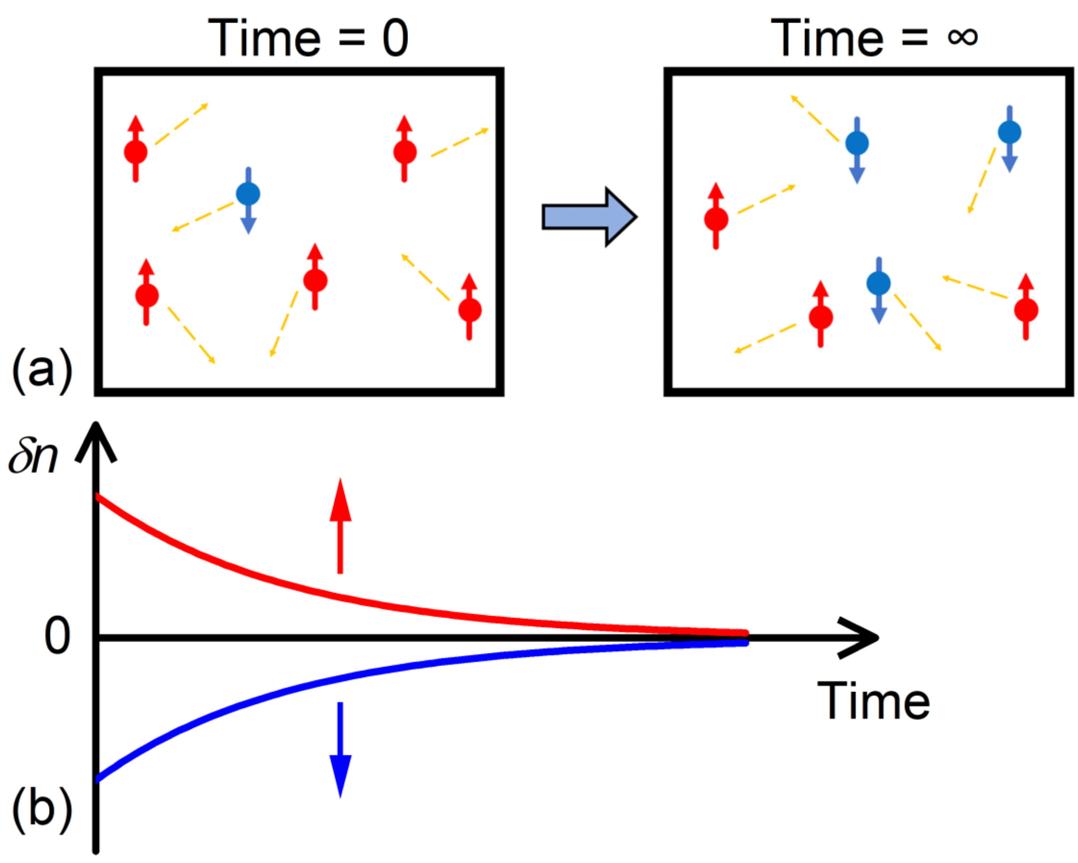

Figure 2.9: (a) Illustration of the spin relaxation in NM metal (e.g., Cu). (b) $\delta n_\uparrow$ and $\delta n_\downarrow$ exponentially decays towards the equilibrium with time constant τ_s.

2.2.2 Electrochemical potentials in FM/NM heterostructure

In this section we consider the electrochemical potential energies (ECP) in FM/NM heterostructures in steady state based on the two-current model. As discussed previously, the validity of the two-current model comes from the fact that spin flips are usually sufficiently rare during scattering events in both FM and NM metals. Throughout this and the next sections, we assume the DOS of the ferromagnets are consistent with Figure 2.4 (a).

The spin dependent ECP is the sum of the electric and chemical potentials:

$$\mu_{\uparrow,\downarrow} = -e\varphi + \delta\varepsilon_{\uparrow,\downarrow} \tag{2.13}$$

where $\delta\varepsilon_{\uparrow,\downarrow}$ are the chemical potential deviations from equilibrium, e is the electron charge, and φ is the electric potential. The equilibrium Fermi level E_F and the electric potential at the origin in the NM $\varphi_{NM}(0)$ are set to 0. As illustrated in Figure 2.10, the origin is defined at the FM/NM interface.

The electric current density $\boldsymbol{j}$ can be driven by either an electric field $\boldsymbol{E}$ (from the voltage supplied) or a gradient of the carrier density as described by Fick's law of diffusion:

$$\boldsymbol{j}_{\uparrow,\downarrow} = \sigma_{\uparrow,\downarrow}\boldsymbol{E} + eD_{\uparrow,\downarrow}\nabla\delta n_{\uparrow,\downarrow} \tag{2.14}$$

where $\sigma_{\uparrow,\downarrow}$ and $D_{\uparrow,\downarrow}$ are the conductivities and diffusion constants. The first term is the contribution from drift, and the second term is the contribution from diffusion.

The total conductivity is the sum of the conductivities of the two spin sub-bands: $\sigma = \sigma_\uparrow + \sigma_\downarrow$. In nonmagnet $\sigma_N^\uparrow = \sigma_N^\downarrow = \frac{1}{2}\sigma_N$, while in ferromagnet $\sigma_F^\uparrow > \sigma_F^\downarrow$, as we discussed in the GMR section. $\sigma_{\uparrow,\downarrow}$ and $D_{\uparrow,\downarrow}$ satisfy Einstein's relation:

$$\sigma_{\uparrow,\downarrow} = e^2 N_{\uparrow,\downarrow} D_{\uparrow,\downarrow} \tag{2.15}$$

$N_{\uparrow,\downarrow}$ denote the spin dependent DOS at the Fermi level.

The electron density deviations $\delta n_{\uparrow,\downarrow}$ are proportional to the chemical potential deviations $\delta\varepsilon_{\uparrow,\downarrow}$:

$$\delta n_{\uparrow,\downarrow} = N_{\uparrow,\downarrow}\delta\varepsilon_{\uparrow,\downarrow} \tag{2.16}$$

which is valid because, as discussed, the chemical potential deviations induced by the electrical spin injection are small perturbations, so the DOS remain approximately constant within the range of $\delta\varepsilon_{\uparrow,\downarrow}$.

From Eq. 2.13 to Eq. 2.16, one finds a linear proportionality between the current densities and the gradients of the ECP:

$$\boldsymbol{j}_{\uparrow,\downarrow} = \frac{\sigma_{\uparrow,\downarrow}}{e}\nabla\mu_{\uparrow,\downarrow} \tag{2.17}$$

The charge current density is obviously $\boldsymbol{j} = \boldsymbol{j}_\uparrow + \boldsymbol{j}_\downarrow$, while the spin current density is defined as $\boldsymbol{j}_s = \boldsymbol{j}_\uparrow - \boldsymbol{j}_\downarrow$.

Making use of Eq. 2.17, the electric potential energy (which is also the equilibrium chemical potential) $\bar{\mu}$, is found to be a weighted average of $\mu_\uparrow$ and $\mu_\downarrow$:

$$\nabla\bar{\mu} = \frac{e}{\sigma}\boldsymbol{j} = \frac{e}{\sigma}(\boldsymbol{j}_\uparrow + \boldsymbol{j}_\downarrow) = \frac{\sigma_\uparrow}{\sigma}\nabla\mu_\uparrow + \frac{\sigma_\downarrow}{\sigma}\nabla\mu_\downarrow$$

Integrating both sides yields:

$$\bar{\mu} = \frac{\sigma_\uparrow}{\sigma}\mu_\uparrow + \frac{\sigma_\downarrow}{\sigma}\mu_\downarrow \tag{2.18}$$

In FM $\mu_F^\uparrow$ weighs more than $\mu_F^\downarrow$, whereas in NM $\mu_N^\uparrow$ and $\mu_N^\downarrow$ have equal weights. These unequal weightings on the two sides of the FM/NM interface has important implications that we will see in a moment.

Figure 2.10 illustrates the current densities and ECP when electrons are injected from ferromagnet into nonmagnet through a transparent contact. In the absence of an injection current, there is no spin accumulation and $\bar{\mu} = \mu_\uparrow = \mu_\downarrow = 0$ throughout the FM/NM structure. When the current first turns on, the electric field drives more up spins than down spins to the interface from the FM side because $\sigma_F^{\uparrow} > \sigma_F^{\downarrow}$, whereas an equal amount of up and down spins leave the interface from the NM side, resulting in an imbalance of the up and down spins at the interface. This spin accumulation increases over time but eventually saturates as $\nabla\delta\varepsilon_{\uparrow}$ drives up spins away from the interface into both FM and NM, while $\nabla\delta\varepsilon_{\downarrow}$ draws down spins towards the interface from both sides.

Figure 2.10 (a) shows the current densities vs position in steady state. Here a positive-valued $\boldsymbol{j}$ stands for electrons flowing to the right. The total current density $\boldsymbol{j}$ (black dash) vs position is a flat line as required by the continuity equation and the charge conservation. $\boldsymbol{j}_E^{\uparrow,\downarrow}$ (blue dash) and $\boldsymbol{j}_{SA}^{\uparrow,\downarrow}$ (red solid) are driven by the electric field ($\boldsymbol{j}_E^{\uparrow,\downarrow} = \sigma_{\uparrow,\downarrow}\boldsymbol{E}$) and the spin accumulation ($\boldsymbol{j}_{SA}^{\uparrow,\downarrow} = \frac{\sigma_{\uparrow,\downarrow}}{e}\nabla\delta\varepsilon_{\uparrow,\downarrow}$), respectively. The current densities of the up and down conduction channels (green solid) are given by $\boldsymbol{j}^{\uparrow,\downarrow} = \boldsymbol{j}_E^{\uparrow,\downarrow} + \boldsymbol{j}_{SA}^{\uparrow,\downarrow}$, and are continuous at the interface in steady state, as it has to be because of the saturation of the spin accumulation.

$\boldsymbol{j}_E^{\uparrow,\downarrow}$ remain constant for a particular conduction channel (up or down) in a specific material (FM or NM) whereas the magnitudes of $\boldsymbol{j}_{SA}^{\uparrow,\downarrow}$ drop exponentially as we move away from the interface with the characteristic length scale being the spin diffusion length, which is similar to the spin signal ΔR_s as described by Eq. 2.8. At room temperature, the FM spin diffusion length λ_F is a few nanometers for Fe, Co and Ni [53], while the NM spin diffusion length λ_N is a few hundred nanometers for Cu, Ag and Al [54]. Therefore, the magnitudes of $\boldsymbol{j}_{SA}^{\uparrow,\downarrow}$ decrease much faster in FM than in NM, as shown in Figure 2.10 (a). Using the spin dependent chemical potentials solved from the diffusion equation which will be discussed soon, one finds: 1) At any specific point throughout the FM/NM structure, $\boldsymbol{j}_{SA}^{\uparrow}$ and $\boldsymbol{j}_{SA}^{\downarrow}$ have equal magnitudes but

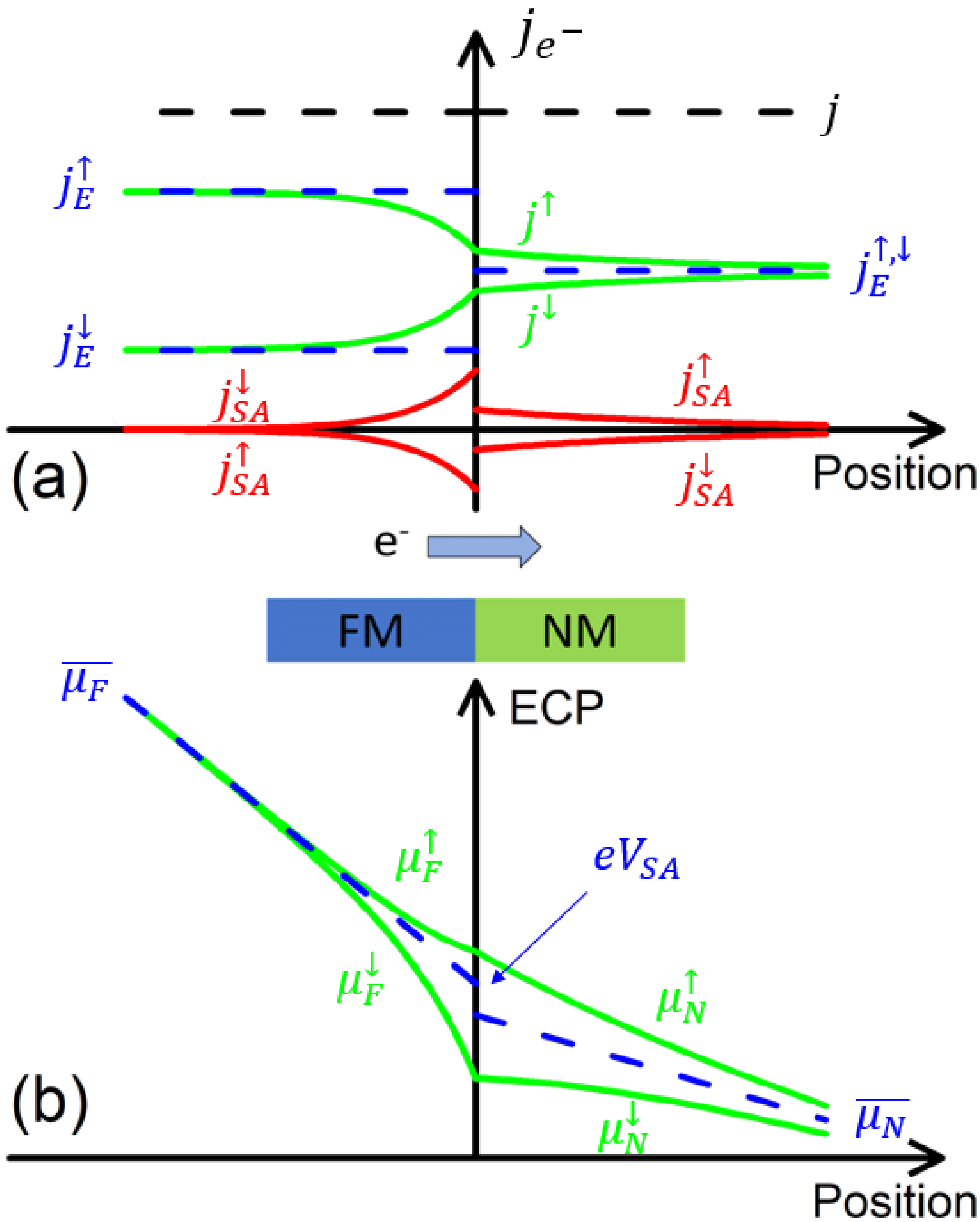

Figure 2.10: Illustration of electron injection from ferromagnet into nonmagnet through transparent contact. (a) Current densities versus position. A positive valued $\boldsymbol{j}$ represents electrons flowing to the right. $\boldsymbol{j}_E^{\uparrow,\downarrow}$ and $\boldsymbol{j}_{SA}^{\uparrow,\downarrow}$ are driven by the electric field and the spin accumulation, respectively. The spin dependent current densities are given by $\boldsymbol{j}^{\uparrow\downarrow} = \boldsymbol{j}_E^{\uparrow\downarrow} + \boldsymbol{j}_{SA}^{\uparrow\downarrow}$. (b) Spin dependent ECP $\mu^{\uparrow\downarrow}$ and electric potential energy $\bar{\mu}$ versus position.

opposite signs. 2) At the interface, the ratio of the magnitude of $\boldsymbol{j}_{SA}^{\uparrow,\downarrow}$ on the NM side (0^+) to that on the FM side (0^-) satisfies $\frac{|j_{SA}^{\uparrow,\downarrow}(0^+)|}{|j_{SA}^{\uparrow,\downarrow}(0^-)|} = \frac{\sigma_F{}^2}{4\sigma_F^{\uparrow}(\sigma_F - \sigma_F^{\uparrow})}\frac{\sigma_N/\lambda_N}{\sigma_F/\lambda_F}$, which is roughly on the order of 0.01 for common FM and NM metals used in spin valve and NLSV. This means most of the surplus up spins at the interface flow back into the FM instead of entering the NM, similarly most of the down spins that fill the deficiency at the interface are from the FM side rather than the NM side. This process is known as the spin backflow, and it results in poor spin injection efficiency. A tunnel barrier or at least low resistance oxide barrier can be used to improve the injection efficiency [48,49].

Figure 2.10 (b) shows the electrochemical potentials vs position. The green solid lines represent $\mu_{\uparrow,\downarrow}$ and the blue dashed lines represent $\bar{\mu}$. Far away from the interface, $\bar{\mu} = \mu_{\uparrow} = \mu_{\downarrow}$ with constant slopes equal to $-ej/\sigma$ according to Eq. 2.17. Near the interface, $\mu_{\uparrow} > \mu_{\downarrow}$ because of the spin accumulation, and both approach $\bar{\mu}$ exponentially due to the spin relaxation. At the interface $\mu_{\uparrow,\downarrow}$ are continuous because the interface conductances $G_I^{\uparrow,\downarrow} \to \infty$ for transparent contact. This can be understood essentially from Ohm's law:

$$A_I \cdot \boldsymbol{j}_{\uparrow,\downarrow} = -G_I^{\uparrow,\downarrow}\frac{\mu_F^{\uparrow,\downarrow}(0^-) - \mu_N^{\uparrow,\downarrow}(0^+)}{e} \qquad (2.19)$$

where A_I is the area of the interface. Since the left side of the equation is finite, $\mu_F^{\uparrow,\downarrow}(0^-) - \mu_N^{\uparrow,\downarrow}(0^+)$ must be 0.

A discontinuity of the electric potential energy $\bar{\mu}$ at the interface naturally arises from the different weights of $\mu_{\uparrow}$ and $\mu_{\downarrow}$ in FM and NM [55]. The energy gap eV_{SA} is given by:

$$eV_{SA} = \overline{\mu_F}(0) - \overline{\mu_N}(0) = \left(\frac{\sigma_F^{\uparrow}}{\sigma_F} - \frac{1}{2}\right)[\mu_{\uparrow}(0) - \mu_{\downarrow}(0)] \qquad (2.20)$$

V_{SA} is the spin accumulation induced voltage and can be shown to be proportional to the current density. Imagine a ferromagnet with resistance of 1 Ω is put in contact with a nonmagnet with the same resistance and a current of 1 A is passed through the FM/NM structure, one will find the total voltage drop across the structure is somewhat larger than 2 V because of V_{SA}. The buildup of an interfacial voltage is a rather common phenomenon. An analogous situation is the normal metal - superconductor junction (e. g. Cu – Pb) [56]. The conversion from normal current into supercurrent also gives rise to a potential gap at the interface.

In addition to the spin accumulations there are also charge accumulations both in the FM and at the interface. To understand the origin of the former, we start from Eq. 2.18, it can be easily shown that the ratio of the chemical potential deviations satisfies $\frac{|\delta\varepsilon_\uparrow|}{|\delta\varepsilon_\downarrow|} = \frac{\sigma_\downarrow}{\sigma_\uparrow}$. However, charge neutrality requires $\frac{|\delta\varepsilon_\uparrow|}{|\delta\varepsilon_\downarrow|} = \frac{N_\downarrow}{N_\uparrow}$ according to Eq. 2.16. In FM in general $D_\uparrow \neq D_\downarrow$, consequently $\frac{\sigma_\downarrow}{\sigma_\uparrow} \neq \frac{N_\downarrow}{N_\uparrow}$ which can be seen from the Einstein relation (Eq. 2.15). Therefore, there is a charge accumulation in the FM wherever the spin accumulation is nonzero and as a result, this charge accumulation is spin polarized. On the other hand, the NM stays charge neutral because $\frac{\sigma_\downarrow}{\sigma_\uparrow} = \frac{N_\downarrow}{N_\uparrow} = 1$.

The interfacial charge accumulation originates from the different conductivities of the FM and the NM: $\sigma_F \neq \sigma_N$. From Ohm's law $\boldsymbol{j} = \sigma\boldsymbol{E}$, one can readily see that the electric field changes across the interface because $\boldsymbol{j}$ is constant throughout the FM/NM heterostructure. The nonzero $\nabla\boldsymbol{E}$ at the interface leads to a charge buildup according to Gauss's law. Such a charge accumulation is spin unpolarized and exists at any interface (e.g., Au/Cu) as far as the conductivities on the two sides are different, therefore we won't go into the details here. For a thorough discussion on the ferromagnetic and the interfacial charge accumulations and their implications, we refer the interested readers to the paper by Zhu et al [57].

2.2.3 Electrochemical potentials in NLSV

We now discuss the ECP in NLSV in steady state. We will cover 3 types of interfaces including transparent, tunnel, and low resistance oxide, whose typical resistances are 0 (ideally, but also depends on the fabrication procedure), ~ kΩ, and ~ Ω, respectively. We will first present a general expression of the spin signal ΔR_s and then discuss the limiting situations for transparent and tunnel interfaces in this section. We will leave the low resistance oxide case until chapter 3. All of the fabricated NLSVs studied in this thesis (chapter 3 – 5) have this type of interface with alumina serving as the oxide layers.

Applying the continuity equation to both the spin up and the spin down conduction channels, one obtains the following equations under steady state (i.e., $d\delta n_{\uparrow,\downarrow}/dt = 0$):

$$\nabla \cdot \boldsymbol{j}_{\uparrow} = e\frac{\delta n_{\uparrow}}{\tau_{\uparrow\downarrow}} - e\frac{\delta n_{\downarrow}}{\tau_{\downarrow\uparrow}} \tag{2.21.1}$$

$$\nabla \cdot \boldsymbol{j}_{\downarrow} = -e\frac{\delta n_{\uparrow}}{\tau_{\uparrow\downarrow}} + e\frac{\delta n_{\downarrow}}{\tau_{\downarrow\uparrow}} \tag{2.21.2}$$

Using these two equations and Eq. 2.15 to Eq. 2.17, as well as the detailed balance principle, which requires $\frac{N_{\uparrow}}{\tau_{\uparrow\downarrow}} = \frac{N_{\downarrow}}{\tau_{\downarrow\uparrow}}$ because in equilibrium the up to down and the down to up transitions balance out, the diffusion equation can be derived as:

$$\nabla^2(\mu_{\uparrow} - \mu_{\downarrow}) = \lambda^{-2}(\mu_{\uparrow} - \mu_{\downarrow}) \tag{2.22}$$

where the spin diffusion length $\lambda = \sqrt{D\tau_s}$. D is the spin averaged diffusion constant and is given by $D^{-1} = (N_{\uparrow}{D_{\downarrow}}^{-1} + N_{\downarrow}{D_{\uparrow}}^{-1})/(N_{\uparrow} + N_{\downarrow})$. τ_s is the spin relaxation time and was defined in Eq. 2.11.

The diffusion equation governs the ECP in both the ferromagnetic electrodes and the nonmagnetic channel. Denoting the width and thickness of the FM electrodes by w_F and t_F, and those of the NM channel by w_N and t_N, the following inequality holds in a NLSV with typical physical dimensions and common FM and NM materials: $\lambda_F \ll t_F \ll (w_F, w_N, t_N) \ll \lambda_N$. As a result, the electrochemical potentials only vary along the z direction in F_1 and F_2, whereas in the NM channel the variations are along the x direction. The coordinate system was illustrated in Figure 2.7 and described in the paragraph below it. With the electric potential at the origin set to 0, the solution to Eq. 2.22 in the NLSV are constructed as follows:

$$\mu_{\uparrow,\downarrow}(x) = \frac{eI}{\sigma_N A_J} x \pm a_1 e^{\frac{x}{\lambda_N}} \mp a_2 e^{\frac{x-L}{\lambda_N}} \qquad NM\ (x < 0)$$

$$\mu_{\uparrow,\downarrow}(x) = \pm a_1 e^{-\frac{x}{\lambda_N}} \mp a_2 e^{\frac{x-L}{\lambda_N}} \qquad NM\ (0 < x < L)$$

$$\mu_{\uparrow,\downarrow}(x) = \pm a_1 e^{-\frac{x}{\lambda_N}} \mp a_2 e^{-\frac{x-L}{\lambda_N}} \qquad NM\ (x > L)$$

$$\mu_{\uparrow,\downarrow}(z) = eV_1 - \frac{eI}{\sigma_F A_J} z \pm b_1 \frac{\sigma_F}{\sigma_F^{\uparrow,\downarrow}} e^{\frac{z}{\lambda_F}} \qquad F_1$$

$$\mu_{\uparrow,\downarrow}(z) = eV_2 \pm b_2 \frac{\sigma_F}{\sigma_F^{\uparrow,\downarrow}} e^{\frac{z}{\lambda_F}} \qquad F_2$$

where I is the injection current, a_1, a_2, b_1, b_2, V_1, V_2 are coefficients that need to be determined using boundary conditions. In these expressions, the constant and linear terms describe the electric potential energies, and the exponential terms describe the chemical potentials. In the NM channel, the a_1 terms are due to the spin injection at F_1 and the a_2 terms are due to the spin absorption at F_2. To solve for these unknown coefficients, the following boundary conditions are imposed at the FM/I/NM interfaces (or FM/NM in case of transparent contacts):

1. The spin up and spin down current densities need to be conserved across the interface $\boldsymbol{j}_F^{\uparrow,\downarrow} = \boldsymbol{j}_N^{\uparrow,\downarrow}$.
2. The electrochemical potentials need to satisfy Eq. 2.19.

Condition 1 is under the assumption that no spin flip occurs at the interface. For transparent contact, the implication of condition 2 is that $\mu_{\uparrow,\downarrow}$ are continuous at the interface due to the infinite interface conductances $G_I^{\uparrow,\downarrow}$, which has already been discussed in the previous section. For tunnel and low resistance oxide barriers, however, $G_I^{\uparrow,\downarrow}$ are finite. Since the current densities $\boldsymbol{j}_{\uparrow,\downarrow}$ also have to be finite, from Eq. 2.19 one readily sees that the ECP must exhibit discontinuities at the interface.

Among the six unknown coefficients, V_2 is particularly important as it is directly measurable and is related to ΔV_{nl}, the difference between the nonlocal voltages (of parallel and antiparallel alignments of F_1 and F_2), and the spin signal ΔR_s by: $V_2 = \frac{1}{2}\Delta V_{nl} = \frac{1}{2} I \Delta R_s$.

Figure 2.11 illustrates the ECP vs position in NLSV with tunnel or low resistance oxide barriers under parallel alignment of F_1 and F_2. The ECP in F_1 (blue), F_2 (red) and the NM channel (green) are shown in the same plot for visualization purpose, however it should be understood that the ECP variations are along the z direction in F_1 and F_2, and along the x direction in the NM channel, as we have already discussed. Similar to Figure 2.10 (b) in the previous section, here the solid lines represent the spin dependent ECP $\mu^{\uparrow,\downarrow}$ and the dashed lines represent the electric potential energies. Different from the transparent interface situation illustrated in Figure 2.10 (b), here $\mu^{\uparrow,\downarrow}$ exhibit discontinuities across the interfaces as required by the second boundary condition (Eq. 2.19). The inset of Figure 2.11 shows the enlarged plot of ECP vs x for x > L. eV_2 gives the difference between the electric potential energies of F_2 and the far right end of the NM channel and can be directly measured by a voltmeter as illustrated in Figure 2.7 (a).

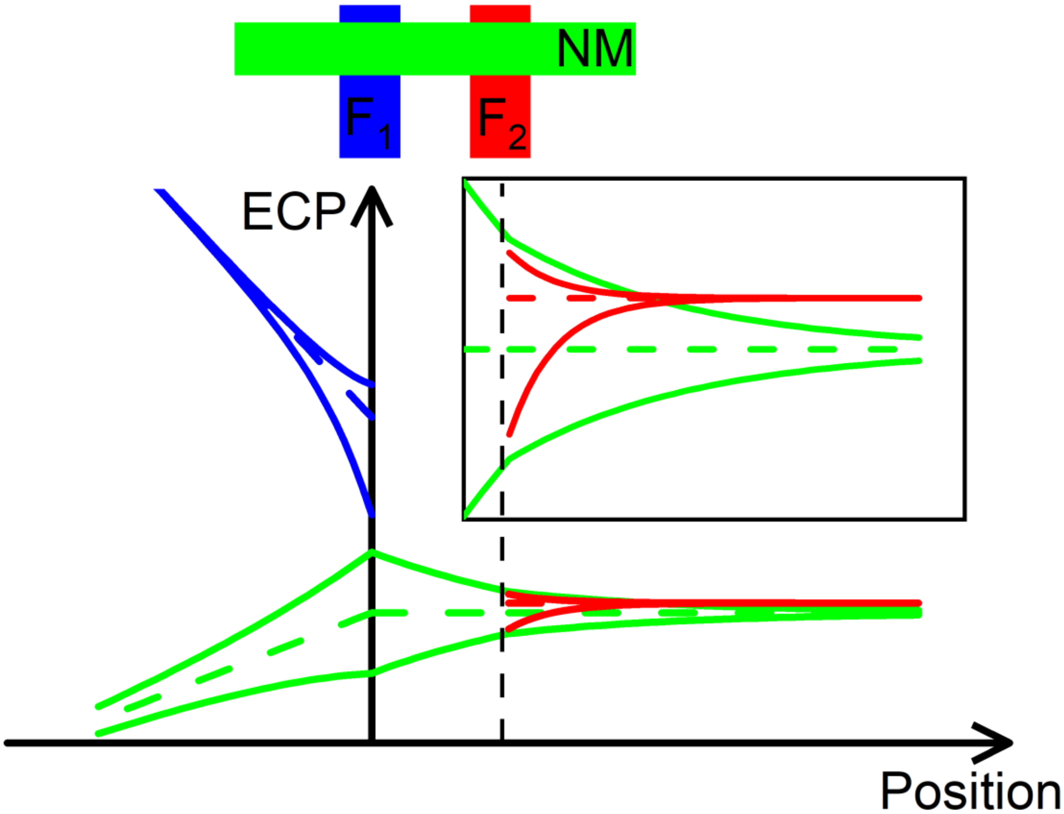

Figure 2.11: ECP in F_1 (blue), F_2 (red), and NM channel (green) versus position in NLSV with tunnel or low resistance oxide barriers under parallel alignment of the FM electrodes. The inset shows the enlarged plot for $x > L$.

Assuming:

1. F_1 and F_2 are made of the same material but have slightly different widths to easily achieve the antiparallel alignment of the two: $w_{F1} \neq w_{F2}$,

2. in case of the tunnel or low resistance oxide barrier, the oxide films at F_1 and F_2 are made of identical material with identical thickness,

the general solution of ΔR_s can be derived from V_2 as [50]:

$$\Delta R_s = 4R_{s,N} \frac{\left(P_I \frac{R_{s,I1}}{R_{s,N}} + P_F \frac{R_{s,F1}}{R_{s,N}}\right)\left(P_I \frac{R_{s,I2}}{R_{s,N}} + P_F \frac{R_{s,F2}}{R_{s,N}}\right) e^{-\frac{L}{\lambda_N}}}{\left(1 + \frac{2R_{s,I1}}{R_{s,N}} + \frac{2R_{s,F1}}{R_{s,N}}\right)\left(1 + \frac{2R_{s,I2}}{R_{s,N}} + \frac{2R_{s,F2}}{R_{s,N}}\right) - e^{-\frac{2L}{\lambda_N}}} \tag{2.23}$$

where the spin resistances R_s of the NM, the FM, and the interface are defined as:

$$R_{s,N} = \rho_N \lambda_N / w_N t_N \qquad \text{NM}$$

$$R_{s,F} = \rho_F \lambda_F / w_N w_F (1 - P_F{}^2) \qquad \text{FM}$$

$$R_{s,I} = R_I / (1 - P_I{}^2) \qquad \text{Interface}$$

Here ρ is the resistivity, $P_F = (\sigma_F^{\uparrow} - \sigma_F^{\downarrow})/\sigma_F$ is the current polarization of the FM, $R_I = G_I{}^{-1} = (G_I^{\uparrow} + G_I^{\downarrow})^{-1}$ is the interface resistance, and $P_I = |G_I^{\uparrow} - G_I^{\downarrow}|/G_I$ is the interfacial current polarization. Note both P_F and P_I should stay the same for F_1 and F_2, whereas $R_{s,I1} \neq R_{s,I2}$ and $R_{s,F1} \neq R_{s,F2}$ because by assumption the interfaces at F_1 and F_2 have different contact areas, which is the case for most experiments on NLSV.

For transparent contact, $R_{s,I} = R_I = 0$ as $G_I^{\uparrow,\downarrow} \to \infty$, $R_{s,F} \ll R_{s,N}$ because $\lambda_F \ll \lambda_N$. Eq 2.23 reduces to:

$$\Delta R_s = 4P_F{}^2 \frac{R_{s,F1} R_{s,F2}}{R_{s,N}} \frac{e^{-\frac{L}{\lambda_N}}}{1 - e^{-\frac{2L}{\lambda_N}}} \tag{2.24}$$

For tunnel junction on the other hand, $R_{s,I} \gg R_{s,N} \gg R_{s,F}$, one can easily show:

$$\Delta R_s = P_I{}^2 R_{s,N} e^{-\frac{L}{\lambda_N}} \tag{2.25}$$

Comparing Eq. 2.25 to Eq. 2.24, clearly the spin signal is greatly enhanced in NLSV with tunnel junctions because $R_{s,N} \gg R_{s,F}$.

Finally for low resistance oxide barrier, the expression of ΔR_s (given in Eq. 2.8) has the same algebraic form as the tunnel junction case but with redefined P_I. This will be discussed in detail in chapter 3.

REFERENCES

[1] M. Julliere, Physics Letters A **54**, 225 (1975).

[2] M. N. Baibich, J. M. Broto, A. Fert, F. N. Van Dau, F. Petroff, P. Etienne, G. Creuzet, A. Friederich, and J. Chazelas, Physical Review Letters **61**, 2472 (1988).

[3] G. Binasch, P. Grünberg, F. Saurenbach, and W. Zinn, Physical Review B **39**, 4828 (1989).

[4] M. Johnson and R. H. Silsbee, Physical Review Letters **55**, 1790 (1985).

[5] B. Marchon, T. Pitchford, Y.-T. Hsia, and S. Gangopadhyay, Advances in Tribology **2013**, 521086 (2013).

[6] S. Jung *et al.*, Nature **601**, 211 (2022).

[7] J. M. Daughton, Journal of Applied Physics **81**, 3758 (1997).

[8] C. Chappert, A. Fert, and F. N. Van Dau, Nature Materials **6**, 813 (2007).

[9] J. Grollier, D. Querlioz, K. Y. Camsari, K. Everschor-Sitte, S. Fukami, and M. D. Stiles, Nature Electronics **3**, 360 (2020).

[10] W. Thomson, Proceedings of the Royal Society of London **8**, 546 (1857).

[11] J. Smit, Physica **17**, 612 (1951).

[12] L. Berger, Physica **30**, 1141 (1964).

[13] A. P. Malozemoff, Physical Review B **34**, 1853 (1986).

[14] J. Stöhr and H. C. Siegmann, *Magnetism From Fundamentals to Nanoscale Dynamics* (Springer Berlin Heidelberg, Berlin, Heidelberg, 2006), 1st 2006. edn., Springer Series in Solid-State Sciences, 152.

[15] S. Tumanski, IEEE Transactions on Magnetics **20**, 1720 (1984).

[16] J. Groenland, IEEE Transactions on Magnetics **20**, 969 (1984).

[17] W. Kwiatkowski and S. Tumanski, Journal of Physics E: Scientific Instruments **19**, 502 (1986).

[18] J. Lenz and S. Edelstein, IEEE Sensors Journal **6**, 631 (2006).

[19] P. Ripka and K. Závěta, in *Handbook of Magnetic Materials*, edited by K. H. J. Buschow (Elsevier, 2009), pp. 347.

[20] P. V. Sreevidya, J. Khan, H. C. Barshilia, C. M. Ananda, and P. Chowdhury, Journal of Magnetism and Magnetic Materials **448**, 298 (2018).

[21] M. J. Hall, B. J. Hickey, M. A. Howson, M. J. Walker, J. Xu, D. Greig, and N. Wiser, Physical Review B **47**, 12785 (1993).

[22] H. Kubota, M. Sato, and T. Miyazaki, Physical Review B **52**, 343 (1995).

[23] N. F. Mott, Proceedings of the Royal Society of London. Series A - Mathematical and Physical Sciences **153**, 699 (1936).

[24] X. Shen and Y. Ji, Physical Review B **104**, 085101 (2021).

[25] A. Fert and I. A. Campbell, Physical Review Letters **21**, 1190 (1968).

[26] J. Mathon, in *Spin Electronics*, edited by M. Ziese, and M. J. Thornton (Springer Berlin Heidelberg, Berlin, Heidelberg, 2001), pp. 71.

[27] D. E. Heim, R. E. Fontana, C. Tsang, V. S. Speriosu, B. A. Gurney, and M. L. Williams, IEEE Transactions on Magnetics **30**, 316 (1994).

[28] H. Kanai, K. Yamada, K. Aoshima, Y. Ohtsuka, J. Kane, M. Kanamine, J. Toda, and Y. Mizoshita, IEEE Transactions on Magnetics **32**, 3368 (1996).

[29] J. Barnaś and V. K. Dugaev, in *Handbook of Surface Science*, edited by R. E. Camley, Z. Celinski, and R. L. Stamps (North-Holland, 2015), pp. 371.

[30] T. Miyazaki and N. Tezuka, Journal of Magnetism and Magnetic Materials **139**, L231 (1995).

[31] J. S. Moodera, L. R. Kinder, T. M. Wong, and R. Meservey, Physical Review Letters **74**, 3273 (1995).

[32] H. X. Wei, Q. H. Qin, M. Ma, R. Sharif, and X. F. Han, Journal of Applied Physics **101**, 09B501 (2007).

[33] S. Ikeda, J. Hayakawa, Y. Ashizawa, Y. M. Lee, K. Miura, H. Hasegawa, M. Tsunoda, F. Matsukura, and H. Ohno, Applied Physics Letters **93**, 082508 (2008).

[34] H. Itoh and J. Inoue, Journal of the Magnetics Society of Japan **30**, 1 (2006).

[35] J. Mathon and A. Umerski, Physical Review B **63**, 220403 (2001).

[36] P. M. Tedrow and R. Meservey, Physical Review Letters **26**, 192 (1971).

[37] R. J. Soulen *et al.*, Science **282**, 85 (1998).

[38] J. M. De Teresa, A. Barthélémy, A. Fert, J. P. Contour, F. Montaigne, and P. Seneor, Science **286**, 507 (1999).

[39] J. A. Hertz and K. Aoi, Physical Review B **8**, 3252 (1973).

[40] M. Yamada, D. Sato, N. Yoshida, M. Sato, K. Meguro, and S. Ogawa, IEEE Transactions on Magnetics **49**, 713 (2013).

[41] C. Qin, Y. Luo, C. Zhou, Y. Cai, M. Jia, S. Chen, Y. Wu, and Y. Ji, Journal of Physics D: Applied Physics **49**, 415002 (2016).

[42] Y. Cai, C. Qin, S. Chen, F. Kandaz, and Y. Ji, Journal of Physics D: Applied Physics **52**, 015002 (2019).

[43] S. Datta and B. Das, Applied Physics Letters **56**, 665 (1990).

[44] F. J. Jedema, A. T. Filip, and B. J. van Wees, Nature **410**, 345 (2001).

[45] F. J. Jedema, H. B. Heersche, A. T. Filip, J. J. A. Baselmans, and B. J. van Wees, Nature **416**, 713 (2002).

[46] X. Lou, C. Adelmann, S. A. Crooker, E. S. Garlid, J. Zhang, K. S. M. Reddy, S. D. Flexner, C. J. Palmstrøm, and P. A. Crowell, Nature Physics **3**, 197 (2007).

[47] N. Tombros, C. Jozsa, M. Popinciuc, H. T. Jonkman, and B. J. van Wees, Nature **448**, 571 (2007).

[48] Y. Cai, Y. Luo, C. Zhou, C. Qin, S. Chen, Y. Wu, and Y. Ji, Journal of Physics D: Applied Physics **49**, 185003 (2016).

[49] X. J. Wang, H. Zou, L. E. Ocola, and Y. Ji, Applied Physics Letters **95**, 022519 (2009).

[50] S. Takahashi and S. Maekawa, Physical Review B **67**, 052409 (2003).

[51] Y. Yafet, in *Solid State Physics*, edited by F. Seitz, and D. Turnbull (Academic Press, 1963), pp. 1.

[52] R. J. Elliott, Physical Review **96**, 266 (1954).

[53] K.-H. Ko and G.-M. Choi, Journal of Magnetism and Magnetic Materials **510**, 166945 (2020).

[54] J. Bass and W. P. Pratt, Journal of Physics: Condensed Matter **19**, 183201 (2007).

[55] P. C. van Son, H. van Kempen, and P. Wyder, Physical Review Letters **58**, 2271 (1987).

[56] A. B. Pippard, J. G. Shepherd, and D. A. Tindall, Proceedings of the Royal Society of London. A. Mathematical and Physical Sciences **324**, 17 (1971).

[57] Y.-H. Zhu, D.-H. Xu, and A.-C. Geng, Physica B: Condensed Matter **446**, 43 (2014).

Chapter 3

LOW TEMPERATURE SPIN DIFFUSION LENGTH EXCEEDING 3 MICROMETERS IN HIGHLY CONDUCTIVE COPPER CHANNELS

3.1 Introduction

Efficient spin transport in a nonmagnetic channel not only supports existing spintronic ideas such as spin field effect transistors [1], spin accumulation field sensors [2], or logic-in-memory devices [3], but also accommodates emerging spintronic functionalities in the future. The nonlocal spin valve (NLSV) [4-6] is the ideal system to investigate spin transport in a channel because a pure spin current can be generated and allows for an accurate detection of the spin accumulation. The spin current decays exponentially over distance in the channel and the characteristic length scale is the spin diffusion length, which becomes an important materials parameter. A large value is desired for spintronic applications.

The study of spin transport in Cu dates back to the discovery of giant magnetoresistance in Co/Cu multilayers [7] and is explored in spin transfer torque devices [8] as well. The reported values of Cu spin diffusion length λ_{Cu}, measured from NLSVs, mostly range between 400 nm and 1.3 μm at low temperatures [5,9-17]. Such a large variation clearly shows that λ_{Cu} is not simply a material constant but depends on the purity, crystallinity, and dimensions of the channel. It also challenges the accurate determination of λ_{Cu} when materials parameters vary among the set of devices used for the measurements. Furthermore, it is a crucial question whether the fabrication conditions or the device structures can be optimized to enhance λ_{Cu} further.

Our recent work indicates that larger cross sections of Cu channels lead to enhanced λ_{Cu} [18,19]. In this work, we further explore this path and demonstrate superior low temperature λ_{Cu} well above 1 μm. A set of 14 Cu based NLSV devices are fabricated on a single substrate to maintain nominally identical fabrication conditions. The Cu channels are made with square cross section of 0.5×0.5 μm^2. An average residual resistivity ratio (RRR) of 6.4 and an average λ_{Cu} of 3.2 μm at 30 K are obtained and illustrate superior electrical and spin transport properties. By using a simple approach, we are able to extract the individual λ_{Cu} value from a given device and establish their correlations with individual resistivity ρ_{cu} and RRR values. For the most conductive device, a λ_{Cu} of 5.3 μm and an RRR of 8.1 are obtained. The superior electrical and spin transport properties can be explained by the reduced grain boundary (GB) and surface scattering associated with a larger Cu cross section.

3.2 Fabrication and measurements

Fig. 3.1 (a) shows a scanning electron microscopy (SEM) image of a NLSV device, which consists of two ferromagnetic stripes (F_1 and F_2), made of $Ni_{81}Fe_{19}$ alloy (permalloy or Py), and a nonmagnetic Cu channel that bridges the two magnetic stripes. The spin injector F_1 is 160 nm wide and the spin detector F_2 is 120 nm wide. F_1 and F_2 share a common thickness of 35 nm. To achieve a long λ_{Cu}, the Cu channels are made with a larger cross-sectional area of $A_{cu} = (0.5 \times 0.5)$ μm^2. The channel length L between the centers of F_1 and F_2 varies from 1 to 5 μm with 1 μm step.

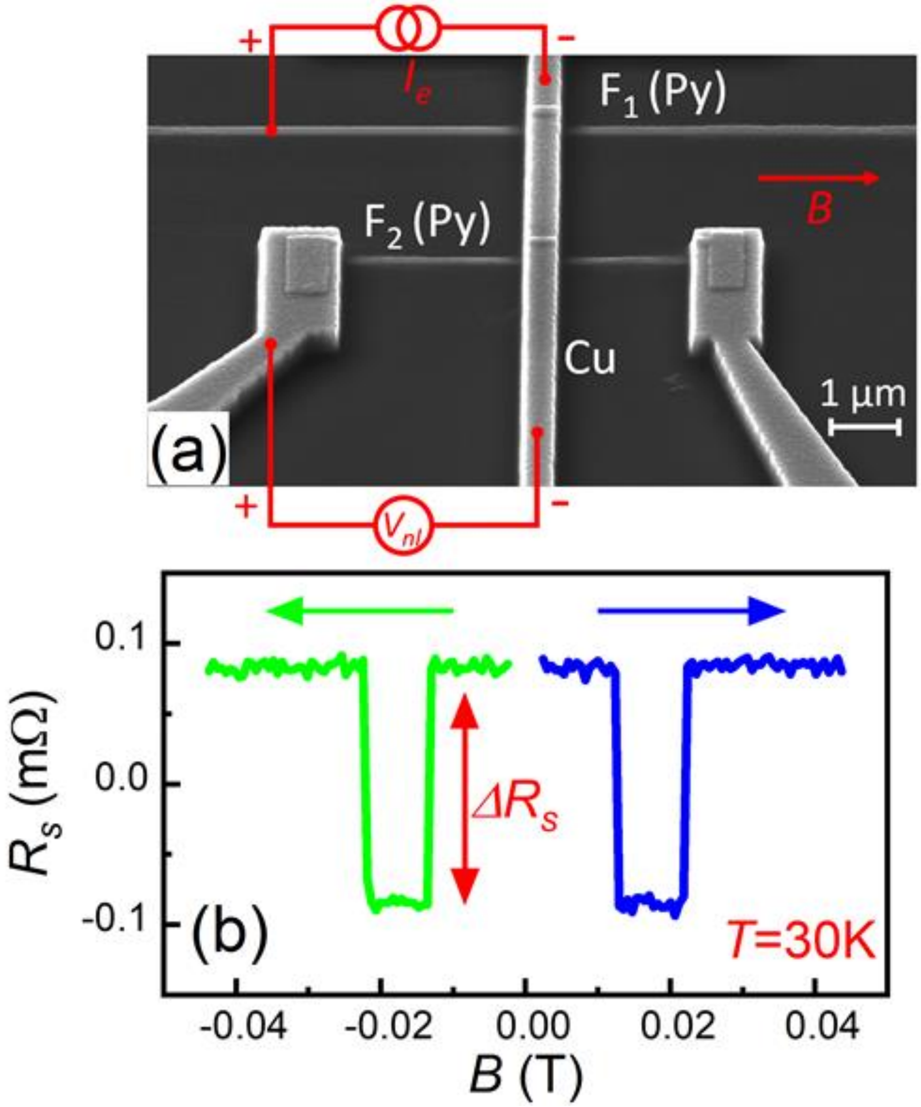

Figure 3.1: (a) SEM image of a NLSV and the measurement configuration. (b) R_s versus B plot for device 4-3 (L = 3 µm) at 30 K.

The device fabrication involves two-step electron beam lithography, with the Py stripes patterned in the first step and the Cu channel patterned in the second step. Materials are deposited by electron beam evaporation. Before the deposition of Cu (source purity of 99.999%), low energy ion-milling is applied to clean the Py surface, and 3 nm of AlO_x is inserted between Py and Cu to enhance the effective spin polarizations of F_1 and F_2 [15,20]. The deposition rates are 0.06 nm/s for Py, 0.02 nm/s for AlO_x, and 1.0 nm/s for Cu. There is no further processing after the deposition and liftoff of Cu. 15 NLSVs were fabricated on a single substrate and 14 were successfully measured for this study. All devices underwent nominally identical fabrication conditions. The geometries of the devices are identical except for the varying L values.

The measurement configuration is illustrated in Fig. 3.1 (a). Briefly, a 346 Hz AC current I_e is injected from F_1 into the Cu channel to induce a spin accumulation in Cu. A nonlocal voltage V_{nl} is detected between F_2 and the opposite end of the channel by using the lock-in method. The nonlocal spin resistance $R_s = V_{nl}/I_e$ is recorded as a function of a magnetic field B applied parallel to F_1 and F_2. The R_s versus B curve at 30 K for device 4-3 (L = 3 μm) is shown in Fig. 3.1(b), and R_s toggles between a high and a low state when F_1 and F_2 change between parallel (P) and antiparallel (AP) alignments, respectively. The different switching fields of F_1 and F_2 are caused by their different widths. The difference in R_s between the P and AP states, or the spin signal ΔR_s, is 0.17 mΩ.

Fig. 3.2 (a) and (b) show the temperature (T) dependence of ΔR_s and ρ_{Cu} from 5 to 100 K for device 4-3. With a decreasing T, ΔR_s initially increases because the phonon spin relaxation is suppressed. Below 30 K, however, ΔR_s decreases upon further cooling. This is caused by the Kondo spin relaxation originating from the Fe impurities in the Cu channel and has been addressed in previous works [13,14,18]. To obtain the individual ρ_{Cu} of a NLSV, the resistance R_{Cu} is measured by sending a current through the Cu channel and detecting the voltage between F_1 and F_2. Then ρ_{Cu}

is deduced from R_{cu} and the dimensions of the channel. For device 4-3, ρ_{Cu} = 2.52 μΩ·cm at 295 K and 0.31 μΩ·cm at 5 K yielding RRR = 8.1. The average RRR of all 14 devices is 6.4. In previous NLSV experiments, A_{cu} is usually < 0.2 × 0.2 μm^2, the RRR values for Cu channels are usually 2 to 3, and ρ_{Cu} at low T is typically 1 to 4 μΩ·cm [5,9-17]. Clearly the electrical conductivity is much enhanced in the current batch of devices.

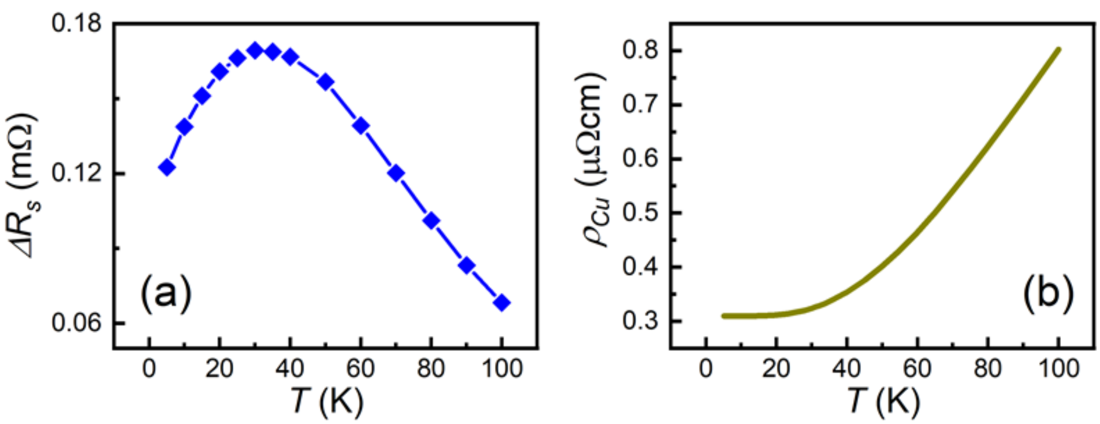

Figure 3.2: Temperature dependence of (a) ΔR_S and (b) ρ_{Cu} for device 4-3 (L = 3 μm).

3.3 Proper expressions of the spin signal

The general expression [21] of the nonlocal spin signal ΔR_s, adapted to our Cu based NLSVs, is:

$$\Delta R_s = 4R_{sCu}\frac{\left(P_{i1}\frac{R_{si1}}{R_{sCu}}+p_f\frac{R_{sF1}}{R_{sCu}}\right)\left(P_{i2}\frac{R_{si2}}{R_{sCu}}+p_f\frac{R_{sF2}}{R_{sCu}}\right)e^{-\frac{L}{\lambda_{Cu}}}}{\left(1+\frac{2R_{si1}}{R_{sCu}}+\frac{2R_{sF1}}{R_{sCu}}\right)\left(1+\frac{2R_{si2}}{R_{sCu}}+\frac{2R_{sF2}}{R_{sCu}}\right)-e^{-\frac{2L}{\lambda_{Cu}}}}, \tag{3.1}$$

where $R_{sCu} = \rho_{Cu}\lambda_{Cu}/A_{Cu}$, $R_{si} = R_i/(1 - P_i^2)$, and $R_{sF} = {}^{\rho_{Py}\lambda_{Py}}\!\Big/_{w_F w_{Cu}(1 - p_f^2)}$ are the spin resistance [22] of the Cu channel, the AlOx interfaces, and the ferromagnetic metal (Py) underneath the interface, respectively. Subscripts 1 or 2, such as in R_{si1} and R_{si2}, indicates relevance to either the spin injector F1 or the spin detector F2. λ_{Py} and ρ_{Py} are the spin diffusion length and resistivity of Py, respectively, and R_i is the electrical resistance of the AlOx interfaces. P_i is interfacial spin polarization of the AlOx junctions and p_f is the bulk spin polarization of Py. w_{Cu} and w_F are the widths of the Cu channels and Py stripes.

For tunnel barrier interfaces ($R_{si} \gg R_{sCu}$), Eq. (3.1) is reduced to a pure exponential decay form $\Delta R_s = P_{i1}P_{i2}R_{sCu}e^{-\frac{L}{\lambda_{Cu}}}$. It is also important to realize that this exponential form can be well preserved with even a modest R_{si}. Consider $R_{si} = 3R_{sCu}$. While the first term on the denominator of Eq. (3.1) exceeds 49, the second term $e^{-\frac{2L}{\lambda_{Cu}}}$ is 0.37 at $L = \lambda_{Cu}/2$ and 0.14 at $L = \lambda_{Cu}$. Therefore, neglecting the $e^{-\frac{2L}{\lambda_{Cu}}}$ term is well justified, and the resulting inaccuracy on ΔR_s is < 1% at $L = \lambda_{Cu}/2$ and decreases even further as L increases. By dropping this term and redefining variables

$$P_1 = \frac{2\left(P_{i1}\frac{R_{si1}}{R_{sCu}} + p_f\frac{R_{sF1}}{R_{sCu}}\right)}{\left(1 + \frac{2R_{si1}}{R_{sCu}} + \frac{2R_{sF1}}{R_{sCu}}\right)} \tag{3.2.1}$$

$$P_2 = \frac{2\left(P_{i2}\frac{R_{si2}}{R_{sCu}} + p_f\frac{R_{sF2}}{R_{sCu}}\right)}{\left(1 + \frac{2R_{si2}}{R_{sCu}} + \frac{2R_{sF2}}{R_{sCu}}\right)} \tag{3.2.2}$$

we can write Eq. (3.1) as

$$\Delta R_s = P_1P_2R_{sCu}e^{-L/\lambda_{Cu}} = \frac{P_1P_2\rho_{Cu}\lambda_{Cu}}{A_{Cu}}e^{-L/\lambda_{Cu}} \tag{3.3}$$

P_1 and P_2 can be understood as effective spin polarizations of F_1 and F_2. For F_1 and F_2 stripes with similar dimensions and identical materials and interfaces, it is common to assume $P_1 = P_2 = P_e$.

To justify the use of Eq. (3.3) in this work, we measured R_i values by using a four-probe method across the Py/AlO_x/Cu junctions formed between the Cu channel and the Py stripe (F_1 or F_2). The average R_{i1} is 2.3 Ω and R_{i2} is 2.6 Ω. Clearly these interfaces are low resistance barriers instead of tunnel junctions which would have kΩ resistance. The Cu spin resistance $R_{sCu} = 0.055$ Ω is estimated from $\rho_{Cu} = 0.43$ μΩ·cm and $\lambda_{Cu} = 3.2$ μm (both obtained in the next section). This R_{sCu} is much smaller than those in the literature because of the larger Cu cross section and the reduced ρ_{Cu} in this work. Obviously, $R_{si} > R_i \gg R_{sCu}$ and it is well justified to use Eq. (3.3) in the following analysis.

3.4 Extracting spin diffusion length and time

To extract the average spin diffusion length λ_{cu} at 30 K, the spin signal ΔR_s is plotted on a log scale versus the channel length L on a linear scale for all devices in Fig. 3.3 (a). The 14 data points spread evenly on the horizontal scale between 1 and 5 μm, and range between 0.18 and 0.04 mΩ on the vertical scale. Substantial scattering of the data points is present even for devices with the same L. At L = 3 μm, for example, ΔR_s values are between 0.17 and 0.10 mΩ. Clearly device quality varies despite the identical dimensions and fabrication conditions. We will exploit this to gain more insights into individual devices later in the text. The decaying feature of ΔR_s with an increasing L, as indicated by Eq. (3.3), is present but not dramatic. This suggests an average λ_{cu} that is clearly greater than 1 μm. To proceed with data fitting, the average ρ_{cu} for all devices is needed and we obtain ρ_{cu} = 0.43 ± 0.01 μΩ·cm by fitting $R_{Cu} = \rho_{Cu} L / A_{Cu}$ to the R_{Cu} versus L data in Fig. 3.3 (b). Subsequently, fitting Eq. (3.3) to the data in Fig. 3.3(a) yields an average spin diffusion length of $\lambda_{Cu} = 3.2 \pm 0.7$ μm as well as an average spin polarization of $P_e = 0.066 \pm 0.008$.

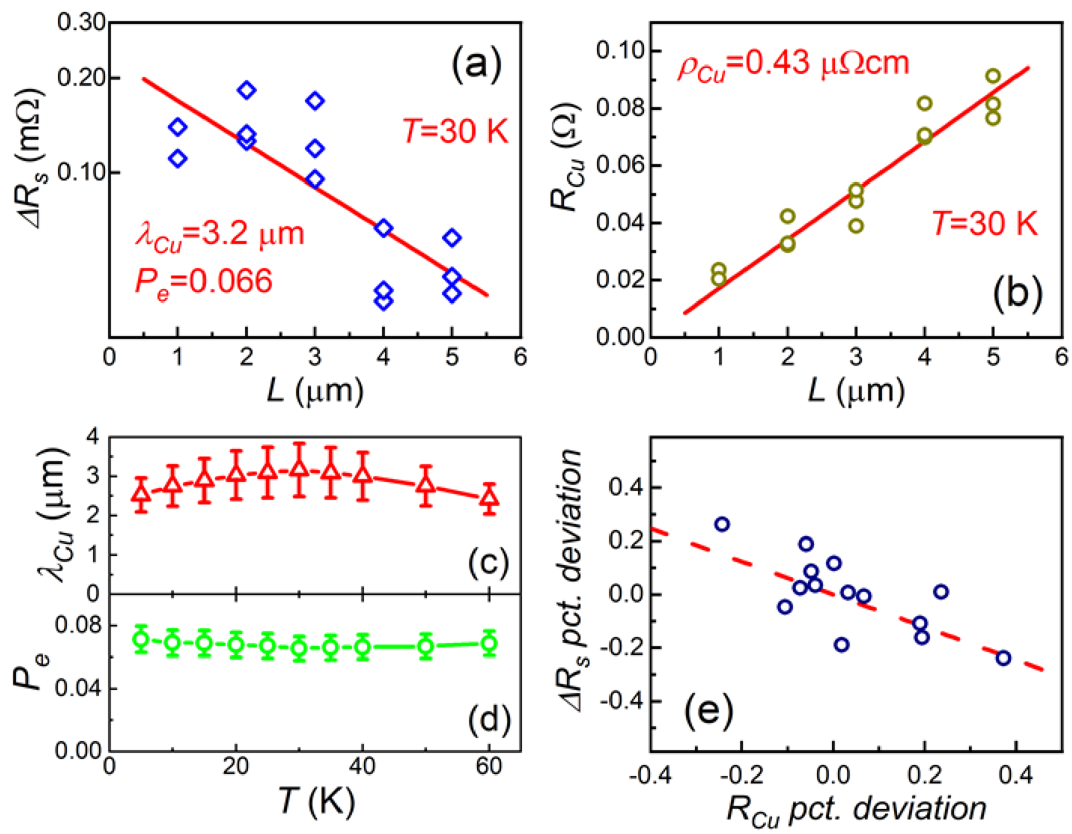

Figure 3.3: (a) A semi-log plot of spin signal ΔR_S versus channel length L at 30 K. (b) R_{Cu} versus L at 30 K. (c) Fitted λ_{Cu} and (d) fitted P_e versus T. (e) Percentage deviation of ΔR_S versus that of R_{Cu}. The solid lines in (a) and (b) are linear fits. The dashed line in (e) is a guide for the eye.

The fitted λ_{cu} clearly exceeds previously reported values [5,9-17] and is encouraging for a metallic channel with a submicron cross section. The fitted P_e value is identical to that obtained from NLSV devices which differ from the current batch only in the thickness of the Cu channels [18]. This gives confidence in the fitted values of λ_{cu} and P_e despite the scattering of data. Using this method, we obtain the average λ_{Cu} and P_e versus T from 5 to 60 K as plotted in Fig. 3.3 (c) and (d). $\lambda_{Cu}(T)$ resembles $\Delta R_s(T)$ in Fig. 3.2(a) and peaks at 30 K due to the interplay between the phonon and Kondo spin relaxations. λ_{cu} is 2.5 ± 0.4 μm at 5 K and 2.4 ± 0.4 μm at 60 K. $P_e(T)$ remains nearly a constant around 0.07 within the T range.

Now we examine the scattering of data points around the best fits in Figs 3.3 (a) and (b). The best fits represent the average quality of the 14 devices. Individual data points (devices) deviate from the best fit to various extent. Take the two devices at $L = 1$ μm as an example, ΔR_s are below the fit line while R_{Cu} are above the line suggesting that a smaller ΔR_s might be associated with a larger ρ_{Cu}. This trend is shown systematically in Fig. 3.3 (e), which is the percentage deviations of ΔR_s versus that of R_{Cu} for all devices. The percentage deviation is defined as the percentage difference between the actual value of ΔR_s or R_{Cu} for a device and the best fit value. A positive (negative) value means being larger (smaller) than average.

In Fig. 3.3 (e), the downward trend indicates that a larger (smaller) R_{Cu} or ρ_{Cu} leads to a smaller (larger) ΔR_s. This contradicts the apparent proportionality between ΔR_s and ρ_{Cu} in Eq. (3.3) assuming a constant λ_{Cu}. On the other hand, Elliot-Yafet model [23,24], indicates that λ_{Cu} is not a constant and $\lambda_{Cu} \propto 1/\rho_{Cu}$ assuming a fixed spin-flip probability. Therefore, a larger (smaller) ρ_{Cu} or R_{Cu} gives a smaller (larger) λ_{Cu} and thereby a smaller (larger) ΔR_s, fully explaining the trend in Fig. 3.3(e).

The above analysis justifies extracting an individual λ_{Cu} from a given NLSV device. The individual λ_{Cu} at a given T can be obtained from ΔR_s, the individual ρ_{Cu}, and the fitted P_e by using Eq. (3.3) with proper error propagation. Fig. 3.4 (a) shows the obtained individual λ_{Cu} values for device 4-3 (L= 3 μm) and 3-1 (L = 1 μm) as a function of T. At 30 K, λ_{Cu} = 5.3 ± 0.8 μm for device 4-3 and λ_{Cu} = 1.9 ± 0.3 μm for device 3-1. These are largest and smallest individual λ_{Cu} values among 14 devices.

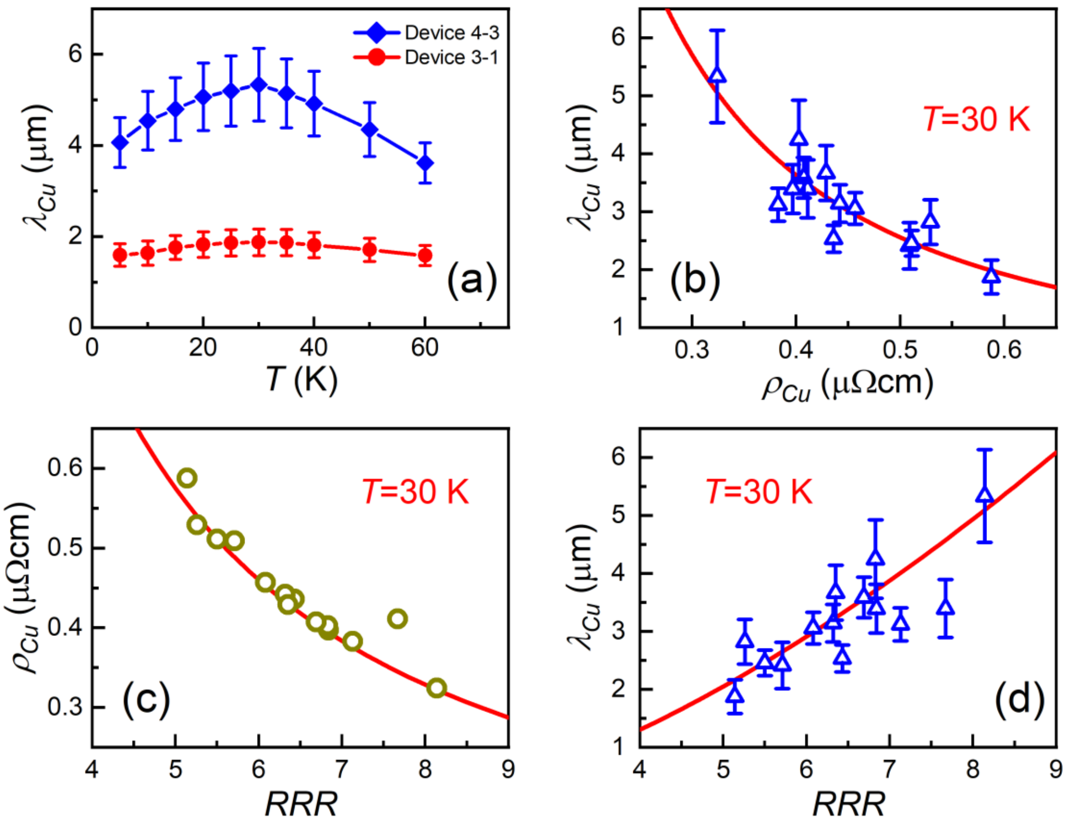

Figure 3.4: (a) λ_{Cu} versus T for device 3-1 (L = 1μm) and device 4-3 (L = 3μm). Plots of (b) λ_{Cu} versus ρ_{Cu}, (c) ρ_{Cu} versus RRR, and (d) λ_{Cu} versus RRR for all devices at 30 K. The solid lines are best fits in (b), (c), and (d).

The plot of λ_{Cu} versus ρ_{Cu} at 30 K for all devices are shown in Fig. 3.4 (b). While ρ_{Cu} varies by a factor of 2 from 0.3 to 0.6 μΩ·cm, λ_{Cu} decreases from 5.3 to 1.9 μm. This trend is qualitatively consistent with the Elliot-Yafet relation $\lambda_{Cu} \propto 1/\rho_{Cu}$

mentioned above. However, an attempted fit by using this relation does not describe the data well. The assumed fixed spin-flip probability is an oversimplification for Cu channels with numerous scattering mechanisms such as phonons, Kondo effects, surfaces, GB, and impurities. Instead, we use an empirical relation $\lambda_{Cu} \sim {\rho_{Cu}}^{-\gamma}$ to fit the data and the best fit gives γ = 1.6.

In addition to the correlation between λ_{Cu} and ρ_{Cu}, Fig. 3.4 (c) and (d) demonstrate clearly that both ρ_{Cu} and λ_{Cu} correlate well with the RRR. The relations can be described well by $\rho_{Cu} = \rho_{ph}/(RRR - 1)$ and $\lambda_{Cu} = A\left[(RRR - 1)/\rho_{ph}\right]^{\gamma}$, where ρ_{ph} is the phonon resistivity at 295 K. These expressions are straightforward to derive with a few well justified approximations. ρ_{Cu} varies little below 30 K, as is evident in Fig. 3.2(b), and is treated as T independent. Average ρ_{ph} of 2.3 ± 0.1 μΩ·cm is obtained by subtracting ρ_{Cu} at low T from that of 295 K and is treated as a constant. The correlation among λ_{Cu}, ρ_{Cu}, and RRR, as shown in Fig. 3.4 (b) through (d), further demonstrate the variations between devices and justify extracting individual λ_{Cu} values. In addition, RRR is established as an indicator for λ_{Cu} as shown in Fig. 3.4(d).

The spin relaxation time (τ_s) can be derived by using the relation $\tau_s = {\lambda_{Cu}}^2/D$, where $D = \frac{1}{3}{v_F}^2\tau_e$ is the diffusion constant. $v_F = 1.57 \times 10^6$ m/s is the Fermi velocity of Cu, and τ_e is the momentum relaxation time and is determined from the Drude model $\tau_e = m/(\rho_{Cu} n e^2)$, where $n = 8.47 \times 10^{28}$ m^{-3} is the electron density in Cu, m and e are the electron mass and charge, respectively. Fig. 3.5 shows the average τ_s and the optimal τ_s (device 4-3) as a function of T. At 30 K, the average τ_s reaches 120 ± 50 ps and the optimal τ_s is 270 ± 80 ps. The low temperature τ_s from previous studies is typically < 50 ps [12-17,25,26].

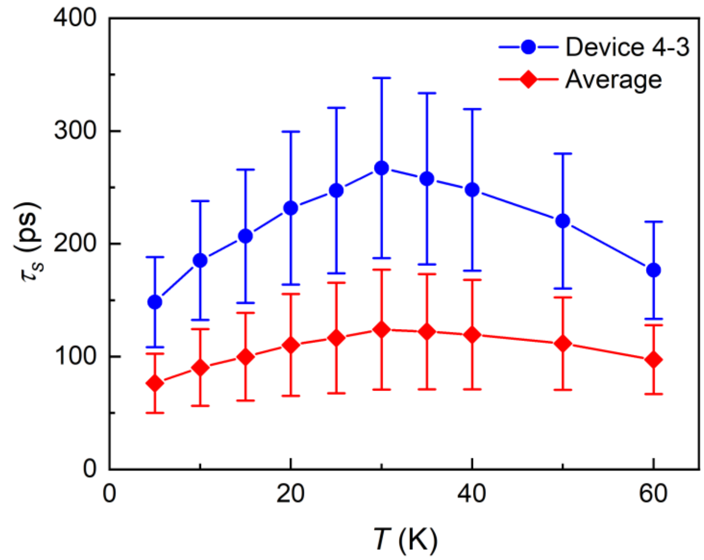

Figure 3.5: Plots of τ_S versus T for device 4-3 and the average τ_S versus T for all devices.

At this point, it is natural to inquire about the room temperature (RT) values of λ_{Cu} and τ_s. While RT spin signals have been detected from NLSVs with L = 1 μm, they are too weak to be clearly measured from devices with L ≥ 2 μm. Both P_e and λ_{Cu} are reduced at RT leading to the smaller spin signals. In addition, the spin signals are further reduced by the fact that the channel length L and cross section A_{Cu} are distinctly larger than those of most NLSVs in the literature. An accurate measurement of λ_{Cu} at RT requires multiple NLSVs with varying L values that are below 2 μm.

3.5 Further analysis

The much enhanced λ_{Cu} and τ_s are striking and can be attributed to the larger cross sections of the Cu channels, which accommodate larger grain sizes and have smaller surface-to-volume ratio. It is well documented that the resistivity of metal wire decreases as the cross-section of the wire increases. The size dependency primarily originates from electron scatterings at GB and surfaces, which are described by the classical Mayadas-Shatzkes (MS) [27] and Fuchs-Sondheimer (FS) models [28,29], respectively. The total resistivity of Cu channel can be separated into 3 components:

$$\rho_{Cu} = \rho_{bulk} + \rho_{GB} + \rho_{surf}, \tag{3.4}$$

where ρ_{bulk}, ρ_{GB}, and ρ_{surf} are the bulk, GB, and surface contributions, respectively. The bulk resistivity arises from scattering sources within a Cu grain such as impurities, phonons, and crystalline defects. ρ_{bulk} is commonly assumed to be dimension (thickness and width) independent [27,30,31].

The total resistivity from the bulk plus GB contributions is given by the MS model as [27]:

$$\rho_{bulk+GB} = \rho_{bulk}[1 - \tfrac{3}{2}\alpha + 3\alpha^2 - 3\alpha^3 \ln(1 + \alpha^{-1})]^{-1}, \tag{3.5}$$

here $\alpha = l_{bulk}R/G(1 - R)$. l_{bulk} is the bulk mean-free-path and will be determined in a moment. The product of ρ_{bulk} and l_{bulk} is a constant: $\rho_{bulk}l_{bulk} = mv_F/ne^2$, which can be trivially derived from the Drude model and the relation $l_{bulk} = v_F\tau_{e,bulk}$, with $\tau_{e,bulk}$ being the bulk momentum lifetime. R is the GB reflection coefficient. $R = 0$ means total transmission of the electrons at the grain boundaries and $R = 1$ means total reflection. For polycrystalline Cu, Mayadas et al. and Chawla et al. have both reported R to be around 0.25 [27,31]. G is the average grain size. For vacuum deposited Cu, the average grain size increases as the thickness d increases. The correlation between the two is commonly described by a power law [32]:

$$G = Ad^{\xi} \tag{3.6}$$

It has been found that the prefactor $A = 1.35$, and the growth exponent $\xi = 0.789$, (when G and d are in the units of nm) for evaporated polycrystalline Cu [32].

Transmission Electron Microscopy measurements of grain sizes in NLSV Cu channels agree reasonably well with the formula [17]. Based on these, we estimate the average grain size of our Cu channel (with *d* = 500 nm) to be 180 nm.

A theoretical description of the surface resistivity was developed by Fuchs and Sondheimer for thin films and was later expanded to wires with square cross-section by MacDonald and Sarginson [33]. Assuming completely diffuse scattering on the surfaces as verified by the study of Chawla *et al.* [31], the total Cu resistivity including all 3 components is given by [33]:

$$\rho_{Cu} = \rho_{bulk+GB+surf} = \rho_{bulk+GB}\left\{1 - \frac{3}{\pi}\left(\frac{\pi}{4k} - \frac{4}{15k^2}\right) + \frac{12}{\pi}\int_0^{\frac{\pi}{4}}\left(\frac{\pi}{4k}cos\theta - \frac{1}{3k}sin\theta - \frac{1}{3k^2}sin2\theta\right)e^{-k/cos\theta}sin^3\theta d\theta + \frac{12}{\pi}\int_{\frac{\pi}{4}}^{\frac{\pi}{2}}[\frac{cos\theta}{k}\left(\frac{\pi}{4} - \frac{1}{2}cos^{-1}(cot\theta)\right) + \frac{cot^2\theta}{2k}\sqrt{-cos2\theta} - \frac{1}{3k}\left(sin\theta - \frac{(-cos2\theta)^{\frac{3}{2}}}{sin^2\theta}\right) - \frac{2}{3k^2}(sin\theta cos\theta - \frac{cos\theta}{sin^2\theta}(-cos2\theta)^{\frac{3}{2}})]e^{-k/cos\theta}sin^3\theta d\theta\right\}^{-1}, \tag{3.7}$$

where $k = d/l_{bulk+GB}$. $l_{bulk+GB}$ is the mean-free-path considering both the bulk and the GB scatterings and can be estimated by $l_{bulk+GB} = l_{bulk}\rho_{bulk}/\rho_{bulk+GB}$ [27]. To determine the contribution of each scattering source to the total resistivity of our Cu channels, we solve for the only unknown parameter l_{bulk} by using the chip average resistivity of 0.43 μΩcm at 30 K and Eq. (3.7), and we find $l_{bulk} = 450$ nm. Our value is in reasonable agreement with the 300 nm bulk mean-free-path under 20 K reported by Plombon *et al.* [30]. Subsequently, we obtain ρ_{bulk} = 0.15 μΩ·cm, ρ_{GB} = 0.17 μΩ·cm and ρ_{surf} = 0.11 μΩ·cm directly from their analytical expressions based on the MS and FS models. The three components ρ_{bulk}, ρ_{GB}, and ρ_{surf} are quite comparable.

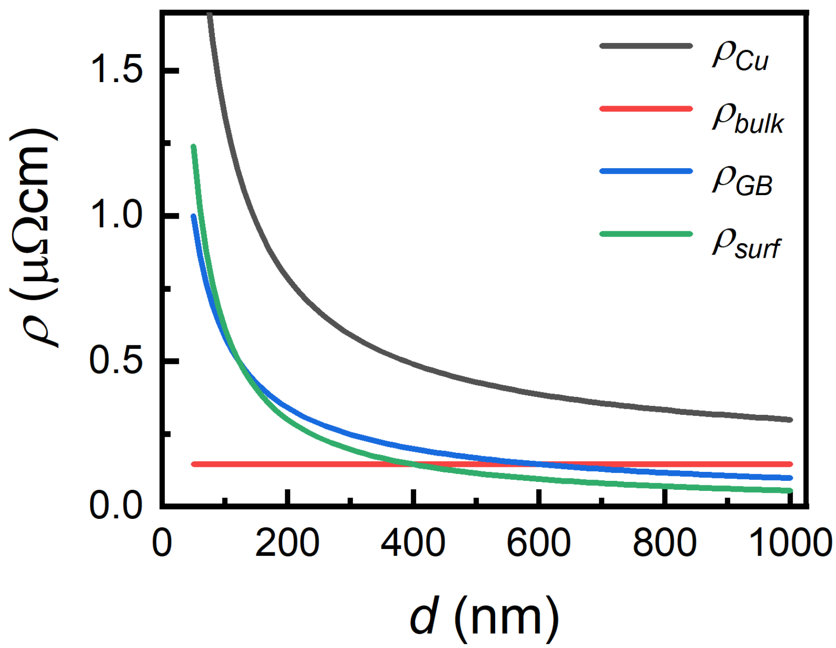

Figure 3.6: Calculated total, bulk, grain boundary, and surface resistivities as functions of the Cu channel dimension *d*.

To illustrate the influence of the dimensions, the dependences of ρ_{Cu}, ρ_{bulk}, ρ_{GB}, and ρ_{surf} on *d* are shown in Fig. 3.6, assuming a constant ρ_{bulk} = 0.15 µΩ·cm. In the range of 100 nm < *d* < 200 nm, which is typical for NLSVs in the literature, both ρ_{GB}, and ρ_{surf} rapidly increase with a decreasing *d*. The drastically enhanced GB and surface scattering limits λ_{Cu} in devices with smaller cross sections.

In our previous works [19,34], it has been demonstrated that a larger cross section (with either a larger thickness or a larger width) of the Cu channels generally leads to a longer λ_{Cu}. Table 3.1 provides a comparison of 3 sets of NLSV devices that have square (or approximately square) cross sections with different sizes. Set A and B are chosen from our previously published works [15,34] and C is the current set of NLSVs in this work. The low temperature values of λ_{Cu} are 0.58 µm, 0.96 µm, and

3.2 μm for cross sectional sizes of ~ 0.1μm, ~ 0.2 μm, and 0.5 μm, respectively. This clearly illustrates the effective enhancement of λ_{Cu} by increasing the size of the cross sections.

Table 3.1: A comparison of 3 sets of NLSVs with different dimensions of Cu channels. Set A consists of NLSVs used in Ref. 15 [15]. Set B includes NLSVs on Substrate No. 70-4 in Ref. 34 [34]. Set C includes NLSVs described in this work.

Device set	# of devices	Cu width (μm)	Cu thickness (μm)	T (K)	avg ρ_{Cu} (μΩ·cm)	avg λ_{Cu} (μm)
A	32	0.125	0.11	10	3.3 ± 0.2	0.58 ± 0.03
B	16	0.18	0.2	10	2.0 ± 0.3	0.96 ± 0.14
C	14	0.5	0.5	30	0.43 ± 0.01	3.2 ± 0.7

3.6 Conclusions

In conclusion, we demonstrate spin diffusion lengths of multiple micrometers at low temperatures in the Cu channels of nonlocal spin valves. Made with a cross section of 0.5 × 0.5 μm^2, the Cu channels exhibit high conductivity at low temperatures. At 30 K, an average spin diffusion length of $\lambda_{Cu} = 3.2 \pm 0.7$ μm and an average spin relaxation time $\tau_s = 120 \pm 50$ ps are determined from a set of devices fabricated in a single batch. Individual λ_{Cu} values vary considerably among the devices but correlate well with individual ρ_{Cu} and RRR values. From the most conductive device, $\lambda_{Cu} = 5.3 \pm 0.8\, \mu m$ and $\tau_s = 270 \pm 80\, ps$ are obtained. The enhanced λ_{Cu} values exceed previous expectations for metals and can be attributed to reduced grain boundary and surface scattering owing to the larger channel cross sections. These Cu channels may serve as effective conduits for spin current in spintronic circuits.

REFERENCES

[1] S. Datta and B. Das, Applied Physics Letters **56**, 665 (1990).

[2] M. Yamada, D. Sato, N. Yoshida, M. Sato, K. Meguro, and S. Ogawa, IEEE Transactions on Magnetics **49**, 713 (2013).

[3] B. Behin-Aein, D. Datta, S. Salahuddin, and S. Datta, Nature Nanotechnology **5**, 266 (2010).

[4] M. Johnson and R. H. Silsbee, Physical Review Letters **55**, 1790 (1985).

[5] F. J. Jedema, A. T. Filip, and B. J. van Wees, Nature **410**, 345 (2001).

[6] F. J. Jedema, H. B. Heersche, A. T. Filip, J. J. A. Baselmans, and B. J. van Wees, Nature **416**, 713 (2002).

[7] S. S. P. Parkin, R. Bhadra, and K. P. Roche, Physical Review Letters **66**, 2152 (1991).

[8] F. J. Albert, N. C. Emley, E. B. Myers, D. C. Ralph, and R. A. Buhrman, Physical Review Letters **89**, 226802 (2002).

[9] T. Kimura, T. Sato, and Y. Otani, Physical Review Letters **100**, 066602 (2008).

[10] H. Zou and Y. Ji, Applied Physics Letters **101**, 082401 (2012).

[11] M. Erekhinsky, F. Casanova, I. K. Schuller, and A. Sharoni, Applied Physics Letters **100**, 212401 (2012).

[12] E. Villamor, M. Isasa, L. E. Hueso, and F. Casanova, Physical Review B **87**, 094417 (2013).

[13] L. O'Brien, M. J. Erickson, D. Spivak, H. Ambaye, R. J. Goyette, V. Lauter, P. A. Crowell, and C. Leighton, Nature Communications **5**, 3927 (2014).

[14] J. T. Batley, M. C. Rosamond, M. Ali, E. H. Linfield, G. Burnell, and B. J. Hickey, Physical Review B **92**, 220420 (2015).

[15] Y. Cai, Y. Luo, C. Zhou, C. Qin, S. Chen, Y. Wu, and Y. Ji, Journal of Physics D: Applied Physics **49**, 185003 (2016).

[16] C. Zhou, F. Kandaz, Y. Cai, C. Qin, M. Jia, Z. Yuan, Y. Wu, and Y. Ji, Physical Review B **96**, 094413 (2017).

[17] J. D. Watts, L. O'Brien, J. S. Jeong, K. A. Mkhoyan, P. A. Crowell, and C. Leighton, Physical Review Materials **3**, 124409 (2019).

[18] X. Shen and Y. Ji, Physical Review B **104**, 085101 (2021).

[19] Y. Ji, X. Y. Shen, F. Kandaz, Y. J. Cai, C. Zhou, Y. Z. Wu, and Z. Yuan, Journal of Magnetism and Magnetic Materials **563**, 169845, 169845 (2022).

[20] X. J. Wang, H. Zou, L. E. Ocola, and Y. Ji, Applied Physics Letters **95**, 022519 (2009).

[21] S. Takahashi and S. Maekawa, Physical Review B **67**, 052409 (2003).

[22] T. Wakamura, K. Ohnishi, Y. Niimi, and Y. Otani, Applied Physics Express **4**, 063002 (2011).

[23] R. J. Elliott, Physical Review **96**, 266 (1954).

[24] Y. Yafet, Physics Letters A **98**, 287 (1983).

[25] A. J. Wright, M. J. Erickson, D. Bromley, P. A. Crowell, C. Leighton, and L. O'Brien, Physical Review B **104**, 014423 (2021).

[26] X. Y. Shen, Y. J. Cai, Y. Z. Wu, and Y. Ji, Physical Review B **106**, 085118 (2022).

[27] A. F. Mayadas and M. Shatzkes, Physical Review B **1**, 1382 (1970).

[28] K. Fuchs, Mathematical Proceedings of the Cambridge Philosophical Society **34**, 100 (1938).

[29] E. H. Sondheimer, Advances in Physics **1**, 1 (1952).

[30] J. J. Plombon, E. Andideh, V. M. Dubin, and J. Maiz, Applied Physics Letters **89**, 113124 (2006).

[31] J. S. Chawla, F. Gstrein, K. P. O'Brien, J. S. Clarke, and D. Gall, Physical Review B **84**, 235423 (2011).

[32] A. Dulmaa, F. G. Cougnon, R. Dedoncker, and D. Depla, Acta Materialia **212**, 116896 (2021).

[33] D. K. C. Macdonald, K. Sarginson, and F. E. Simon, Proceedings of the Royal Society of London. Series A. Mathematical and Physical Sciences **203**, 223 (1950).

[34] Y. J. Cai, C. Qin, F. Kandaz, X. Y. Shen, C. Zhou, M. W. Jia, Y. M. Luo, Y. Z. Wu, and Y. Ji, Physical Review B **100**, 144419 (2019).

Chapter 4

SCALING OF KONDO SPIN RELAXATION: EXPERIMENTS ON CU-BASED NONLOCAL SPIN VALVES WITH FE IMPURITIES

4.1 Introduction

The Kondo effect [1,2] has captured attention for decades because of its complex many-body physics. In metals with dilute magnetic impurities, the signature of the Kondo effect is the low temperature increase of resistivity resulting from the antiferromagnetic s-d exchange interaction between the impurity spin and the conduction electron spins of the host metal. A popular but controversial physical picture is the Kondo screening cloud, which is an electron cloud surrounding the impurity site with an overall spin polarization opposite to the impurity spin. At temperatures well below the Kondo temperature T_K, the net spin of the Kondo cloud completely screens the impurity spin forming a Kondo singlet state. Its spatial extent ξ_K is given theoretically by $\hbar v_F/k_B T_K$ in the ballistic transport regime and $\sqrt{\hbar D/k_B T_K}$ in the diffusive regime [3,4], where v_F is the Fermi velocity, k_B is the Boltzmann constant, and D is the diffusion constant.

Consider Fe impurities in Cu host (T_K = 30 K) as an example. The ξ_K is 400 nm in the ballistic regime and ~ 100 nm in the diffusive regime. The average distance between Fe impurities at 1 part per million (ppm) in Cu is ~ 20 nm and significantly smaller than ξ_K. This leads to a somewhat unsettling implication that Kondo clouds from neighboring impurities overlap substantially even at a very low concentration [5]. The size and configuration of Kondo clouds are challenging to probe experimentally, because the spin density is extremely dilute: ~ 1 Bohr magneton per (100 nm)^3 volume. The physical existence of Kondo clouds has been questioned [3,6,7]. Recently Borzenets *et al*. [8] found convincing evidence for micrometer-sized Kondo clouds in a semiconductor quantum dot [9] system. However, evidence for Kondo clouds in metals is still lacking.

In recent years, the Kondo effect has crossed paths with spintronics. In the Cu channels of nonlocal spin valves (NSLVs) [10,11] with dilute Fe impurities, the spin relaxation rate ${\tau_s}^{-1}$ is found to increase at low temperatures, complementing the Kondo effect's low temperature increase of the momentum relaxation rate ${\tau_e}^{-1}$ [12-15]. Here τ_s and τ_e are the spin relaxation time and momentum relaxation time, respectively. For spin relaxation in general, Elliott-Yafet (EY) [16,17] and Dyakonov-Perel (DP) [18] models give explicit relations between ${\tau_s}^{-1}$ and ${\tau_e}^{-1}$. The EY spin relaxation is caused by weak spin-orbit coupling between energy bands and ${\tau_s}^{-1}$ is proportional to ${\tau_e}^{-1}$. The ratio τ_e/τ_s is the spin relaxation probability α. The DP spin relaxation originates from spin-orbit coupling, caused by inversion symmetry breaking, between two spin sub-bands within the same energy band and ${\tau_s}^{-1}$ is inversely proportional to ${\tau_e}^{-1}$. The Kondo spin relaxation, however, is caused by s-d exchange interaction instead of spin-orbit effects.

In this work, we use a systematic method to extract the Kondo spin relaxation rate ${\tau_{sK}}^{-1}$ and Kondo momentum relaxation rate ${\tau_{eK}}^{-1}$ from each NLSV device. A relation between ${\tau_{sK}}^{-1}$ and ${\tau_{eK}}^{-1}$ is established by using a set of 20 NLSVs. The ${\tau_{sK}}^{-1}$ is independent of ${\tau_{eK}}^{-1}$ as the latter varies over a substantial range. We provide a qualitative explanation of this unusual relation by considering the spin density and charge density of overlapping Kondo clouds as well as the spin and momentum relaxation processes through the clouds.

4.2 Sample preparation and measurements

Our NLSVs are fabricated by 2-step electron beam lithography. Each NLSV includes a spin injector F_1, a spin detector F_2, and a Cu channel, as shown in Figure 4.1 (a). Magnetic electrodes F_1 and F_2, made of $Ni_{81}Fe_{19}$ alloy (permalloy or Py), are patterned in the first step and Cu channels are patterned in the second step. The materials are deposited by electron beam evaporation. The widths of F_1 and F_2 are 160 nm and 120 nm, respectively, and the thickness is 35 nm. Before the deposition of Cu, low energy ion milling is performed to clean the surface of Py and a 3 nm AlO_x layer is deposited. The Py/AlO_x/Cu interfaces have been shown to provide a higher effective spin polarization than the ohmic Py/Cu interfaces [19,20]. The distance L between F_1 and F_2 varies from 1 to 5 μm with 1 μm increment. All Cu channels are 500 nm wide and 300 nm thick to prevent the suppression of Kondo clouds [7,21]. This work involves data from two sample substrates (chip 11 and chip 12) with 10 devices on each. Devices on the same substrate undergo identical fabrication conditions.

The measurement configuration is shown in Figure 4.1 (a). A low frequency alternating current (AC) I_e is driven from F_1 to the upper end of the Cu channel, and the nonlocal voltage V_{nl} is detected between F_2 and the lower end of the channel. The root-mean-square value of the AC current is consistently 0.3 mA in all nonlocal measurements. Figure 4.1 (b) shows the nonlocal resistance $R_s = V_{nl}/I_e$ as a function of magnetic field B applied parallel to F_1 and F_2 stripes. The high and low states of R_s correspond to the parallel and antiparallel states of F_1 and F_2 magnetizations, respectively. The difference is the spin signal [22]:

$$\Delta R_s = \frac{P_e^2 \rho_{cu} \lambda_{cu}}{A_{cu}} e^{-\frac{L}{\lambda_{cu}}} \tag{4.1}$$

where P_e is the effective spin polarization of F_1 and F_2, ρ_{cu} the Cu resistivity, λ_{cu} the Cu spin diffusion length, and A_{cu} the Cu channel cross sectional area. $\Delta R_s(T)$ of each NLSV is measured from 5 K to 100 K and Figure 4.1 (c) shows the data of device 11-43 (device 43 on chip 11). As T decreases, ΔR_s initially increases, reaching its maximum at 30 K, and then decreases. This feature is well documented [23-26] for NLSVs and convincingly attributed to the Kondo effect [12-15,27,28].

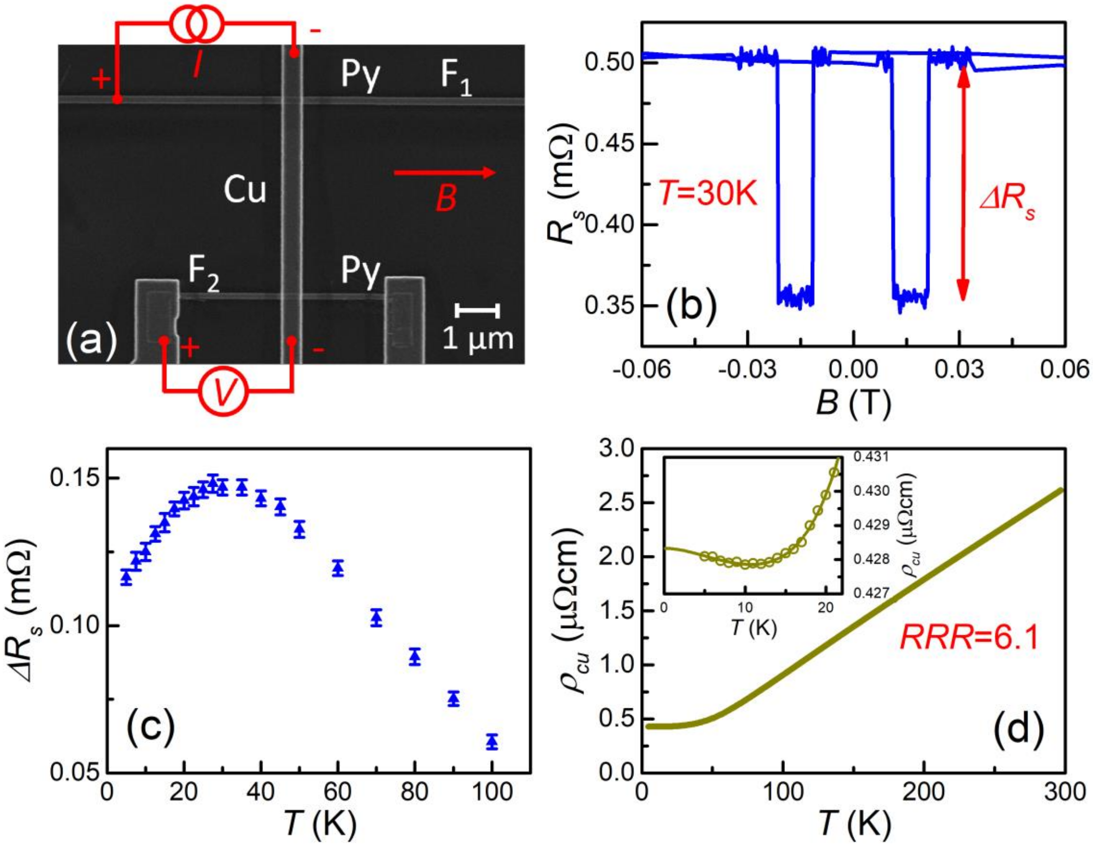

Figure 4.1: (a) SEM image of a NLSV. Plots of (b) R_s versus B, (c) ΔR_s versus T, and (d) ρ_{cu} versus T for device 11-43 (L = 3.0 µm).

The resistivity ρ_{cu} of a given NLSV is deduced from its Cu channel resistance R_{cu}, which is obtained by sending in an AC current of 0.1 mA through the channel and measuring the voltage difference between F_1 and F_2. The $\rho_{cu}(T)$ for device 11-43 is shown in Figure 4.1 (d) with $\rho_{cu} = 0.43$ μΩ·cm at 5 K and $\rho_{cu} = 2.60$ μΩ·cm at 295K. The ratio of the two values (6.1) is the residual resistivity ratio (RRR). The inset of Figure 4.1 (d) shows the low temperature portion of $\rho_{cu}(T)$. The low T increase of ρ_{cu} indicates the Kondo effect from dilute magnetic impurities in Cu.

The coexistence of the resistivity upturn and the spin signal downturn at low temperatures unequivocally points to the Kondo effect. The former is a telltale sign of Kondo physics [2] and the magnitude of the upturn is proportional to the impurity concentration [28]. The latter was initially interpreted as being related to high surface spin relaxation probabilities [23], but later works show strong evidence of Kondo effect [12-14,27]. The Cu resistivity changes little below 30 K, and so should the surface scattering probability for electrons. Therefore, the substantial decrease of spin signal below 30 K cannot be accounted for by a high surface spin relaxation probability. In addition, as we show later in the text, both the $\rho_{cu}(T)$ and ${\tau_s}^{-1}(T)$ data can be fitted well by the well-established Kondo physics formulas.

Previous work on NLSVs reported different spin signals measured on the opposite ends of the F_2 stripe [29]. However, such difference is not present in our NLSV devices. The average λ_{cu} (> 2 μm as shown in the next section) is significantly greater than the width (500 nm) of the Cu channel. Variation of spin accumulation across the channel width is negligible as can be seen from Figure 4.2 where we show the spin signal measurements of a device with L = 5 μm at 5 K (device 12-45). The cross configuration is for F_1 and F_2 on opposite sides of the Cu channel while the half configuration is for F_1 and F_2 on the same side of the channel. Obviously, the two configurations give identical spin signals.

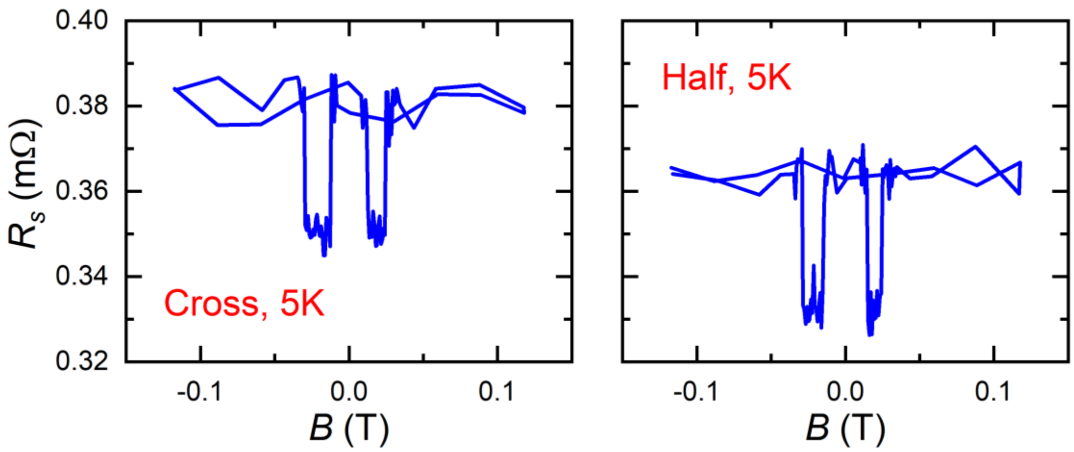

Figure 4.2: Comparison of spin signals of device 12-45 under cross and half configurations at 5 K.

4.3 Data analysis

Next, we extract the average P_e and λ_{cu} values of devices on the same substrate. ΔR_s versus L is plotted for 10 devices on chip 11 at 30 K in Figure 4.3 (a). Fitting Eq. (4.1) to the plot yields λ_{cu} = 2.6 ± 0.1 μm and P_e = 0.066 ± 0.003. The average ρ_{cu} used in this process is deduced from the linear fitting to the R_{cu} versus L data in Figure 4.3 (b). In this manner, the average P_e and λ_{cu} are obtained between 5 K and 100 K and shown in Figure 4.3 (c) and its inset, respectively. $\lambda_{cu}(T)$ resembles $\Delta R_s(T)$ in Figure 4.1(c) and reaches its maximum of 2.6 μm at 30 K. λ_{cu} decreases to 2.2 μm at 5 K because of the enhanced Kondo spin relaxation. The plot of $P_e(T)$ shows a rather flat trend around 0.07 within the temperature range of our measurements. For NLSVs on chip 12, we obtain λ_{cu} = 2.1 ± 0.2 μm and P_e = 0.064 ± 0.006 at 30 K. The trends of $\lambda_{cu}(T)$ and $P_e(T)$ are similar to those of chip 11.

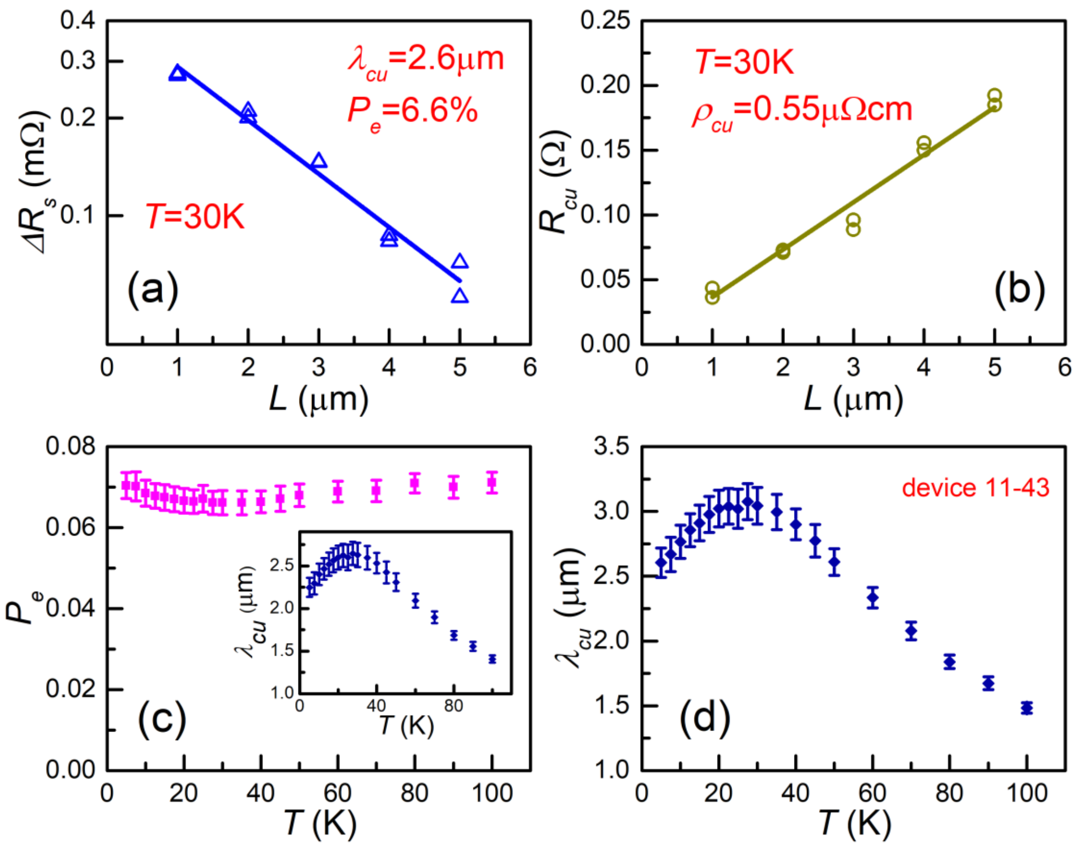

Figure 4.3: (a) Spin signal ΔR_s and (b) Cu resistance R_{cu} versus channel length L for NLSVs on chip 11 at 30 K. (c) Fitted average P_e and λ_{cu} (inset) as a function of T. (d) λ_{cu} versus T for device 11-43. The solid lines are fitting lines.

As suggested by previous works on Py/Cu NLSVs, the Kondo effect originates from Fe impurities [12-14,27,28]. The maximum λ_{cu} occurs at 30 K, which is the Kondo temperature T_K for Fe impurities in Cu host. Data analysis of ${\tau_s}^{-1}(T)$ and

${\tau_e}^{-1}(T)$ later in the text is also consistent with T_K = 30 K. The Fe impurities are likely introduced in the fabrication processes. When the Py surface is ion milled, Fe atoms are removed and deposited on the side walls of the resist. When Cu is evaporated, the vapor flux of Cu transfers momentum to the Fe atoms on the side walls and redeposits them into the Cu channel. In some of the previous works [12,15,27,28], Fe impurities are concentrated near the ohmic Py/Cu interfaces, and as a result the spin polarization $P_e(T)$ is suppressed at low T. In our devices, the Fe impurities are located throughout the Cu channel. This is evident from the low T upturn of $\rho_{cu}(T)$, the low T downturn of $\lambda_{cu}(T)$, and the flat trend of $P_e(T)$.

It is noticeable that data points disperse around the fitted lines in Figure 4.3 (a) and (b). For the two devices with L = 3 μm, for example, data points of ΔR_s are above the fitted line and those of R_{cu} are below. These indicate variations of P_e, λ_{cu}, and ρ_{cu} between devices. Here we explore a method to extract the λ_{cu} value from each NLSV. For a given NLSV on chip 11, the ρ_{cu} is obtained directly from its Cu resistance. The fitted P_e values and uncertainties shown in Figure 4.3 (c) provide the range of P_e for devices on chip 11 at various temperatures. The λ_{cu} of the NLSV at a specific T is then calculated from ΔR_s, P_e, and ρ_{cu} by using Eq. (4.1), and the uncertainty of λ_{cu} is properly propagated from the uncertainty of P_e and the measurement uncertainty of ΔR_s. $\lambda_{cu}(T)$ for device 11-43 is shown in Figure 4.3 (d) with a maximum $\lambda_{cu} = 3.0 \pm 0.1$ μm at 30 K. In this manner $\lambda_{cu}(T)$ are obtained for all 20 NLSVs.

In Figure 4.4, λ_{cu} versus ρ_{cu} at 30 K is plotted for all 20 NLSVs on chips 11 and 12. As ρ_{cu} increases from 0.44 to 1.0 μΩ·cm, λ_{cu} clearly decreases from 3.0 μm to < 2.0 μm. This trend is qualitatively consistent with the Elliott-Yafet model. Since several spin relaxation mechanisms with different spin relaxation probabilities are involved, the decrease of λ_{cu} is slower than a $1/\rho_{cu}$ dependence, which would be the case for a fixed spin relaxation probability.

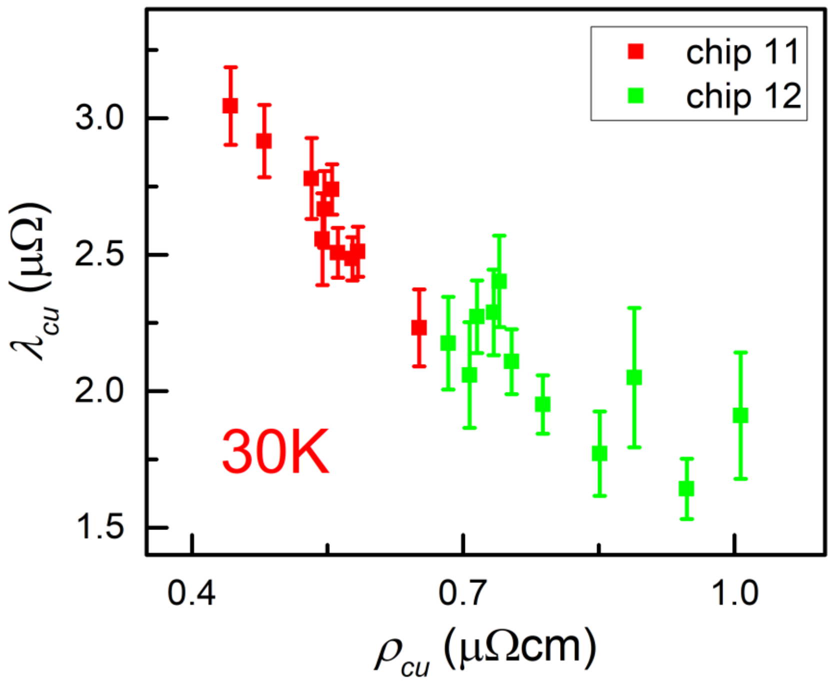

Figure 4.4: The spin diffusion length versus resistivity for NLSVs on chips 11 and 12.

The spin relaxation rate $\tau_s{}^{-1}(T)$ is calculated from $\lambda_{cu}(T)$ by using the relation $\lambda_{cu} = \sqrt{D\tau_s}$ and shown in Figure 4.5 (a) and (b) for devices 11-33 and 12-32, respectively. $D = \frac{1}{3}v_F{}^2\tau_e$ is the diffusion constant and $v_F = 1.57 \times 10^6$ m/s is the Fermi velocity of Cu. τ_e can be derived from ρ_{cu} by using the Drude model $\rho_{cu} = m/(\tau_e ne^2)$, where $n = 8.47 \times 10^{28}$ m^{-3} is the Cu electron density and m and e are electron mass and charge, respectively. With a decreasing T, $\tau_s{}^{-1}$ initially decreases,

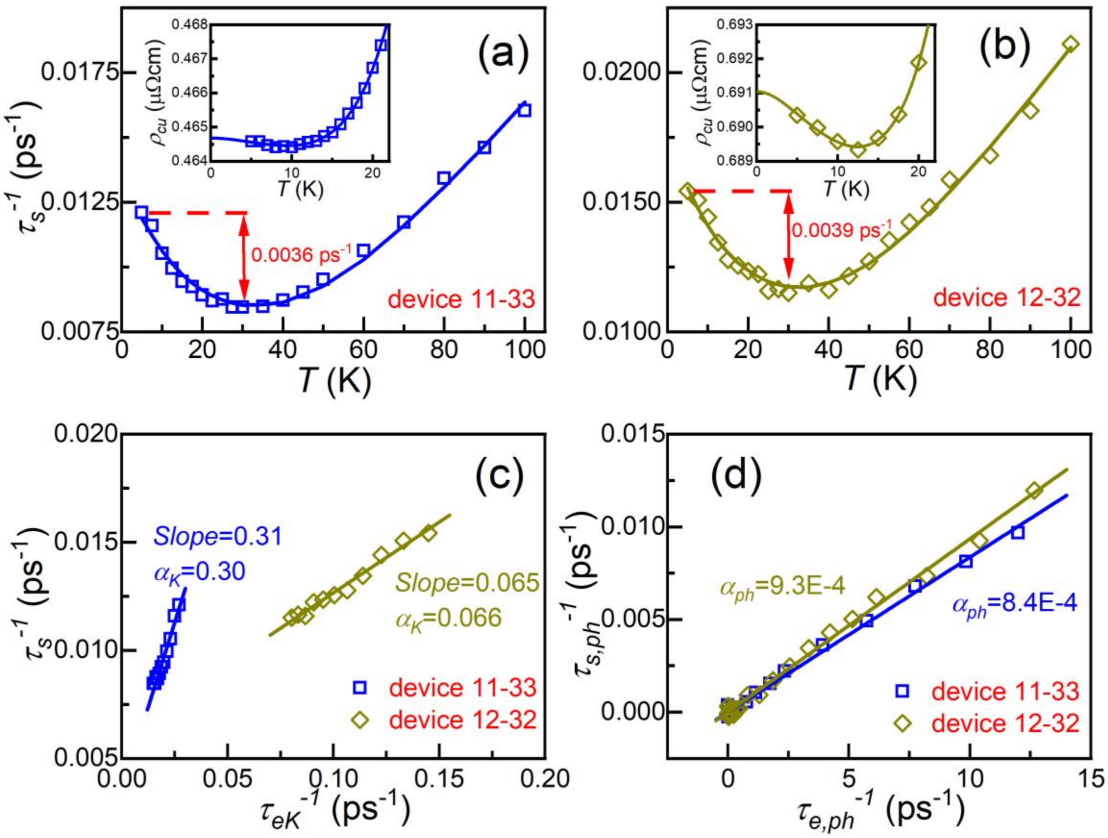

Figure 4.5: Spin relaxation rate τ_S^{-1} versus T for (a) device 11-33 and (b) device 12-32. $\rho_{cu}(T)$ plots are shown in the insets. (c) τ_S^{-1} versus τ_{eK}^{-1} for $T \leq 30$ K for the two devices. The slopes of the linear fittings are compared with α_K values obtained from fittings with Eq. (4.2). (d) $\tau_{S,ph}^{-1}$ versus $\tau_{e,ph}^{-1}$ plots. The solid lines are fitting lines.

reaches its minimum around 30 K, and then increases upon further cooling. This resembles the Kondo effect's low temperature increase of ρ_{cu} as shown in the insets of Figure 4.5 (a) and (b). The low T increase of ρ_{cu} of 11-33 is much smaller than that of 12-32, indicating a lower impurity concentration in 11-33 [28]. However, the low T increase of τ_s^{-1} of the two devices are surprisingly comparable. This provides the first hint for an unusual relation between Kondo momentum relaxation and Kondo spin relaxation.

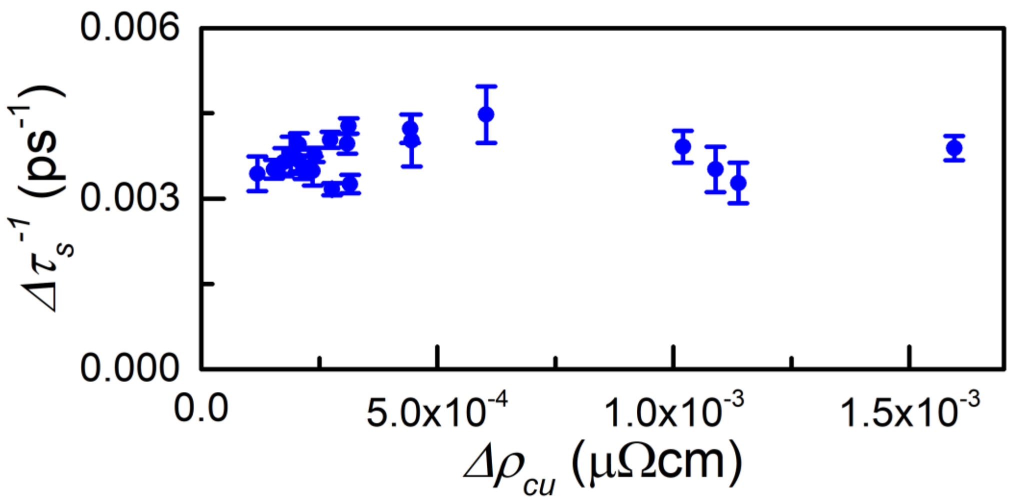

Figure 4.6: The low temperature increase of Cu spin relaxation rate $\Delta\tau_S^{-1}$ versus the low temperature increase of Cu resistivity $\Delta\rho_{cu}$.

To establish an overall trend, the low T upturn of τ_s^{-1} is plotted versus that of ρ_{cu} for all 20 NLSVs in Figure 4.6. Strikingly, while $\Delta\rho_{cu}$ varies by more than an order of magnitude between 1.2×10^{-4} μΩ·cm and 1.6×10^{-3} μΩ·cm, $\Delta\tau_s^{-1}$ is confined between 0.003 and 0.0045 ps^{-1} with no apparent dependence on $\Delta\rho_{cu}$. While $\Delta\rho_{cu}$ scales with the additional momentum relaxation rate from the Kondo effect, $\Delta\tau_s^{-1}$ scales with the additional spin relaxation rate from the Kondo effect. Note that $\Delta\rho_{cu}$ and $\Delta\tau_s^{-1}$ are extracted directly from $\rho_{cu}(T)$ and $\tau_s^{-1}(T)$ curves without any fitting. $\rho_{cu}(T)$ is measured by lock-in method with long-time averaging and the uncertainty is $< 5 \times 10^{-5}$ μΩ·cm. The uncertainty of $\tau_s^{-1}(T)$ mainly comes from the uncertainty of

$P_e(T)$. We will show later that the uncertainty of $P_e(T)$ moves the entire ${\tau_s}^{-1}(T)$ curve up or down but induces only small uncertainties in $\Delta{\tau_s}^{-1}$. While it is an intuitive assumption that ${\tau_{sK}}^{-1}$ is proportional to ${\tau_{eK}}^{-1}$, Figure 4.6 clearly demonstrates a different and unusual scaling.

In the following, we show that the $\rho_{cu}(T)$ and ${\tau_s}^{-1}(T)$ data can be fitted by well-established models and the quantities of ${\tau_{eK}}^{-1}$ and ${\tau_{sK}}^{-1}$ can be extracted. Applying Matthiessen's rule to spin relaxation, the total ${\tau_s}^{-1}$ is given by ${\tau_s}^{-1} = {\tau_{s,def}}^{-1} + {\tau_{s,ph}}^{-1} + {\tau_{sK}}^{-1}$, where ${\tau_{s,def}}^{-1}$, ${\tau_{s,ph}}^{-1}$, and ${\tau_{sK}}^{-1}$ are the spin relaxation rates attributed to defects, phonon, and Kondo effect, respectively. Defining ${\tau_{e,def}}^{-1}$, ${\tau_{e,ph}}^{-1}$, and ${\tau_{eK}}^{-1}$ as the corresponding momentum relaxation rates and α_{def}, α_{ph}, and α_K as the associated spin relaxation probabilities, we have

$$\frac{1}{\tau_s(T)} = \alpha_{def}\frac{1}{\tau_{e,def}} + \alpha_{ph}\frac{1}{\tau_{e,ph}(T)} + \alpha_K\frac{1}{\tau_{eK}(T)} \tag{4.2}$$

It is well justified to assume a linear relation between ${\tau_s}^{-1}$ and ${\tau_e}^{-1}$ for defects and phonons, because EY mechanism is dominant. We will show later that ${\tau_{sK}}^{-1}$ is also proportional to ${\tau_{eK}}^{-1}$ under varying T.

The ${\tau_e}^{-1}$ of each type (total, defect, phonon, or Kondo) is linked to the corresponding ρ by the Drude model . The defect resistivity ρ_{def} is T independent and the phonon resistivity can be described as $\rho_{ph}(T) = AT^5$ at low T, where A is a constant related to the Debye temperature [30]. The Kondo resistivity can be described by a phenomenological formula [9]:

$$\rho_K(T) = \rho_{K0}\left(\frac{{T_K'}^2}{T^2+{T_K'}^2}\right)^s, \tag{4.3}$$

where $T_K' = T_K/\sqrt{2^{1/s}-1}$, s = 0.225 and T_K = 30 K. From ${\tau_e}^{-1} = {\tau_{e,def}}^{-1} + {\tau_{e,ph}}^{-1} + {\tau_{eK}}^{-1}$, the total resistivity is

$$\rho_{cu}(T) = \rho_{def} + AT^5 + \rho_K(T) \tag{4.4}$$

Fitting Eq. (4.4) along with Eq. (4.3) to the measured $\rho_{cu}(T)$ data below 20 K yields ρ_{def}, A, and ρ_{K0}. The fitting does not work well for T > 20 K, because $\rho_{ph}(T) = AT^5$ is only valid at low T. For the data of 11-33 and 12-32 in the insets of Figure 4.5 (a) and (b), the fitted values of ρ_{K0} are 0.0013 μΩ·cm and 0.0067 μΩ·cm, respectively. ρ_{K0} or ${\tau_{eK0}}^{-1}$ represents the ρ_K or ${\tau_{eK}}^{-1}$ value at $T << T_K$.

Despite the small magnitudes of ρ_{K0}, the fitted values are of high confidence. The curves are fitted well by Eq. (4.4). The three terms have distinct temperature dependence and can be clearly resolved. With an increasing T, ρ_{def} remains a constant, $\rho_K(T)$ decreases, and $\rho_{ph}(T) = AT^5$ increases. The fitted ρ_{def} ranges between 0.4 and 1.0 μΩ·cm among 20 devices. Such variations, which are temperature independent, have no impact on the low T upturn and fitted ρ_{K0}. The fitted ρ_{K0} varies by factor of 10 between 0.001 and 0.01 μΩ·cm and shows no apparent dependence on ρ_{def}.

To extract α_{def}, α_{ph}, and α_K, we fit Eq. (4.2) to the ${\tau_s}^{-1}(T)$ data by using the empirical data of ${\tau_{e,def}}^{-1}$, ${\tau_{e,ph}}^{-1}(T)$, and ${\tau_{eK}}^{-1}(T)$ obtained from the measured $\rho_{cu}(T)$ and fitting. More specifically, ${\tau_{e,def}}^{-1}$ can be obtained from the fitted ρ_{def} and ${\tau_{eK}}^{-1}(T)$ from the fitted ρ_{K0} and Eq. (4.3). For ${\tau_{e,ph}}^{-1}(T)$ we use the relation $\rho_{ph}(T) = \rho_{cu}(T) - \rho_{def} - \rho_K(T)$. We do not use $\rho_{ph}(T) = AT^5$ because it significantly deviates from experimental data when T > 20 K. The empirical data sets of ${\tau_{e,def}}^{-1}$, ${\tau_{e,ph}}^{-1}(T)$, and ${\tau_{eK}}^{-1}(T)$ are substituted into Eq. (4.2). The fitting procedure automatically adjusts parameters α_{def}, α_{ph}, and α_K until the generated ${\tau_s}^{-1}(T)$ curve provides the best fit to the experimental ${\tau_s}^{-1}(T)$ data. The best fits for α_K are 0.30 ± 0.03 and 0.066 ± 0.006 and the best fits for α_{ph} are (8.4 ± 0.3) × 10^{-4} and (9.3 ± 0.4) × 10^{-4} for devices 11-33 and 12-32, respectively. While the α_{ph} values are comparable, the α_K values are quite different. Again, the results point to the unusual scaling for Kondo spin relaxation.

We should justify the assumed linear relation ${\tau_{sK}}^{-1}(T) = \alpha_K \cdot {\tau_{eK}}^{-1}(T)$ under varying T in Eq. (4.2). In Figure 4.5 (c), ${\tau_s}^{-1}$ is plotted versus ${\tau_{eK}}^{-1}$ between 5 K and 30 K for the two NLSVs and we observe clear linear dependences. At $T \leq 30$ K, the variation of ${\tau_s}^{-1}$ should be dominated by ${\tau_{sK}}^{-1}$, because ${\tau_{s,def}}^{-1}$ is T independent and ${\tau_{s,ph}}^{-1}$ is negligible compared to ${\tau_{sK}}^{-1}$. Therefore, Figure 4.5 (c) confirms the linear relation between ${\tau_{sK}}^{-1}(T)$ and ${\tau_{eK}}^{-1}(T)$ under varying T. In addition, the slopes of the linear fittings to the ${\tau_s}^{-1}$ versus ${\tau_{eK}}^{-1}$ data are very close to the fitted α_K values using Eq. (4.2). Similarly, linear relation for phonons between ${\tau_{s,ph}}^{-1}(T)$ and ${\tau_{e,ph}}^{-1}(T)$ is also verified in Figure 4.5 (d). The data of ${\tau_{s,ph}}^{-1}$ is obtained by subtracting $\alpha_{def} \cdot {\tau_{e,def}}^{-1}$ and $\alpha_K \cdot {\tau_{eK}}^{-1}$ from the total ${\tau_s}^{-1}$. The slopes of the fitted lines are the same as the fitted α_{ph} values by using Eq. (4.2).

For a given NLSV at each temperature, ${\tau_s}^{-1}$ is calculated from λ_{cu}, which is obtained from the ΔR_s and ρ_{cu} of the NLSV and the fitted P_e value of the sample substrate (chip 11 or 12). Among these values, P_e is the major source of uncertainty for the ${\tau_s}^{-1}(T)$ curves such as those shown in Figure 4.5 (a) and (b).

The plot of fitted P_e versus T is shown in Figure 4.3 (c) with error bars for chip 11. The fitted values represent the average P_e of all NLSVs on chip 11. The top of the error bars indicates the upper bounds of P_e values, and bottom of the error bars indicates the lower bounds. For a given NLSV on the substrate, the P_e values could be above the average or below the average, depending on the quality of Py/AlO_x/Cu interfaces. But such variations should be consistent across all temperatures. In other words, if the P_e value of a device is above average at one temperature, it should be consistently above average for all temperatures. Based on this assumption, we produce three $\tau_s^{-1}(T)$ curves for device 11-33 in Figure 4.7 to reflect the influence of the uncertainties of P_e. The green circles are data based on the upper bounds of the P_e values across all temperatures. The blue triangles are data based on the lower bounds of P_e values. The red squares are data based the averaged P_e values and are essentially the same as the τ_s^{-1} versus T data shown in Figure 4.5 (a).

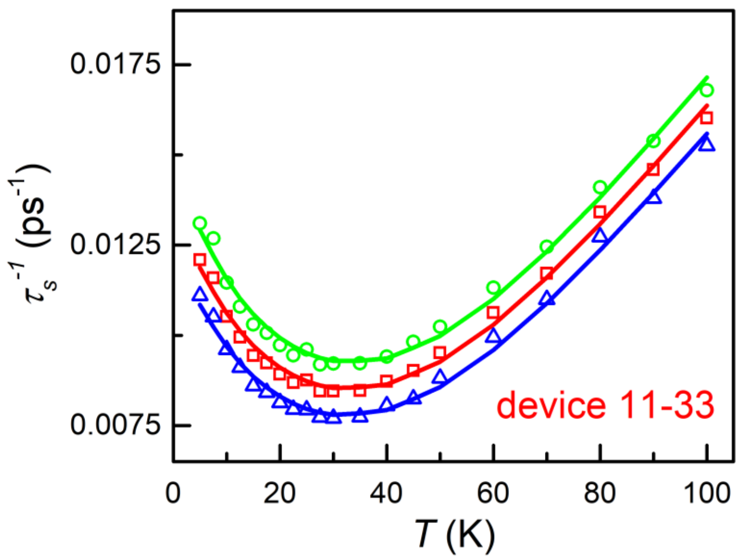

Figure 4.7: τ_S^{-1} versus T data and fitting lines based on upper bounds of P_e (green), average P_e values (red), and lower bounds of P_e (blue) for device 11-33.

It is obvious that the uncertainties of P_e move the $\tau_s^{-1}(T)$ curves up and down vertically. However, the low temperature upturn $\Delta\tau_s^{-1}$ is not strongly affected. The $\Delta\tau_s^{-1}$ values obtained from the three curves are quite similar: 3.8×10^{-3} ps^{-1}, 3.6×10^{-3} ps^{-1}, and 3.4×10^{-3} ps^{-1} for the upper (green), middle (red), and lower (blue) curves, respectively. Therefore, we can conclude $\Delta\tau_s{}^{-1}$ = (3.6 ± 0.2) × 10^{-3} ps^{-1} for device 11-33. The solid lines in Figure 4.7 are fitting lines by using Eq. (4.2). The fitted α_K values from the three sets of data are quite similar, leading to moderate or small uncertainties of α_K as shown in Figure 4.8.

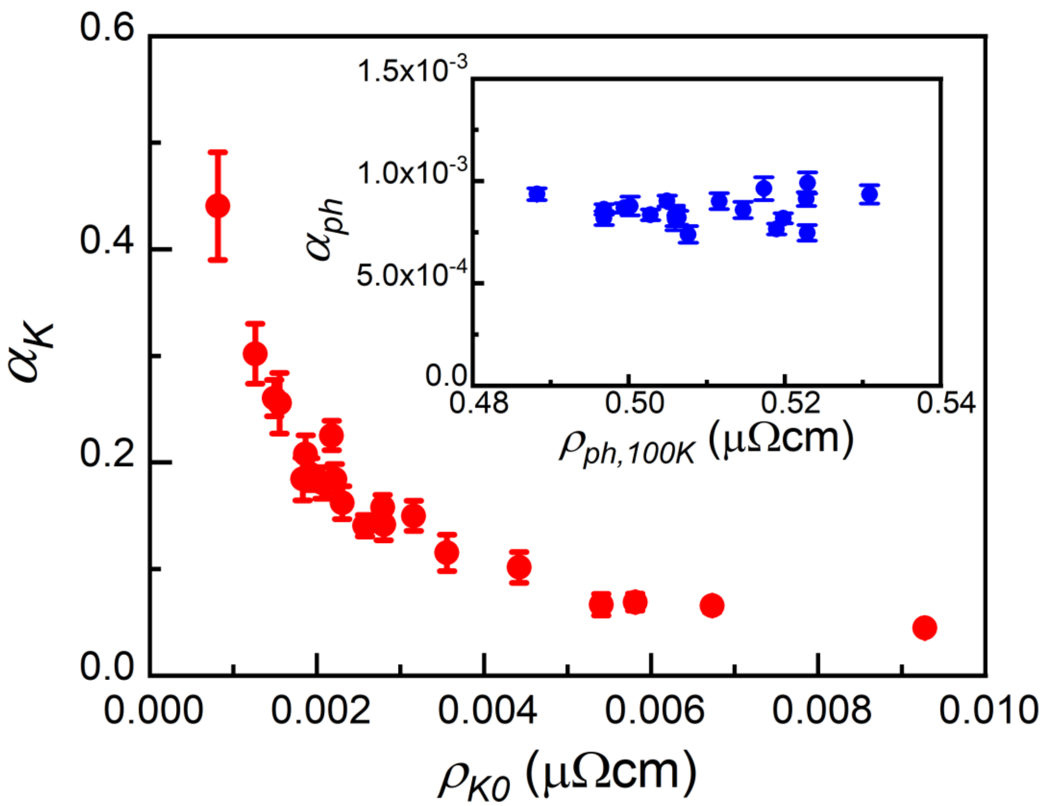

Figure 4.8: Kondo spin flip probability α_K versus Kondo resistivity ρ_{K0}. Inset: Phonon spin flip probability α_{ph} versus 100 K phonon resistivity $\rho_{ph,100K}$.

Next, we demonstrate the unusual relation between $\tau_{sK}{}^{-1}$ and $\tau_{eK}{}^{-1}$ under a varying impurity concentration C_{Fe} which is proportional to ρ_{K0} or $\tau_{eK0}{}^{-1}$ [28]. Figure

4.8 shows the fitted α_K versus ρ_{K0} for all 20 NLSVs. Strikingly, α_K decreases drastically from 0.44 ± 0.05 to 0.045 ± 0.004 as ρ_{K0} ($\propto {\tau_{eK0}}^{-1}$) increases from < 0.001 μΩ·cm to > 0.009 μΩ·cm. As a comparison, the inset of Figure 4.8 shows α_{ph} versus $\rho_{ph,100K}$, which is the ρ_{ph} at 100K, for all NLSVs. α_{ph} remains nearly a constant and independent of $\rho_{ph,100K}$ as expected for processes governed by EY mechanism. The average α_{ph} (~ 8.5 × 10^{-4}) is in good agreement with previous works [15,26,31].

The average α_{def} is 3.2 × 10^{-4} and the data are shown in Figure 4.9. α_{def} shows no particular dependence on the ρ_{def} and can be roughly regarded as a constant within uncertainties. This is consistent with the Elliott-Yafet mechanism. The average value of α_{def} is (3.2 ± 0.6) × 10^{-4}. We note that there are different types of defects such as impurities, grain boundaries, and surfaces. The variations of these contributions between devices might be responsible for the larger dispersion of α_{def} as compared to α_{ph} and α_K shown in Figure 4.8.

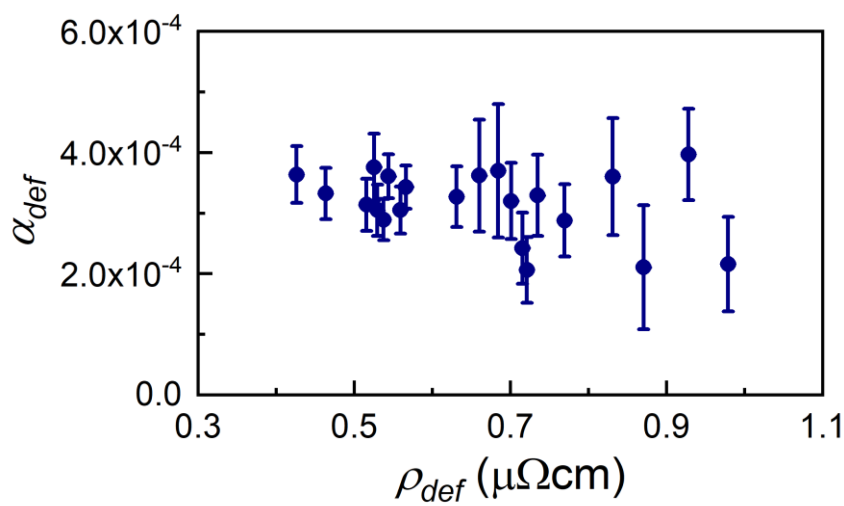

Figure 4.9: Plot of α_{def} versus ρ_{def}.

The decreasing trend in Figure 4.8 suggests that the relation between ${\tau_{sK0}}^{-1}$ and ${\tau_{eK0}}^{-1}$ is not linear, where ${\tau_{sK0}}^{-1}$ is the value of ${\tau_{sK}}^{-1}$ at $T << T_K$. Figure 4.10 (a) shows ${\tau_{sK0}}^{-1}$, obtained by using the definition ${\tau_{sK0}}^{-1} = \alpha_K \cdot {\tau_{eK0}}^{-1}$, versus ${\tau_{eK0}}^{-1}$. While ${\tau_{eK0}}^{-1}$ varies by a factor of 10, ${\tau_{sK0}}^{-1}$ stays nearly constant clearly excluding a

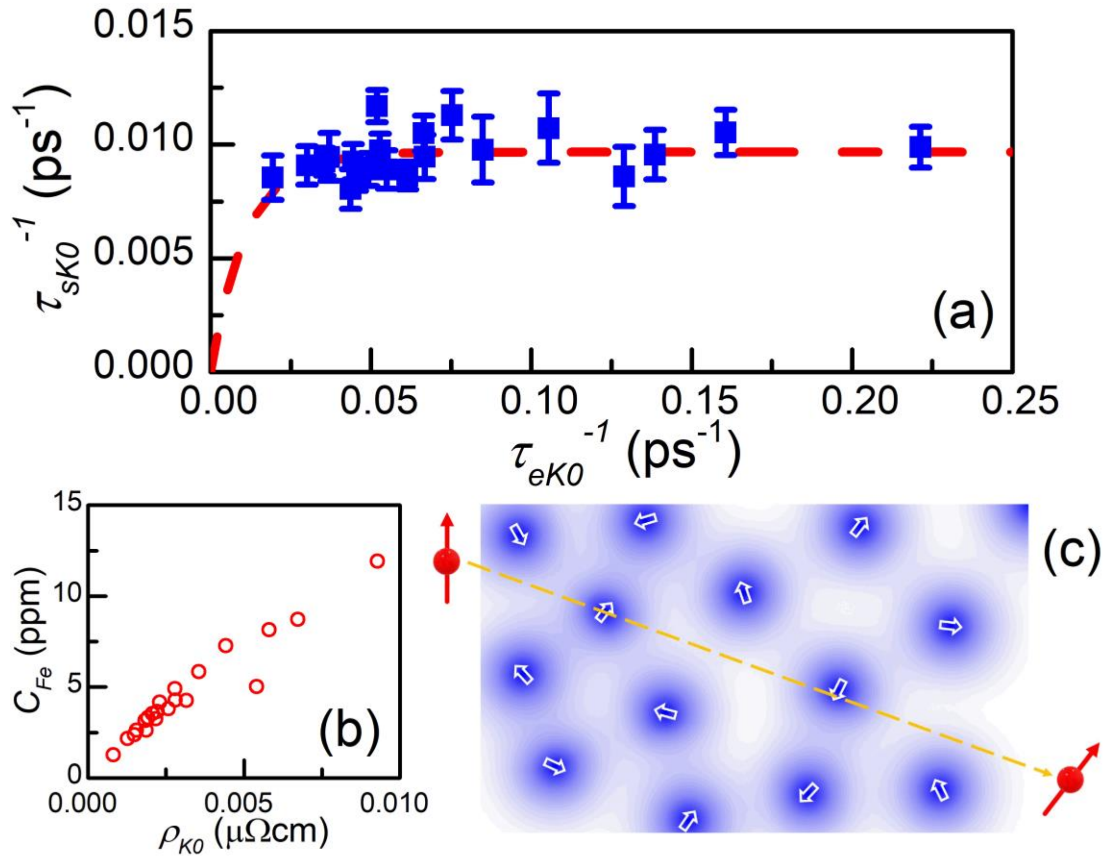

Figure 4.10: (a) Kondo spin relaxation rate τ_{sK0}^{-1} versus Kondo momentum relaxation rate τ_{eK0}^{-1} from 20 NLSVs. (b) Fe impurity concentration C_{Fe} versus ρ_{K0}. (c) Illustration of the Kondo medium. The gray scale indicates the spin density, and the white arrows indicate the polarization directions of the domains.

linear dependence. This relation obtained from the fitting method is quite consistent with the $\Delta\tau_s{}^{-1}$ versus $\Delta\rho_{cu}$ dependence, which is extracted directly from the experimental $\rho_{cu}(T)$ and $\tau_s{}^{-1}(T)$ curves and shown in Figure 4.6.

The few previous studies of Kondo spin relaxation assume linear relations and yield constant α_K of ~ 1/3 by Batley et al. [13] and ~ 2/3 by Kim et al. [28] The high spin relaxation probabilities reflect the antiferromagnetic nature of the exchange process. The relations shown in Figure 4.8 and 4.10 (a) deviate from these results and have been neither anticipated nor addressed previously. Based on previous theoretical works, Kim et al. showed explicitly that the expression of ρ_{K0} or $\tau_{eK0}{}^{-1}$ is proportional to the impurity concentration C_{Fe} [28]. The C_{Fe} for each NLSV can be extracted from the temperature T_{min} that corresponds to the minimum of the fitted $\rho_{cu}(T)$ curve [27,32]. The range of C_{Fe} in our devices is between 1 and 12 ppm, which is significantly lower than the 100 to 200 ppm by Hamaya *et al*. [14] Figure 4.10 (b) shows the extracted C_{Fe} versus ρ_{K0} for all NLSVs. Therefore, Figure 4.10 (a) suggests that Kondo spin relaxation remains nearly constant as the impurity concentration increases by one order of magnitude. The interactions between impurity spins should be negligible because C_{Fe} is very dilute and < 12 ppm as shown in Figure 4.10 (b).

4.4 Physical pictures

The unusual scaling can be understood by considering the Kondo clouds, which act as momentum scattering barriers as well as spin scattering barriers for conduction electrons passing through them [33]. While $\tau_{eK}{}^{-1}$ should be proportional to the average charge density, $\tau_{sK}{}^{-1}$ should be proportional to the average spin density of the cloud. $\tau_{sK}{}^{-1}$ may also be related to the relative orientation between the conduction electron spin and the polarization direction of the cloud.

The size of a single Kondo cloud is $\xi_K = \sqrt{\hbar D / k_B T_K} \approx 100$ nm for diffusive Cu channels. The average distance between Fe impurities is 10 nm < d_{Fe} < 20 nm, estimated from the C_{Fe} of our NLSVs, and obviously $\xi_K > d_{Fe}$. Therefore, the Kondo clouds from adjacent impurities overlap and form a continuous medium in the Cu channel. The charge density of overlapping clouds should simply add up. However, the spin density may cancel out because the polarization directions of the clouds are random. Figure 4.10 (c) is a cartoon illustration of the spatial distributions of spin density and polarization directions of the Kondo medium. Domains with random polarization directions are formed in the medium around impurity sites.

When a conduction electron traverses through the medium, the ${\tau_{eK0}}^{-1}$ or ${\tau_{sK0}}^{-1}$ should be proportional to the average charge density or the average spin density of the medium, respectively, along the electron's path. The influence of the polarization directions on ${\tau_{sK0}}^{-1}$ can be neglected because the traversing electron passes through many ($\sim 10^4$) randomly oriented Kondo domains within the time of τ_{sK0}. A higher C_{Fe} leads to a higher charge density and a higher ${\tau_{eK0}}^{-1}$, but not necessarily to a higher spin density or ${\tau_{sK0}}^{-1}$ because of the cancellation effect of overlapping clouds. The exact trend is challenging to predict without the precise knowledge of the spatial distributions of spin and charge densities of the Kondo medium. From Figure 4.10 (a), we infer that the average spin density of the medium maintains a nearly constant value within the range of 1 ppm < C_{Fe} < 12 ppm, corresponding to 10 nm < d_{Fe} < 20 nm. The red curve in Figure 4.10 (a) is a guide to the eye with the assumption that ${\tau_{sK0}}^{-1} \to 0$ as ${\tau_{eK0}}^{-1} \to 0$. We speculate that the initial slope of the curve, representing α_k in the limit of ${\tau_{eK0}}^{-1} \to 0$, should be a constant as predicted by the theory [2].

4.5 Conclusions

In conclusion, we extract the Kondo momentum relaxation rate ${\tau_{eK0}}^{-1}$ and the Kondo spin relaxation rate ${\tau_{sK0}}^{-1}$ from Cu-based nonlocal spin valves with Fe impurities. While ${\tau_{eK0}}^{-1}$ is tuned by a factor of 10 by varying Fe concentrations, ${\tau_{sK0}}^{-1}$ remains nearly constant and defies a more intuitive linear dependence on ${\tau_{eK0}}^{-1}$. Such a relation can be understood by considering spin relaxation through overlapping Kondo clouds and provides evidence for the Kondo screening clouds.

REFERENCES

[1] W. J. De Haas and G. J. Van Den Berg, Physica **3**, 440 (1936).

[2] J. Kondo, Progress of Theoretical Physics **32**, 37 (1964).

[3] V. Chandrasekhar, C. Van Haesendonck, and A. Zawadowski, *Kondo Effect and Dephasing in Low-Dimensional Metallic Systems* (Kluwer Academic Publishers, 2000).

[4] I. Affleck, arXiv:0911.2209 (2009).

[5] E. S. Sorensen and I. Affleck, Phys Rev B **53**, 9153 (1996).

[6] J. B. Boyce and C. P. Slichter, Physical Review Letters **32**, 61 (1974).

[7] M. A. Blachly and N. Giordano, Phys Rev B **51**, 12537 (1995).

[8] I. V. Borzenets, J. Shim, J. C. H. Chen, A. Ludwig, A. D. Wieck, S. Tarucha, H. S. Sim, and M. Yamamoto, Nature **579**, 210 (2020).

[9] D. Goldhaber-Gordon, J. Gores, M. A. Kastner, H. Shtrikman, D. Mahalu, and U. Meirav, Physical Review Letters **81**, 5225 (1998).

[10] M. Johnson and R. H. Silsbee, Physical Review Letters **55**, 1790 (1985).

[11] F. J. Jedema, A. T. Filip, and B. J. van Wees, Nature **410**, 345 (2001).

[12] L. O'Brien, M. J. Erickson, D. Spivak, H. Ambaye, R. J. Goyette, V. Lauter, P. A. Crowell, and C. Leighton, Nat Commun **5**, 3927 (2014).

[13] J. T. Batley, M. C. Rosamond, M. Ali, E. H. Linfield, G. Burnell, and B. J. Hickey, Phys Rev B **92**, 220420(R) (2015).

[14] K. Hamaya, T. Kurokawa, S. Oki, S. Yamada, T. Kanashima, and T. Taniyama, Phys Rev B **94**, 140401(R) (2016).

[15] J. D. Watts, L. O'Brien, J. S. Jeong, K. A. Mkhoyan, P. A. Crowell, and C. Leighton, Physical Review Materials **3**, 124409 (2019).

[16] R. J. Elliott, Physical Review **96**, 266 (1954).

[17] Y. Yafet, Phys. Lett. A **98**, 287 (1983).

[18] M. I. Dyakonov and V. I. Perel, Soviet Physics Solid State,Ussr **13**, 3023 (1972).

[19] X. J. Wang, H. Zou, L. E. Ocola, and Y. Ji, Appl Phys Lett **95**, 022519 (2009).

[20] Y. J. Cai, Y. M. Luo, C. Zhou, C. Qin, S. H. Chen, Y. Z. Wu, and Y. Ji, Journal of Physics D: Applied Physics **49**, 185003 (2016).

[21] G. L. Chen and N. Giordano, Physical Review Letters **66**, 209 (1991).

[22] M. Johnson, Physical Review Letters **70**, 2142 (1993).

[23] T. Kimura, T. Sato, and Y. Otani, Physical Review Letters **100**, 066602 (2008).

[24] G. Mihajlovic, J. E. Pearson, S. D. Bader, and A. Hoffmann, Physical Review Letters **104**, 237202 (2010).

[25] H. Zou and Y. Ji, Appl Phys Lett **101**, 082401 (2012).

[26] E. Villamor, M. Isasa, L. E. Hueso, and F. Casanova, Phys Rev B **87**, 094417 (2013).

[27] L. O'Brien, D. Spivak, J. S. Jeong, K. A. Mkhoyan, P. A. Crowell, and C. Leighton, Phys Rev B **93**, 014413 (2016).

[28] K. W. Kim, L. O'Brien, P. A. Crowell, C. Leighton, and M. D. Stiles, Phys Rev B **95**, 104404 (2017).

[29] T. Kimura and Y. Otani, J. Phys.-Condes. Matter **19**, 165216 (2007).

[30] J. M. Ziman, *Electrons and Phonons* (Clarendon Press, Oxford, 1960).

[31] P. Monod and F. Beuneu, Phys Rev B **19**, 911 (1979).

[32] J. P. Franck, D. L. Martin, and F. D. Manchester, Proceedings of the Royal Society of London Series A-Mathematical and Physical Sciences **263**, 494 (1961).

[33] P. Simon and I. Affleck, Phys Rev B **68**, 115304 (2003).

Chapter 5

TUNING OF SPIN RELAXATION AND THE KONDO EFFECT IN COPPER THIN FILMS BY IONIC GATING

5.1 Introduction

The research of spintronics has evolved rapidly to encompass a broad range of ideas and materials systems, some of which may lead to disruptive technologies for computer memory and logic, quantum information processing [1,2], and neuromorphic computing [3]. Many of the essential spintronic functionalities are carried by the spin current, which is a flow of electronic spin angular momentum. While a spin current is often accompanied by a charge current, a pure spin current without a net charge current can be generated as well. Two major challenges to the practicality of spin current are the lack of tunability and the ubiquitous spin relaxation. A tunable spin current has been desired since the inception of spintronics [4] but remains a major challenge despite some encouraging progress [5]. The spin relaxation occurs in all materials and results in an exponential decay of the injected spin current over distance. The characteristic decay length is known as the spin diffusion length λ. A short λ leads to a rapidly diminishing spin current that hinders the application potential.

Spin diffusion lengths in various materials span a broad range from a few nanometers [6] to exceeding 100 micrometers [7]. Achieving a long spin diffusion length is non-trivial: λ depends not only on the material itself but also on its crystallinity, dimensions, microstructures, and surface conditions. The exact factors that influence spin relaxation are yet fully understood. For a specific material in a given spin transport structure, however, the spin diffusion length is typically a fixed quantity. The prospect of a tunable spin diffusion length by an electric voltage is intriguing and naturally leads to a tunable spin current. In this manner, the spin current tunability can be achieved by taking advantage of the spin relaxation processes occurring in all materials.

Two dimensional (2-D) materials have been leading the way in gate tunable spin relaxation. Anisotropy in spin relaxation has been observed in graphene heterostructures [8,9] or bilayer graphene [10] and attributed to the spin-orbit effects. A gate voltage tunes the spin-orbit effects and thereby the spin relaxation [10]. In black phosphorous, the spin relaxation strongly depends on the carrier concentration, which can be modulated by an electrical gate [11]. Metallic materials, on the other hand, have not been explored for tunable spin relaxation, because their charge screening length is short and electric fields cannot influence the bulk of the metal. However, several metals, such as Cu, Ag, and Al, have substantial spin diffusion lengths and are desirable materials for spin transport channels [12-15]. One recent study shows an average λ of 2.6 μm at 30 K in submicron Cu channels [15]. Metallic materials also have the advantage of straightforward fabrication and being able to accommodate a much larger spin current than 2-D materials. The capability of tuning the spin diffusion length on demand in metals will be a valuable addition.

In this work, we demonstrate that the spin diffusion length λ_{cu}, the resistivity ρ_{cu}, and the Kondo effect in Cu thin films can be effectively tuned by using the ionic gating technique [16-23]. A polymer electrolyte, polyethylene oxide (PEO) and Lithium Perchlorate ($LiClO_4$), is applied between a metal gate and a submicron Cu-based nonlocal spin valve (NLSV) [13,24,25] as the gating medium [26]. At room temperature (RT), a positive (negative) gate voltage V_g induces an accumulation of Li^+ (ClO_4^-) ions on the surfaces of the NLSV. The electrolyte freezes below 273 K and low temperature gating is achieved by cooling the NLSV under a V_g from 295 K.

At 5 K, λ_{cu} is tuned between 670 nm and 410 nm reversibly in a gated NLSV, resulting in the modulation of the nonlocal spin signal by a factor of 3. In addition, ρ_{cu} is tuned by 8.7% and the strength of the Kondo effect is tuned by one order of magnitude. Tuning of ρ_{cu} and λ_{cu} has been achieved at RT as well, though the tuning ranges are smaller than those at 5 K. Upon repeated gate cycling, both λ_{cu} and its tuning range gradually increase suggesting an electrochemical origin. We further hypothesize that Li ions/atoms diffuse into and out of the Cu channel along the grain boundaries under ionic gating and induce the observed tuning effects. Though the ionic gating technique has been widely used for tuning charge-transport properties of oxides, superconductors, 2-D materials, and even metals [16-23], tuning of spin-transport properties, such as λ, in mesoscopic NLSV devices has not been pursued previously.

5.2 Sample fabrication and measurement

Figure 5.1 (a) is a cartoon illustration of the mesoscopic experimental structure and Figure 5.1 (b) is a scanning electron microscope (SEM) image of the structure before the ionic gel is applied. The key component of the structure is a metallic NLSV, which consists of a spin injector (F_1) and a spin detector (F_2), both ferromagnetic, as well as a nonmagnetic Cu channel. The spin relaxation process in Cu can be quantitatively investigated by using the NLSV. In Figure 5.1 (a) and (b), F_1 and F_2 are the pair of parallel stripes underneath the Cu channel, and they are made of $Ni_{81}Fe_{19}$ alloy known as permalloy (Py). A 3-nm layer of AlO_x is placed between the Py stripes

(F_1 and F_2) and the Cu channel to enhance the efficiency of spin injection and spin detection for F_1 and F_2, respectively [25,27]. In addition to the NLSV, a Cu gate

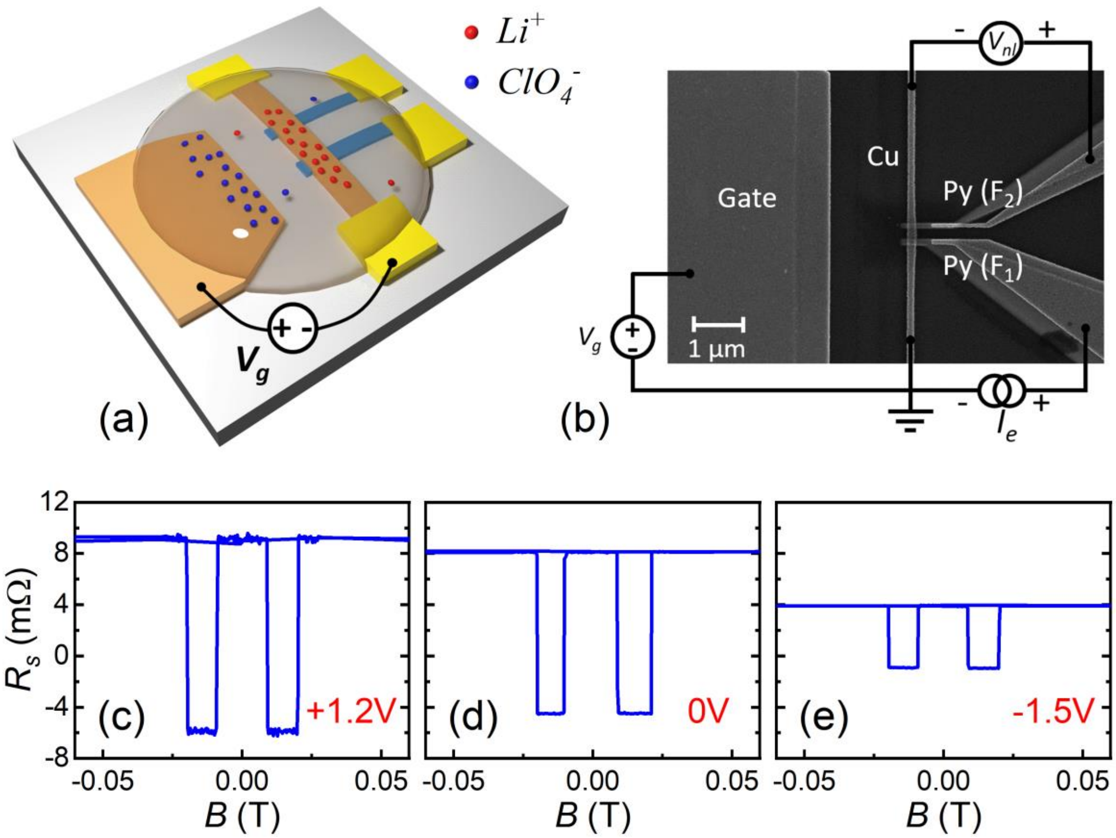

Figure 5.1: (a) A cartoon illustration of ionic gating on a NLSV. (b) The SEM image of a NLSV with a side gate. R_s versus B curves of the NLSV device with L = 800 nm at 5 K after cooling the device from 295 K under V_g of (c) +1.2 V, (b) 0 V, and (c) -1.5 V.

electrode is patterned 2 or 5 micrometers away from the Cu channel for the ionic gating purpose. To fabricate the entire structure, electron beam lithography is used to create a mesoscopic shadow mask via two layers of electron beam resist on a Si substrate. Subsequently, Py is deposited from an oblique angle and AlO_x and Cu are deposited along the substrate normal direction through the shadow mask [25,27]. This angle deposition method ensures the pristine quality of the spin injection/detection interfaces Py/AlO_x/Cu at F_1 and F_2, because they are formed without breaking the chamber vacuum.

The spin injection and detection method can be explained by referring to the circuity in Figure 5.1 (b). An electric current I_e flows from F_1 toward the grounded end of the Cu channel and injects spin polarized electrons across the F_1/AlO_x/Cu interface into Cu. A split between the spin-up and spin-down electrochemical potentials, also known as a spin accumulation, is induced in Cu but decays exponentially over distance due to the spin relaxation. The gradient of the spin accumulation drives diffusive spin currents toward both ends of the Cu channel. F_2 is used as a spin-dependent detector to probe the spin accumulation in Cu. A nonlocal voltage V_{nl} is measured between F_2 and the floating end of the Cu channel. The nonlocal resistance $R_s = V_{nl}/I_e$ is recorded as a function of a magnetic field B applied parallel to F_1 and F_2 stripes. Example R_s versus B curves are shown Figure 5.1 (c) through (e). As the B field is swept, parallel (P) and antiparallel (AP) alignments between the F_1 and F_2 magnetizations can be reached. The high values of R_s correspond to the P state and the low values to the AP state.

The difference between P and AP states is the spin signal ΔR_s and is proportional to the spin accumulation in the Cu channel at the location of F_2. Quantitatively, ΔR_s is given by [28]:

$$\Delta R_s = \frac{P_1 P_2 \rho_{cu} \lambda_{cu}}{A} e^{-\frac{L}{\lambda_{cu}}} \tag{5.1}$$

where P_1 and P_2 are the effective spin polarizations of F_1 and F_2 across the Py/AlO_x/Cu interfaces, respectively, L is the center to center distance between F_1 and F_2, and A is the cross-sectional area of the channel. It is common to assume $P_1 = P_2 = P_e$ when F_1 and F_2 have similar widths and thicknesses. As L increases, ΔR_s decreases exponentially with a characteristic decay length λ_{cu} as expected with spin relaxation. A standard method of finding λ_{cu} is to fit Eq. (5.1) to the data of ΔR_s versus L for a series of NLSVs with varying L. Alternatively, λ_{cu}can also be directly calculated from the measured ΔR_s of a single NLSV by using Eq. (5.1) if P_e and ρ_{cu} are known. Note that ρ_{cu} can be measured directly on the NLSV by sending in a current through the Cu channel and measuring the voltage drop between F_1 and F_2.

The ionic gel of the electrolyte is prepared by mixing lithium perchlorate ($LiClO_4$) and polyethylene oxide (PEO) and then dissolving the mixture in methanol and deionized water at the proper ratio. A drop of the liquid is applied to the structure covering both the gate and the NLSV. The sample is left in air for 30 minutes for the methanol and water to evaporate and subsequently placed into the sample tube of a variable temperature cryostat. The sample tube is evacuated to vacuum and back filled with helium exchange gas at 295 K. Measurements can be conducted between 295 K and 5 K.

As illustrated in Figure 5.1 (a) and (b), a voltage source connected between the gate and the Cu channel provides the gate voltage V_g. At RT, Li^+ and $ClO4^-$ ions are driven by V_g to move through PEO and accumulate on the negative and positive electrodes, respectively. Under a positive V_g, for example, Li^+ accumulate on the surfaces of the Cu channel as illustrated in Figure 5.1 (a). Upon electrolyte freezing below 273 K, the ion accumulation on the Cu surface cannot be altered by changing or removing V_g. The gating measurements at cryogenic temperatures are performed by setting the desired V_g at 295 K and cooling the device under this V_g to temperatures below 250 K. To reset V_g, the sample is first warmed up to 295 K before a different V_g can be effectively applied.

More than 10 NLSV devices have been measured and consistently show the tuning effects. In the following we focus on the data from one device, which has been measured for both ρ_{cu} and λ_{cu} at various temperatures under prolonged gate cycling. The Cu channel of this device has a cross sectional area of A = 200 × 65 nm^2 with 200 nm being the width and 65 nm being the thickness. The length of the channel between the centers of F_1 and F_2 is L = 800 nm. The distance between the gate and the Cu channel is 5 μm.

5.3 Low temperature tuning of spin diffusion length and resistivity

Here we describe the gating measurements at low temperatures, where the largest tuning of λ_{cu} has been observed. The NLSV device is cooled from 295 K to 5 K under three different V_g values of +1.2 V, 0 V, and - 1.5 V, and distinctly different ΔR_s values of 15 mΩ, 13 mΩ, and 5 mΩ, respectively, are measured at 5 K as shown in Figure 5.1 (c) through (e). While the positive V_g results in a larger ΔR_s, the negative V_g leads to a smaller ΔR_s that is only 1/3 of the former. Such a dramatic change of spin signal in the same NLSV is striking. The change can be reversed by warming up the device to 295 K and cooling down under the opposite V_g. ΔR_s as a function of T between 5 K and 250 K has been measured and shown in Figure 5.2 (a) for the three V_g values, and clearly the differences in ΔR_s are maintained at all temperatures. The unusual decease of ΔR_s at lower T (< 40 K) is a well-documented sign of the enhanced spin relaxation by the Kondo effect [15,29,30].

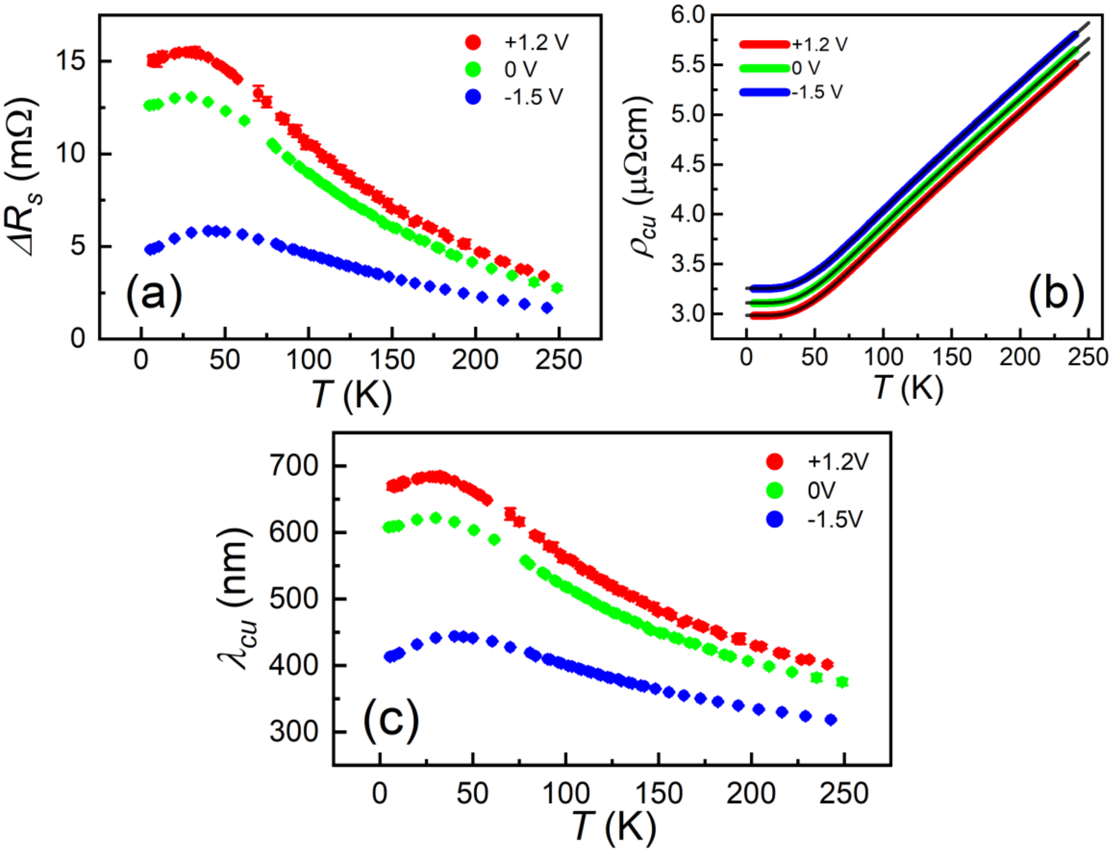

Figure 5.2: (a) The spin signal and (b) the Cu resistivity as a function of T as the NLSV is cooled under various V_g. Solid lines in (b) are fits by using the Bloch-Grüneisen term for phonon resistivity. (c) Derived λ_{cu} as functions of T under various V_g values.

The tuning of ΔR_s arises primarily from the tuning of λ_{cu} as justified in the following. In Eq (1) ΔR_s is related to a few parameters. While L and A are geometrical and are unlikely to be affected by the gating, a change in ΔR_s may be potentially traced to the changes in P_e, λ_{cu} or ρ_{cu}. P_e is determined by the intrinsic polarization of Py as well as the Py/AlO_x/Cu interfaces. λ_{cu} and ρ_{cu} reflect the properties of the Cu channel. The Py electrodes and the Py/AlO_x/Cu interfaces are unlikely to be affected by the gating because they are buried underneath the 65 nm thick Cu channel. To illustrate this point further, we perform gating measurements on NLSVs which have 65 nm thick Al channels but are otherwise similar to the Cu-based NLSVs. Despite applied V_g up to 3.5 V in both polarities, no tuning of ΔR_s or ρ_{cu} has been observed. The spin signals from one of the Al-based NLSVs, shown in Figure 5.3 (a) and (b), are ΔR_s = 4.0 mΩ under both V_g = +3.5 V and V_g = -3.5 V at 295 K. This illustrates that the ionic gating cannot directly tune P_e by affecting the Py film or the Py/AlO_x interface through a 65 nm nonmagnetic film.

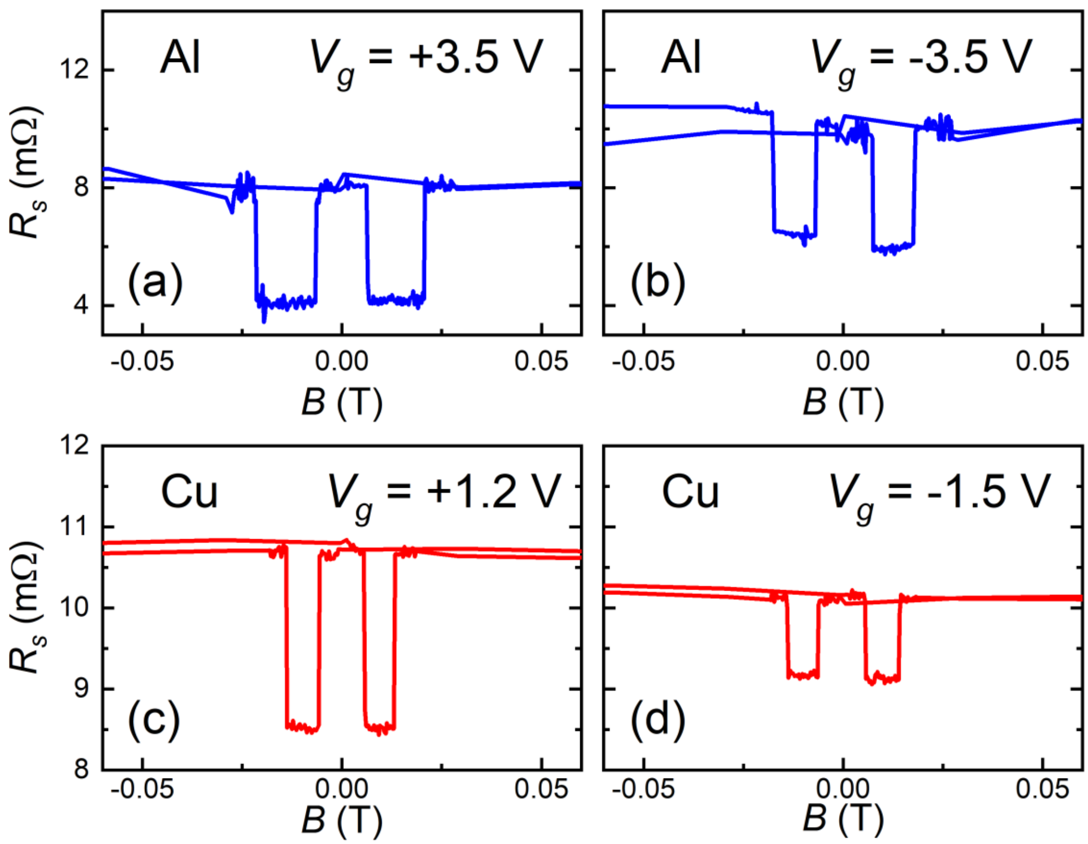

Figure 5.3: R_s versus B curves for a NLSV with an Al channel under V_g of (a) +3.5 V and (b) -3.5 V at 295 K. R_s versus B curves for the Cu-based device under V_g of (c) +1.2 V and (d) -1.5 V at 295 K.

In contrast, the spin signals for the Cu-based device under opposite V_g values are clearly different even at 295 K, as shown in Figure 5.3 (c) and (d). ΔR_s = 2.2 mΩ under V_g = +1.2 V and ΔR_s = 1.0 mΩ under V_g = -1.5 V. This gate-induced change in ΔR_s should primarily come from the tuning of Cu properties (λ_{cu} and ρ_{cu}). When $|V_g|$ > 2.0 V is applied to the Cu channels, irreversible electrochemical changes usually occur. Both Al and Cu channels are covered by natural oxides. The oxide on Al is more uniform and we will discuss in section VI why ionic gating has no effect on the Al properties (λ_{Al} and ρ_{Al}) at all.

The Cu resistivity ρ_{cu} versus T under various V_g values is directly measured and shown in Figure 5.2 (b). Indeed ρ_{cu} is tuned by V_g. At 5 K, the value of ρ_{cu} under V_g = +1.2 V is 9% lower than that under V_g = – 1.5 V. To derive the tuning of λ_{cu}, we assume that $P_e = P_0\left(1 - \alpha T^{3/2}\right)$, where P_0 is the polarization at T = 0. This relation is based on the assumption that P_e scales with the Py magnetization which follows a temperature dependence that is well documented in the literature [31-33]. From our previous data [25,34] on Py/AlO_x/Cu NLSVs and taking into account the dimensions of the current device, we estimate P_0 = 0.18 and P_e = 0.10 at 295 K yielding α = 8.77 × 10^{-5} $K^{-3/2}$. By using Eq. (5.1), the relations of λ_{cu} versus T under various V_g , shown in Figure 5.2 (c), are derived from the data of ΔR_s versus T in Figure 5.2 (a), ρ_{cu} versus T in Figure 5.2 (b), and $P_1 = P_2 = P_e$. The low T downturns associated with the Kondo effect are still present.

At 5 K, λ_{cu} is tuned between 410 nm under V_g = -1.5 V and 670 nm under V_g = +1.2 V. Using λ_{cu} = 610 nm under V_g = 0 V as the baseline, 43% tuning of λ_{cu} is achieved between opposite polarities of V_g. Such large and reversible tunability of λ_{cu} on demand in metal is unprecedented. The values of ρ_{cu} and λ_{cu} under various V_g

values at 5 K are summarized in Table 5.1. The opposite trends of tuning for λ_{cu} and ρ_{cu} is qualitatively consistent with the Elliott-Yafet (EY) spin relaxation model [35,36], which predicts an inversely proportional relationship between λ_{cu} and ρ_{cu} assuming a constant spin-flip probability. The EY model assumes that spin flip events occur with a certain probability upon each momentum scattering event.

Table 5.1: The ρ_{cu} and λ_{cu} of the NLSV device under various V_g values at 5 K and 295 K. The percentage change is relative to the value under V_g = 0.

	ρ_{cu} (μΩ·cm) at 5 K	λ_{cu} (nm) at 5 K	ρ_{cu} (μΩ·cm) at 295 K	λ_{cu} (nm) at 295 K
V_g = +1.2 V	2.98	670	6.11	380
V_g = 0 V	3.11	610	6.36	350
V_g = -1.5 V	3.25	410	6.55	300
Change	8.7%	43%	6.9%	23%

The spin current through the Cu channel passing by the spin detector F_2 is $I_s = \frac{1}{2}P_1 I_e e^{-L/\lambda_s}$. To achieve effective tuning of a robust spin current in a NLSV, the spin transport channel length L should be comparable to the range of λ_{cu}. If $L << \lambda_{cu}$, the tuning effect of I_s will be minimal. If $L >> \lambda_{cu}$, the magnitude of I_s will be minimal. The current NLSV device with L = 800 nm matches well with the tuning range 410 nm ≤ λ_{cu} ≤ 670 nm. The spin current I_s near F_2 is modulated by a factor of 2.1 between $0.013I_e$ and $0.027I_e$ at 5 K. The spin signal ΔR_s, which is the nonlocal electrical voltage resulting from the spin current, is tuned by a factor of 3 as shown in Figure 5.1 (c) through (e). The reason for the different tuning factors is that the spin resistance $\rho_{cu}\lambda_{cu}/A$ has to be factored in to convert I_s into ΔR_s. Nevertheless, both the spin signal and the spin current in this mesoscopic metallic NLSV are tuned substantially.

5.4 Tuning the kondo effect

In addition to λ_{cu} and ρ_{cu}, the Kondo effect in the Cu channel is tuned by ionic gating as well. The Kondo effect arises from the antiferromagnetic exchange interaction between the localized spin of a magnetic impurity and the delocalized spins of conduction electrons of the host metal. The well-known experimental signature of

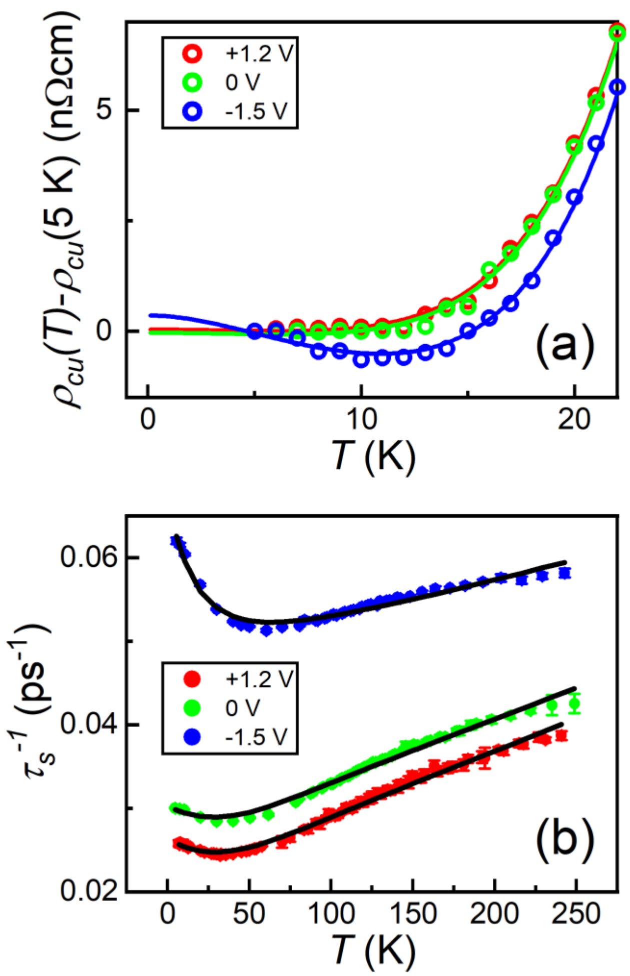

Figure 5.4: (a) The plot of $\rho_{cu}(T) - \rho_{cu}(5K)$ versus T between 5 K and 22 K for the Cu channel under various V_g values. (b) The spin relaxation rate τ_s^{-1} versus T between 5 K and 250 K under various V_g values. All solid lines are fitting lines.

the Kondo effect in metals is the increase of resistivity (or momentum relaxation rate) at low temperature. The plots of $\rho_{cu}(T) - \rho_{cu}(5K)$ versus T between 5 K and 22 K under V_g of +1.2 V, 0 V, and -1.5 V are shown in Figure 5.4 (a). The curve with V_g = -1.5 V shows a pronounced low temperature increase of ρ_{cu}, revealing the presence of the Kondo effect. The curves with V_g of 0 V and +1.2 V, however, show no obvious upturn at low temperatures. Apparently, the strength of the Kondo effect at negative V_g is much stronger than that at positive V_g.

For Cu based NLSVs with Py electrodes, it has been shown that Fe impurities in Cu channel are responsible for the Kondo effect. Fe and Ni impurities are introduced into the Cu channels unintentionally during the fabrication processes [15,29,37]. Fe impurities in Cu is well known as a Kondo system with a Kondo temperature of T_K = 30 K. But T_K for Ni impurities in Cu is above 1000 K and no Kondo features should be present in the temperature range of this study [29,38]. The total ρ_{cu} can be expressed as

$$\rho_{cu}(T) = \rho_{def} + \rho_{ph}(T) + \rho_K(T) \tag{5.2}$$

where ρ_{def}, ρ_{ph}, and ρ_K are defect, phonon, and Kondo contributions to the resistivity. While ρ_{def} is a constant, phonon resistivity can be approximated as $\rho_{ph}(T) = AT^5$ at low T. The Kondo resistivity can be described by a phenomenological formula [39]:

$$\rho_K(T) = \rho_{K0}\left(\frac{{T_K'}^2}{T^2 + {T_K'}^2}\right)^s \tag{5.3}$$

where $T_K' = T_K/\sqrt{2^{1/s} - 1}$, and s = 0.225. ρ_{K0} is the Kondo resistivity at T = 0 and scales with the Kondo momentum scattering rate. It also represents the strength of the Kondo effect in general. The values of ρ_{K0} under various V_g values are obtained by fitting Eq. (5.2) to the three curves in Figure 5.4 (a) and tabulated in Table 5.2. ρ_{K0} =

4.2×10^{-3} μΩ·cm under V_g = -1.5 V is one order of magnitude higher than ρ_{K0} = 3.3×10^{-4} μΩ·cm under V_g = +1.2 V or the value under 0 V, confirming substantial tuning of the Kondo effect strength. The concentration of Fe impurities is proportional to ρ_{K0} [40] and can be conveniently estimated by using an empirical formula that involves the temperature corresponding the resistivity minimum of the $\rho_{cu}(T)$ curve [15,37,41,42]. For this NSLV, the concertation is < 5 ppm and measurements are done at $T \geq 5$ K. Therefore, interactions between impurities, which were found at > 100 ppm and $T < 0.4$ K [43], can be neglected.

The tuning of the Kondo effect is also reflected in the data of ${\tau_s}^{-1}$ versus T in Figure 5.4 (b), where τ_s is the spin relaxation time and ${\tau_s}^{-1}$ is the spin relaxation rate of the Cu channel. τ_s is calculated from λ_{cu} by using relation $\lambda_{cu} = \sqrt{D\tau_s}$, where $D = \frac{1}{3}{v_F}^2\tau_e$ is the diffusion constant. $v_F = 1.57 \times 10^6$ m/s is the Fermi velocity of Cu and the momentum relaxation time τ_e can be obtained by using the Drude model $\rho_{cu} = m/\tau_e n e^2$, where n = 8.47×10^{28} m^{-3} is the Cu electron density, m is the electron mass, and e is the electron charge. All three ${\tau_s}^{-1}$ versus T curves under various V_g values in Figure 5.4 (b) show upturns at low temperature, which can be attributed to the enhanced spin relaxation rate due to the Kondo effect. The upturn under V_g = -1.5 V is clearly more pronounced than those under 0 V and +1.2 V. This is consistent with the more pronounced resistivity upturn associated with V_g = -1.5 V in Figure 5.4 (a).

The total spin relaxation rate can be expressed as the summation of three individual spin relaxation rates

$$\frac{1}{\tau_s(T)} = \alpha_{def}\frac{1}{\tau_{e,def}} + \alpha_{ph}\frac{1}{\tau_{e,ph}(T)} + \alpha_K\frac{1}{\tau_{eK}(T)} \tag{5.4}$$

where $\tau_{e,def}{}^{-1}$, $\tau_{e,ph}{}^{-1}$, and $\tau_{eK}{}^{-1}$ are the electron momentum relaxation rates for defects, phonon, and the Kondo effect and they are related to ρ_{def}, ρ_{ph}, or ρ_K through the Drude model, respectively. α_{def}, α_{ph}, and α_K are the respective spin relaxation probabilities for each momentum scattering type. Data in Figure 5.4 (b) can be fitted well by Eq. (5.4). The details of the fitting method are given in our previous work [15]. The fitted values of α_{def}, α_{ph}, and α_K under various V_g values are listed in Table 5.2. The values of α_K are significantly larger than α_{def} or α_{ph} by orders of magnitude. This is due to the antiferromagnetic nature of the Kondo exchange interaction, which leads to a high probability of spin relaxation at a Kondo momentum scattering event. The good quality of the fitting corroborates the conclusion from Figure 5.4 (a) that the strength of the Kondo effect can be tuned by the ionic gating.

Table 5.2: Kondo resistivity ρ_{K0}, defect resistivity ρ_{def}, parameter A, Kondo spin relaxation probability α_K, defect spin relaxation probability α_{def}, and phonon spin relaxation probability α_{ph} under various V_g values.

V_g	ρ_{K0} (μΩ·cm)	ρ_{def} (μΩ·cm)	A (μΩ·cm·K^{-5})	α_K	α_{def}	α_{ph}
+1.2 V	3.3×10^{-4}	2.98	1.30×10^{-9}	0.40	3.2×10^{-4}	2.7×10^{-4}
0 V	3.4×10^{-4}	3.11	1.30×10^{-9}	0.32	3.7×10^{-4}	2.6×10^{-4}
-1.5 V	4.2×10^{-3}	3.25	1.32×10^{-9}	0.22	5.5×10^{-4}	2.0×10^{-4}

5.5 Evolution of the gating effects at room temperature

At this point, it is natural to inquire the origin of the observed tuning effects under ionic gating. The discussion of electrochemical versus electrostatic origins has been an important theme in the literature of the ionic gating technique. Under V_g, positive or negative ions accumulate on the outer surface of the gated material and attract opposite charges on the inner surface forming an electric double layer (EDL). Due to the short distance (~ 1 nm) between opposite charges of the EDL, a strong surface electric field (> 1 V/nm) and a high surface charge density exceeding 10^{14} /cm^2 can be achieved and are capable of tuning properties of 2-D materials, ultrathin metallic films, and materials with low charge densities. In many previous works, the experimental evidence indeed points to the intense electrostatic field or/and the high charge doping as the origin of the tuning effects. In some cases [21,44-46], however, arguments for a complete or a partial electrochemical origin of the tuning have been presented. Such divergence of opinions highlights the complexity of this versatile ionic gating technique.

Some previous works on ionic gating are relevant to metallic materials and/or spintronics. Tuning of resistivity in Au films has been demonstrated and interpreted as an electrostatic effect that modulates the charge density in metal [23]. However, x-ray absorption near edge structure measurements suggested an electrochemical origin: reversible oxidation of Au films [44]. Tuning of the inverse spin Hall effect, Kondo effect, and ferromagnetism in Pt by ionic gating has been demonstrated as well [47,48]. In the following, by analyzing the evolution of the gating effects at RT, we show that an electrochemical origin is responsible for the tuning effects in Cu based NLSVs.

Clear RT tuning of spin signals are already shown in Figure 5.3 (c) and (d): ΔR_s = 2.2 mΩ under V_g = +1.2 V and ΔR_s = 1.0 mΩ under V_g = -1.5 V for the NLSV device at 295 K. The spin signal is tuned by a factor of 2.2. However, the initial tuning range of the device is much smaller and the prolonged gating measurements surprisingly amplify the range. To understand the origin of the tuning effects, it is useful to trace the evolution of gating measurements over time. Figure 5.5 (a) shows selected data of ΔR_s and V_g versus the gating measurement time t_g at RT. Figure 5.5 (b) shows selected data of ρ_{cu} and V_g versus t_g. The t_g timer starts on the initial gating measurement (t_g = 0) of the as-fabricated device and continues for any RT

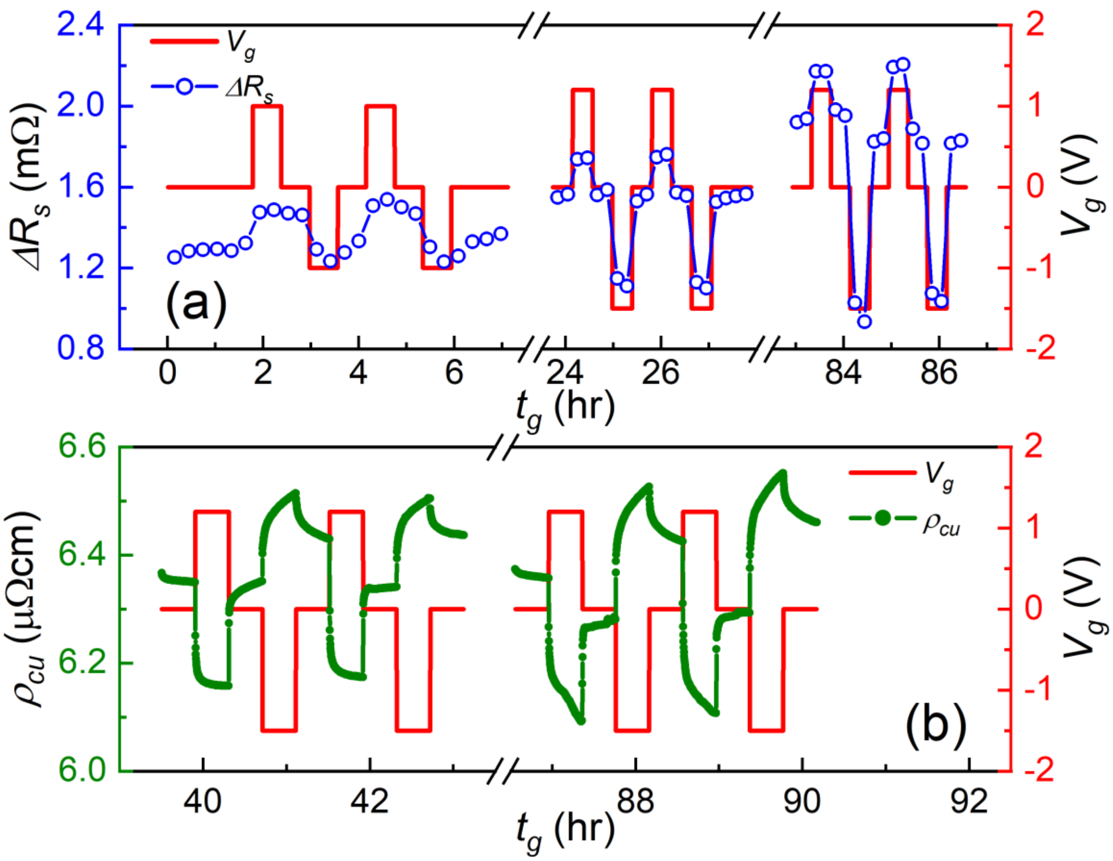

Figure 5.5: (a) The measured ΔR_s (left vertical axis) and applied V_g (right vertical axis) as functions of gating time t_g at 295 K. (b) The measured ρ_{cu} (left vertical axis) and applied V_g (right vertical axis) as a function of t_g at 295 K.

gating measurement (either ΔR_s or ρ_{cu}). The timer pauses when the device is cooled below 273 K (upon electrolyte freezing) and resumes once the device is warmed above 273 K. For this device, t_g extends to ~ 90 hr and the low T measurements shown in the previous section are mainly conducted during the time interval 60 hr < t_g< 80 hr. The RT measurements shown in Figure 5.3 (c) and (d) are conducted around t_g = 85 hr.

As shown by the solid lines in Figure 5.5, V_g is applied in a square-wave fashion and varies abruptly between zero and two opposite polarities. At each V_g, a few (2 to 4) data points are available for ΔR_s in Figure 5.5 (a) but many more data points are available for ρ_{cu} in Figure 5.5 (b), because the measurement of each ΔR_s requires sweeping magnetic field and is more time consuming. Clearly Figure 5.5 (a) shows that the tuning range of ΔR_s increases substantially over time. A moderate increase of tuning range over time is also evident for ρ_{cu} in Figure 5.5 (b).

In Figure 5.5 (a) at t_g = 0 hr, ΔR_s = 1.2 mΩ is measured under V_g = 0 V representing the spin signal of the as-fabricated device. At t_g = 2 hr, V_g = +1.0 V is applied and ΔR_s increases moderately to 1.5 mΩ, which remains even when V_g is reduced to 0 V. ΔR_s returns to 1.2 mΩ under V_g = -1.0 V completing the first gate cycle. The tuning features for the next several gate cycles (between + 1.0 V and -1.0 V) are quite similar but the tuning range $\Delta R_s^+ - \Delta R_s^-$ gradually increases, where ΔR_s^+ and ΔR_s^- are the spin signals under the positive and negative V_g, respectively. Figure 5.6 (a) shows $\Delta R_s^+ - \Delta R_s^-$ of each gate cycle versus t_g. In the first 5 gating cycles during 0 hr < t_g < 24 hr, the tuning range increases from 0.2 mΩ to 0.4 mΩ. During 24 hr < t_g < 28 hr, there are two gate cycles with V_g between +1.2 V and -1.5 V and the tuning ranges increase to 0.6 mΩ. The plots of ΔR_s and V_g versus t_g for these two gate cycles are shown in the middle section of Figure 5.5 (a). Compared to the interval

$0 < t_g < 6$ hr in the left section of Figure 5.5 (a), there is less hysteresis in the tuning features: the value of ΔR_s at V_g = 0 V following V_g = +1.2 V is the same as that following V_g = -1.5 V.

The final complete gate cycles are measured during 83 hr < t_g < 87 hr and the plot of ΔR_s versus t_g data are shown in the right section of Figure 5.5 (a). The spin signals ΔR_s are 2.2 mΩ, 1.9 mΩ, and 1.0 mΩ under V_g of +1.2 V, 0 V, and -1.5 V, respectively. ΔR_s more than doubles between opposite V_g polarities and the tuning range is 1.2 mΩ. Strikingly, the tuning range increases from merely 0.2 mΩ to 1.2 mΩ during 87 hr of gate cycling at 295 K as summarized in Figure 5.6 (a). In addition, as can be seen in Figure 5.5 (a), the value of ΔR_s at V_g = 0 V also increases from 1.2 mΩ in the as-fabricated device to 1.9 mΩ in the same device after 87 hr of gate cycling. The evolution of the tuning range and the value of ΔR_s at V_g = 0 V over time strongly suggests that the origin of the tuning effects is electrochemical instead of electrostatic.

As mentioned earlier in this section, the hysteresis features of the tuning effect also evolve over time. An explicit hysteresis loop of ΔR_s versus V_g can be obtained when V_g is varied in small steps between two polarities. The loop in Figure 5.6 (b) is measured between -1.0 V and +1.0 V around t_g = 12 hr, and there is an obvious hysteresis. The loop in Figure 5.6 (c) is measured between -1.2 V and +1.2 V around t_g = 31 hr, and there is essentially no hysteresis on the negative side of V_g. Though a small hysteresis remains on the positive side of V_g, ΔR_s values at V_g = 0 are almost the same for the upward and downward branches. Such evolution of hysteresis further supports the electrochemical origin.

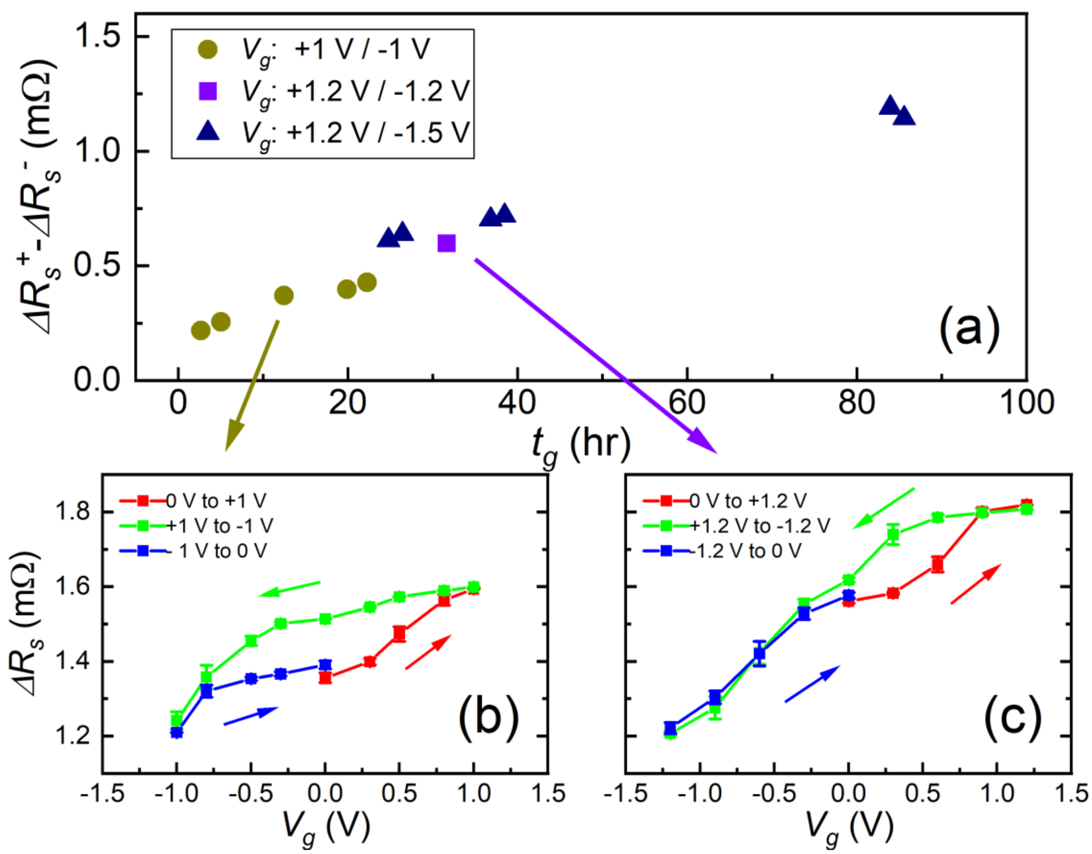

Figure 5.6: (a) The tuning range of spin signals $\Delta R_s{}^{+}$ - $\Delta R_s{}^{-}$ between positive and negative polarities of V_g for each complete gate cycle as a function of t_g for the NSLV at 295 K. Different symbols indicate the range of applied V_g. (b) Hysteresis loop of ΔR_s versus V_g around t_g = 12 hr. (c) Hysteresis loop of ΔR_s versus V_g around t_g = 31 hr.

The evolution of resistivity tuning at 295 K can be examined in Figure 5.5 (b). During 39 hr < t_g < 43 hr, ρ_{cu} is tuned by 5.5% with a lower ρ_{cu} at +1.2 V and a higher ρ_{cu} at -1.5 V. During 86 hr < t_g < 90 hr, the tuning range of ρ_{cu} is enhanced to 6.9%. To quantify the optimized tuning effects, we estimate λ_{cu} values under various V_g values at 295 K by using ΔR_s data during 83 hr < t_g < 87 hr as well as ρ_{cu} data during 87 hr < t_g < 90 hr. At +1.2 V, λ_{cu} is 380 nm and ρ_{cu} is 6.11 μΩ·cm. At -1.5 V,

λ_{cu} is suppressed to 300 nm and ρ_{cu} increases to 6.55 μΩ.cm. While λ_{cu} is tuned by 23% (relative to λ_{cu} = 350 nm under V_g = 0), ρ_{cu} is tuned by 6.9% at 295 K. The optimized tuning of λ_{cu} and ρ_{cu} at 295 K is summarized in Table 5.1.

5.6 Discussion of possible mechanisms of the tuning effects

The identification of the electrochemical origin of the gating effect in our NLSVs is an important revelation because the controversy of electrostatic versus electrochemical origins has been long standing with the ionic gating method [21,44-46]. Here we further discuss possible underlying electrochemical mechanisms. To pinpoint an exact mechanism, advanced characterization methods on the morphology and composition of the Cu channels are necessary. However, a direct probe into the mesoscopic Cu channel is very challenging because of the thick layer of solid electrolyte and the delicate nature of the nanoscale NLSVs.

Since the surfaces of the Cu channels are exposed to air and the electrolyte without capping layers, natural oxides form. Recent studies [49,50] show that O^{2-} ions can be moved by an electric field bidirectionally through a GdO_x layer to change the oxidation state of an adjacent metallic magnetic layer. It is reasonable to consider if the O^{2-} ions can be driven by the electric field of the EDL to affect λ_{cu} and ρ_{cu}. Because of the short charge screening length (~ 0.1 nm) of metal, however, electric field cannot penetrate into the bulk of Cu metal. Therefore, field-driven motion of O^{2-} ions, if any, is only confined to the surface region within one atomic layer. This mechanism is unlikely to be responsible for the observed tuning effects. Another possibility is that the O^{2-} ions may simply diffuse into Cu via the grain boundaries without being driven by a field. However, there is no reason that such diffusion process can be modulated by the gate voltage.

Alternatively, we hypothesize a Li diffusion process via the Cu grain boundaries. The ionic gating voltage can modulate the concentration of Li on the Cu surfaces, thereby controlling the diffusion. Our gating experiment with PEO:$LiClO_4$ electrolyte and Cu films resembles some electrochemical systems used to study Li ion batteries [51]. In these systems, Li^+ containing electrolyte is in contact with a Cu electrode, and a bias voltage with the proper polarity induces concentrated Li^+ ions or even plated Li metal on the Cu surface. Diffusion of Li from the surface into the bulk of the Cu electrode occurs along the grain boundaries [51-54]. When the bias voltage changes sign, the process is reversed, and Li moves out of the Cu [51]. Another relevant and similar process is that Li^+ ions can intercalate into layered electrodes of Li ion batteries or layered 2-D materials and can be removed by reversing the bias [55-57].

We propose the following scenarios for our system. Under a positive V_g, high concentration of Li is induced on the Cu channel surfaces because of the accumulated Li^+ ions from the electrolyte and/or plated Li metal, and Li diffuses into the channel along the grain boundaries. Note that Cu is inert to Li and does not form intermetallic compounds with Li at room temperature [58]. It is well known that grain boundaries act as potential barriers for conduction electrons and contribute significantly to momentum relaxation as well as spin relaxation. As Li atoms fill up the grain boundaries in Cu, these potential barriers are effectively reduced leading to a reduced ρ_{cu} and an enhanced λ_{cu}. Under a negative V_g, Li^+ ions or plated Li metal are stripped away from the Cu channel and the surface Li concentration is significantly reduced. Consequently, Li diffuses out of the Cu channel reversing the changes of λ_{cu} and ρ_{cu}.

The lack of tuning in Al channels, as shown in Figure 5.3 (a) and (b), might be attributed to the uniform Al_2O_3 oxide layer, which blocks the diffusion of Li.

Two main features in Figure 5.5 and 5.6, the gradual increase of the tuning range of ΔR_s and the evolution of its hysteresis, can now be explained in the context of Li diffusion. With repeated bidirectional Li diffusion under gate cycling, the diffusion paths along the grain boundaries become more efficient and the diffusivity for Li increases. At positive V_g, more Li diffuses into the Cu channel. At negative V_g, a greater fraction of the trapped Li in Cu moves out of the channel. Therefore, the tuning range of ΔR_s increases over time. Previous work has shown that Li can reversibly diffuse into and out of Cu with a small amount being trapped.[38] Also because of the enhanced diffusivity, the Li density inside the Cu channel depends more sensitively on the Li concentration at the Cu surfaces. Therefore, the measured ΔR_s responds readily to the applied V_g, which regulates the surface Li concentration, and there is less hysteresis in the ΔR_s versus V_g curve in Figure 5.6 (c). The exact cause of the enhanced diffusivity is a subject of future study. Possible reasons include cleansing of the grain boundaries via repeated diffusion.

Now we may explain the tuning of the Kondo effect in the context of Li diffusion. Under a positive V_g, concentrated Li atoms accumulate in the Cu grain boundaries. The chemical environment of the Fe impurities, especially those located near the grain boundaries, is profoundly altered from that in a pure Cu host. Therefore, the effectiveness of the antiferromagnetic exchange interaction between the Fe impurity spin and the conduction electron spins is reduced and the Kondo effect is quenched. Under negative V_g, Li moves out of the Cu and Kondo effect is recovered. Note that Li and Fe do not form intermetallic compound [53].

5.7 Conclusions

In conclusion, we demonstrate tuning of spin diffusion length λ_{cu}, resistivity ρ_{cu}, and the Kondo effect in Cu thin films by using the ionic gating technique. Polymer electrolyte PEO:$LiClO_4$ is used as the gating medium between a metal gate and the Cu channel of a nonlocal spin valve (NLSV). While ionic gating can be implemented directly at room temperature, warming and cooling are involved to reset the gate voltage for low temperature gating. At 5 K, the spin signal of a NLSV is modulated by an impressive factor of 3. The value of λ_{cu} is tuned between 670 nm and 410 nm and ρ_{cu} is tuned by 9%. In addition, the strength of the Kondo effect is tuned by one order of magnitude.

At room temperature, λ_{cu} is tuned reversibly between 380 nm and 300 nm and ρ_{cu} is tuned by 7%. The tuning ranges of λ_{cu} and ρ_{cu} have been amplified over time by prolonged gating. We conclude that the origin of the tuning effects is electrochemical and is most likely related to reversible diffusion of Li atoms/ions along Cu grain boundaries. The demonstrated tuning range of λ_{cu} allows for effective modulation of the spin current in submicron Cu spin transport channels and opens up the broader potential for tunable metallic spintronic devices.

REFERENCES

[1] O. O. Soykal and M. E. Flatte, Physical Review Letters **104**, 077202 (2010).

[2] C. M. Hu, arXiv:1508.01966 (2015).

[3] J. Grollier, D. Querlioz, K. Y. Camsari, K. Everschor-Sitte, S. Fukami, and M. D. Stiles, Nature Electronics **3**, 360 (2020).

[4] S. Datta and B. Das, Appl Phys Lett **56**, 665 (1990).

[5] H. C. Koo, J. H. Kwon, J. Eom, J. Chang, S. H. Han, and M. Johnson, Science **325**, 1515 (2009).

[6] J. Bass and W. P. Pratt, J. Phys.-Condes. Matter **19**, 183201 (2007).

[7] B. Huang, D. J. Monsma, and I. Appelbaum, Physical Review Letters **99**, 177209 (2007).

[8] T. S. Ghiasi, J. Ingla-Aynes, A. A. Kaverzin, and B. J. van Wees, Nano Lett **17**, 7528 (2017).

[9] L. A. Benitez, J. F. Sierra, W. S. Torres, A. Arrighi, F. Bonell, M. V. Costache, and S. O. Valenzuela, Nat Phys **14**, 303 (2018).

[10] J. S. Xu, T. C. Zhu, Y. K. Luo, Y. M. Lu, and R. K. Kawakami, Physical Review Letters **121**, 127703 (2018).

[11] A. Avsar, J. Y. Tan, M. Kurpas, M. Gmitra, K. Watanabe, T. Taniguchi, J. Fabian, and B. Ozyilmaz, Nat Phys **13**, 888 (2017).

[12] M. Johnson and R. H. Silsbee, Physical Review Letters **55**, 1790 (1985).

[13] F. J. Jedema, A. T. Filip, and B. J. van Wees, Nature **410**, 345 (2001).

[14] Y. Fukuma, L. Wang, H. Idzuchi, S. Takahashi, S. Maekawa, and Y. Otani, Nature Materials **10**, 527 (2011).

[15] X. Y. Shen and Y. Ji, Phys Rev B **104**, 085101 (2021).

[16] H. Shimotani, H. Asanuma, A. Tsukazaki, A. Ohtomo, M. Kawasaki, and Y. Iwasa, Appl Phys Lett **91**, 082106 (2007).

[17] K. Ueno, S. Nakamura, H. Shimotani, A. Ohtomo, N. Kimura, T. Nojima, H. Aoki, Y. Iwasa, and M. Kawasaki, Nature Materials **7**, 855 (2008).

[18] A. S. Dhoot, C. Israel, X. Moya, N. D. Mathur, and R. H. Friend, Physical Review Letters **102**, 136402 (2009).

[19] D. Braga, I. G. Lezama, H. Berger, and A. F. Morpurgo, Nano Lett **12**, 5218 (2012).

[20] A. Das *et al.*, Nat. Nanotechnol. **3**, 210 (2008).

[21] J. Jeong, N. Aetukuri, T. Graf, T. D. Schladt, M. G. Samant, and S. S. P. Parkin, Science **339**, 1402 (2013).

[22] J. T. Ye, Y. J. Zhang, R. Akashi, M. S. Bahramy, R. Arita, and Y. Iwasa, Science **338**, 1193 (2012).

[23] D. Daghero, F. Paolucci, A. Sola, M. Tortello, G. A. Ummarino, M. Agosto, R. S. Gonnelli, J. R. Nair, and C. Gerbaldi, Physical Review Letters **108**, 066807 (2012).

[24] T. Kimura, T. Sato, and Y. Otani, Physical Review Letters **100**, 066602 (2008).

[25] Y. J. Cai, Y. M. Luo, C. Zhou, C. Qin, S. H. Chen, Y. Z. Wu, and Y. Ji, Journal of Physics D: Applied Physics **49**, 185003 (2016).

[26] D. K. Efetov and P. Kim, Physical Review Letters **105**, 256805 (2010).

[27] X. J. Wang, H. Zou, L. E. Ocola, and Y. Ji, Appl Phys Lett **95**, 022519 (2009).

[28] M. Johnson, Physical Review Letters **70**, 2142 (1993).

[29] L. O'Brien, M. J. Erickson, D. Spivak, H. Ambaye, R. J. Goyette, V. Lauter, P. A. Crowell, and C. Leighton, Nat Commun **5**, 3927 (2014).

[30] J. D. Watts, L. O'Brien, J. S. Jeong, K. A. Mkhoyan, P. A. Crowell, and C. Leighton, Physical Review Materials **3**, 124409 (2019).

[31] C. H. Shang, J. Nowak, R. Jansen, and J. S. Moodera, Phys Rev B **58**, R2917 (1998).

[32] D. T. Pierce, R. J. Celotta, J. Unguris, and H. C. Siegmann, Physical Review B **26**, 2566 (1982).

[33] D. Mauri, D. Scholl, H. C. Siegmann, and E. Kay, Physical Review Letters **61**, 758 (1988).

[34] Y. J. Cai, C. Qin, F. Kandaz, X. Y. Shen, C. Zhou, M. W. Jia, Y. M. Luo, Y. Z. Wu, and Y. Ji, Phys Rev B **100**, 144419 (2019).

[35] R. J. Elliott, Physical Review **96**, 266 (1954).

[36] Y. Yafet, Physics Letters A **98**, 287 (1983).

[37] L. O'Brien, D. Spivak, J. S. Jeong, K. A. Mkhoyan, P. A. Crowell, and C. Leighton, Physical Review B **93**, 014413 (2016).

[38] P. A. Schroeder, R. Wolf, and J. A. Woollam, Physical Review **138**, A105 (1965).

[39] D. Goldhaber-Gordon, J. Gores, M. A. Kastner, H. Shtrikman, D. Mahalu, and U. Meirav, Physical Review Letters **81**, 5225 (1998).

[40] K. W. Kim, L. O'Brien, P. A. Crowell, C. Leighton, and M. D. Stiles, Physical Review B **95**, 104404 (2017).

[41] J. P. Franck, D. L. Martin, and F. D. Manchester, Proceedings of the Royal Society of London Series A-Mathematical and Physical Sciences **263**, 494 (1961).

[42] J. T. Batley, M. C. Rosamond, M. Ali, E. H. Linfield, G. Burnell, and B. J. Hickey, Physical Review B **92**, 220420(R) (2015).

[43] E. C. Hirschkoff, M. R. Shanabarger, O. G. Symko, and J. C. Wheatley, Journal of Low Temperature Physics **5**, 545 (1971).

[44] T. A. Petach, M. Lee, R. C. Davis, A. Mehta, and D. Goldhaber-Gordon, Phys Rev B **90**, 081108 (2014).

[45] J. Walter, H. L. Wang, B. Luo, C. D. Frisbie, and C. Leighton, ACS Nano **10**, 7799 (2016).

[46] B. Cui, P. Werner, T. P. Ma, X. Y. Zhong, Z. C. Wang, J. M. Taylor, Y. C. Zhuang, and S. S. P. Parkin, Nature Communications **9**, 3055 (2018).

[47] S. Dushenko, M. Hokazono, K. Nakamura, Y. Ando, T. Shinjo, and M. Shiraishi, Nature Communications **9**, 3118 (2018).

[48] L. Liang, Q. H. Chen, J. M. Lu, W. Talsma, J. Shan, G. R. Blake, T. T. M. Palstra, and J. T. Ye, Science Advances **4**, eaar2030 (2018).

[49] L. Baldrati, A. J. Tan, M. Mann, R. Bertacco, and G. S. D. Beach, Applied Physics Letters **110**, 012404, 012404 (2017).

[50] M. Huang, A. J. Tan, M. Mann, U. Bauer, R. Ouedraogo, and G. S. D. Beach, Scientific Reports **7**, 7452, 7452 (2017).

[51] S. S. Lv, T. Verhallen, A. Vasileiadis, F. Ooms, Y. L. Xu, Z. L. Li, Z. C. Li, and M. Wagemaker, Nature Communications **9**, 2152 (2018).

[52] B. J. Neudecker, N. J. Dudney, and J. B. Bates, Journal of the Electrochemical Society **147**, 517 (2000).

[53] R. Rupp, B. Caerts, A. Vantomme, J. Fransaer, and A. Vlad, Journal of Physical Chemistry Letters **10**, 5206 (2019).

[54] D. Rehnlund, J. Pettersson, K. Edstrom, and L. Nyholm, Chemistryselect **3**, 2311 (2018).

[55] M. S. Whittingham, Chemical Reviews **104**, 4271 (2004).

[56] Y. J. Yu *et al.*, Nat. Nanotechnol. **10**, 270 (2015).

[57] M. Rajapakse, B. Karki, U. O. Abu, S. Pishgar, M. R. K. Musa, S. M. S. Riyadh, M. Yu, G. Sumanasekera, and J. B. Jasinski, Npj 2d Materials and Applications **5**, 30 (2021).

[58] H. Okamoto, Journal of Phase Equilibria and Diffusion **32**, 172 (2011).

CONCLUSION

Despite extensive studies of spin transport in light metals, it remains a challenge to achieve spin diffusion length well above 1 μm even under low temperatures. In chapter 3, we demonstrated an average spin diffusion length of 3.2 ± 0.7 μm, and an average spin relaxation time of 120 ± 50 ps at 30 K using 14 Cu-based NLSVs with channel cross sections of 0.5 × 0.5 μm^2. These channels also exhibited superior electrical conductivities and residual resistivity ratios. In spite of the nominally identical fabrication conditions as these NLSVs were fabricated in the same batch, substantial variations of λ_{Cu}, RRR and resistivity were found among the 14 channels and these three parameters correlated well to one another. The most conductive channel yielded λ_{Cu} = 5.3 ± 0.8 μm and τ_s = 270 ± 80 ps at 30 K. These exceptional values exceed the expectations for metals and can be explained by the reduced scatterings from grain boundaries and surfaces owing to the larger channel cross sections using the Mayadas–Shatzkes model and the Fuchs–Sondheimer model. This study highlights the importance of reducing the grain boundary and surface spin relaxations to improve the spin transport efficiency.

The Kondo effect, a many-body phenomenon, has been studied for decades and is relatively well understood. However, it still poses many critical questions such as the existence of the elusive Kondo screening cloud and the interaction of overlapping clouds. In chapter 4, we studied the Kondo effect induced spin relaxation and observed an unexpected scaling between the Kondo spin relaxation rate ${\tau_{sK}}^{-1}$ and the Kondo momentum relaxation rate ${\tau_{eK}}^{-1}$. We fabricated 20 NLSVs with submicron

Cu channels that contain dilute Fe impurities, with the impurity concentration C_{Fe} ranging from 1 to 12 ppm. For each device, we measured its spin signal and resistivity from 5 to 100 K. We determined the Kondo spin relaxation rate and the Kondo momentum relaxation rate of each individual device as functions of temperature. For any given NLSV, ${\tau_{sK}}^{-1}$ is linearly proportional to ${\tau_{eK}}^{-1}$ under varying temperature. However, as C_{Fe} varies among the 20 devices, ${\tau_{sK0}}^{-1}$ remains approximately constant despite ${\tau_{eK0}}^{-1}$ varies with the impurity concentration by one order of magnitude. The ratio of the Kondo spin relaxation rate to the Kondo momentum relaxation rate gives the Kondo spin relaxation probability α_K, which has been assumed to be constant by previous studies. Our data suggest that while this probability is constant under varying temperature for a particular device with a specific impurity concentration, it increases from 0.045 to 0.44 as the impurity concentration decreases from 12 to 1 ppm.

The unexpected relation between ${\tau_{sK}}^{-1}$ and ${\tau_{eK}}^{-1}$ can be qualitatively explained by the overlapping of adjacent Kondo clouds. The clouds, theoretically calculated to be ~ 120 nm in our Cu channels, was found to be significantly larger than the separation of nearby impurities, which was estimated to be between 10 to 20 nm depending on the impurity concentration of the specific channel. Thereby, in all of our 20 NLSVs the clouds heavily overlap and form continuous Kondo medium in the Cu channels. When two clouds overlap their spin densities may cancel due to the random orientations of the Kondo clouds. Our data suggest that within the concentration range of 1-12 ppm, the Kondo medium spin density remains approximately constant, leading to a constant Kondo spin relaxation rate across all 20 devices. This study provides evidence for the existence of Kondo clouds in the diffusive regime and opens up a new avenue for investigating the Kondo screening cloud in light metals, which involves utilizing the spin transport measurement along with the conventional charge transport measurement.

The electrical tunability of spintronic devices is a highly desired feature as it can enable novel spintronic functionalities. In chapter 5, we demonstrated tunable spin diffusion length, resistivity, and Kondo effect in Cu channels of NLSVs by using the ionic gating technique. Solid polymer electrolyte containing Li^+ ions was applied to the sample immersing both the NLSV and a lateral gate patterned a few micrometers away from the channel. The Li^+ ion concentration at the surface of the channel was modulated by adjusting the gate voltage. A positive gate increases the Li^+ concentration and a negative gate decreases the concentration.

In contrast to the values under 0 gate, positive gate enhanced the spin signal, spin diffusion length, and Cu conductivity whereas negative gate reduced these parameters. Furthermore, prominent Kondo spin and momentum relaxations were observed only under negative gate. At 5 K, a remarkable threefold reversible modulation of the spin signal was observed. The tuning of λ_{cu} ranged from 670 to 410 nm, and the Cu resistivity showed 9% tunability. Additionally, the strength of the Kondo effect due to the Fe impurities was tuned by one order of magnitude. At room temperature, λ_{cu} was tuned between 380 and 300 nm, and the tunability of ρ_{cu} was 7%. Over repeated gate cycling, the tuning ranges of both the spin signal and the resistivity gradually expanded, while the hysteresis of the spin signal gradually diminished.

The discussion of electrostatic versus electrochemical origin has always been a focal point in experiments employing the ionic gating technique. The observed evolution of the gating effects and the tunable Kondo effect strongly suggest electrochemical origin. We hypothesized that the reversible diffusion of Li along the Cu grain boundaries is responsible for the tuning effects. The controllable spin relaxation enables the manipulation of the spin current in the metallic channel, opening up possibilities for novel spintronic devices.

Appendix

REPRINT PERMISSIONS

Reprint permission for Figure 2.4:

SPRINGER NATURE LICENSE
TERMS AND CONDITIONS

Jan 02, 2024

This Agreement between Xingyu Shen ("You") and Springer Nature ("Springer Nature") consists of your license details and the terms and conditions provided by Springer Nature and Copyright Clearance Center.

License Number	5700620263475
License date	Jan 02, 2024
Licensed Content Publisher	Springer Nature
Licensed Content Publication	Springer eBook
Licensed Content Title	Phenomenological Theory of Giant Magnetoresistance
Licensed Content Author	J. Mathon
Licensed Content Date	Jan 1, 2001
Type of Use	Thesis/Dissertation
Requestor type	academic/university or research institute
Format	print and electronic
Portion	figures/tables/illustrations
Number of figures/tables/illustrations	1
Will you be translating?	no
Circulation/distribution	50000 or greater
Author of this Springer Nature content	no
Title of new work	ENHANCEMENT, QUANTITATIVE UNDERSTANDING, AND TUNING OF SPIN DIFFUSION LENGTH IN COPPER
Institution name	University of Delaware
Expected presentation date	Jan 2024
Portions	4.7
Requestor Location	Xingyu Shen 104 The Green Newark, DE 19716 United States Attn: Xingyu Shen
Total	**0.00 USD**
Terms and Conditions	

Reprint permission for Chapter 3:

AIP PUBLISHING LICENSE TERMS AND CONDITIONS

Jan 02, 2024

This Agreement between Xingyu Shen ("You") and AIP Publishing ("AIP Publishing") consists of your license details and the terms and conditions provided by AIP Publishing and Copyright Clearance Center.

License Number	5700930941994
License date	Jan 02, 2024
Licensed Content Publisher	AIP Publishing
Licensed Content Publication	Journal of Applied Physics
Licensed Content Title	Low temperature spin relaxation length exceeding 3 μm in highly conductive copper channels
Licensed Content Author	Shen, Xingyu; Ji, Yi
Licensed Content Date	Oct 9, 2023
Licensed Content Volume	134
Licensed Content Issue	14
Type of Use	Thesis/Dissertation
Requestor type	Author (original article)
Format	Print and electronic
Portion	Excerpt (> 800 words)
Will you be translating?	No
Title of new work	ENHANCEMENT, QUANTITATIVE UNDERSTANDING, AND TUNING OF SPIN DIFFUSION LENGTH IN COPPER
Institution name	University of Delaware
Expected presentation date	Jan 2024
Portions	Whole article
Requestor Location	Xingyu Shen 104 The Green Newark, DE 19716 United States Attn: Xingyu Shen
Total	**0.00 USD**
Terms and Conditions	

Reprint permission for Chapter 4:

American Physical Society Reuse and Permissions License

02-Jan-2024

This license agreement between the American Physical Society ("APS") and Xingyu Shen ("You") consists of your license details and the terms and conditions provided by the American Physical Society and SciPris.

Licensed Content Information

License Number:	**RNP/24/JAN/073549**
License date:	02-Jan-2024
DOI:	10.1103/PhysRevB.104.085101
Title:	Scaling of Kondo spin relaxation: Experiments on Cu-based nonlocal spin valves with Fe impurities
Author:	Xingyu Shen and Yi Ji
Publication:	Physical Review B
Publisher:	American Physical Society
Cost:	USD $ 0.00

Request Details

Does your reuse require significant modifications: No

Specify intended distribution locations:	United States
Reuse Category:	Reuse in a thesis/dissertation
Requestor Type:	Author of requested content
Items for Reuse:	Whole Article
Format for Reuse:	Electronic and Print
Total number of print copies:	Up to 1000

Information about New Publication:

University/Publisher:	University of Delaware
Title of dissertation/thesis:	ENHANCEMENT, QUANTITATIVE UNDERSTANDING, AND TUNING OF SPIN DIFFUSION LENGTH IN COPPER
Author(s):	Xingyu Shen
Expected completion date:	Jan. 2024

License Requestor Information

Name:	Xingyu Shen
Affiliation:	Individual
Email Id:	xingyu@udel.edu
Country:	United States

Reprint permission for Chapter 5:

American Physical Society Reuse and Permissions License

02-Jan-2024

This license agreement between the American Physical Society ("APS") and Xingyu Shen ("You") consists of your license details and the terms and conditions provided by the American Physical Society and SciPris.

Licensed Content Information

License Number:	**RNP/24/JAN/073550**
License date:	02-Jan-2024
DOI:	10.1103/PhysRevB.106.085118
Title:	Tuning of spin relaxation and the Kondo effect in copper thin films by ionic gating
Author:	Xingyu Shen et al.
Publication:	Physical Review B
Publisher:	American Physical Society
Cost:	USD $ 0.00

Request Details

Does your reuse require significant modifications: No

Specify intended distribution locations:	United States
Reuse Category:	Reuse in a thesis/dissertation
Requestor Type:	Author of requested content
Items for Reuse:	Whole Article
Format for Reuse:	Print and Electronic
Total number of print copies:	Up to 1000

Information about New Publication:

University/Publisher:	University of Delaware
Title of dissertation/thesis:	ENHANCEMENT, QUANTITATIVE UNDERSTANDING, AND TUNING OF SPIN DIFFUSION LENGTH IN COPPER
Author(s):	Xingyu Shen
Expected completion date:	Jan. 2024

License Requestor Information

Name:	Xingyu Shen
Affiliation:	Individual
Email Id:	xingyu@udel.edu
Country:	United States